Investigation of Ultra-High Performance Concrete for Longitudinal Joints in Deck Bulb Tee Bridge Girders

Timothy John Peruchini

A thesis

submitted in partial fulfillment of the

requirements for the degree of

Master of Science in Civil Engineering

University of Washington

2017

Committee:

John Stanton

Paolo Calvi

Program Authorized to Offer Degree:

Civil and Environmental Engineering

©Copyright 2017

Timothy John Peruchini

University of Washington

Abstract

Investigation of Ultra-High Performance Concrete for Longitudinal Joints in Deck Bulb Tee Bridge Girders

Timothy John Peruchini

Chair of the Supervisory Committee:
Professor John Stanton
Civil and Environmental Engineering

In recent decades, many state DOTs have implemented ultra-high performance concrete (UHPC) in bridge construction because of its advanced mechanical properties beyond those of conventional concrete. The Federal Highway Administration (FHWA) has extensively tested a proprietary class of UHPC, but WSDOT has been hesitant to adopt this mix because of its high cost and associated high risk. In this study, a mix design developed by Washington State University was tested for its structural performance when used in a reinforced spliced connection between adjacent concrete deck-bulb tee (DBT) bridge decks. The important parameter for this application is the bond strength of epoxy-coated reinforcing bars to the UHPC as well as the tension strength of the UHPC when the rebar in the connection is stressed axially in tension. ASTM-standard test procedures in this study showed that compressive strengths up to 16 ksi, tension strengths above 2 ksi, and bond strengths up to 7 ksi can be achieved with this particular UHPC, all with improved ductility beyond that of conventional concrete due largely to the steel fiber reinforcement. Structural experiments were performed on idealized “bond curbs” as well as a section of deck representing actual DBT girders to determine the available bond strength and

the corresponding required joint width. These experiments and the subsequent analysis showed that a UHPC joint width of 7.11 inches, corresponding to a splice length of 5.11 inches, is satisfactory to fracture the reinforcement within the connection. To account for construction tolerances, this joint width should, in practice, be increased to 10 inches.

TABLE OF CONTENTS

LIST OF FIGURES

LIST OF TABLES

LIST OF TERMINOLOGY

Variable		Description
a	=	Linear data fit parameter.
A_b	=	Reinforcing bar cross-sectional area.
b	=	Linear data fit parameter.
B	=	Specimen width.
c_b	=	Clear cover.
D	=	Diameter.
d_{avg}	=	Distance from the compression face of a beam to the average centroid of reinforcing bars.
d_b	=	Reinforcing bar diameter.
E_c	=	Concrete modulus of elasticity.
$f_c', f_{c,28}'$	=	Concrete 28-day specified compressive strength.
$f_{c,14}'$	=	Concrete 14-day specified compressive strength.
f_{DT}	=	Direct tension average stress.
f_{min}	=	Minimum live-load stress resulting from the AASHTO Fatigue I load combination, combined with the more severe stress from either the permanent loads or the permanent loads, shrinkage, and creep-induced external loads.
f_r	=	UHPC modulus of rupture.
f_s	=	Axial tension stress in a single reinforcing bar.
$f_{s,t}$	=	Reinforcing bar stress in the extreme layer of tension reinforcement for a beam.
f_{sa}	=	Allowable reinforcing bar axial tension stress.
f_t	=	UHPC split-tension strength.
L	=	Specimen length.
L_e	=	Reinforcing bar embedment length into UHPC.
L_{spl}	=	Reinforcing bar splice length with adjacent reinforcement within UHPC.
M_n	=	Nominal bending moment capacity of a concrete cross-section.
r^2	=	Coefficient of determination.
S_1	=	Compression cylinder stress corresponding to a longitudinal strain of 50 millionths.
S_2	=	Compression cylinder stress corresponding to 40% of the ultimate load of the UHPC.

t	=	Curing time.
t_{50}	=	Curing time required for UHPC to reach 50% of its 14-day strength.
T_{tot}	=	Axial tension stress in all reinforcing bars within one layer of a beam.
$(\Delta F)_{TH}$	=	Constant-amplitude fatigue threshold for reinforcing bar stress.
α	=	Ratio between the allowable bond stress and ultimate bond stress.
β	=	Bond stress distribution factor along the length of a reinforcing bar.
ε_2	=	Compression cylinder strain produced by S_2.
σ_s	=	Axial tension stress in a single steel fiber.
τ_b	=	Bond stress around the perimeter of a single steel fiber.
ζ	=	Ratio between bond curb reinforcing bar stress and simulated deck reinforcing bar stress.
ζ_{avg}	=	Average ratio between bond curb reinforcing bar stress and simulated deck reinforcing bar stress for all specimens.

EXECUTIVE SUMMARY

Bridges that are constructed in remote, rural areas throughout Washington State present access difficulties for traditional construction equipment like concrete delivery trucks. In response to this constraint, the Washington State Department of Transportation (WSDOT) worked with local precast concrete manufacturers to create deck bulb tees (DBTs). In these girders, a section of driving deck is precast monolithically with the girders so that, when they are lifted into place, only the adjacent deck elements need to be connected. This can be done using welded steel inserts and a grouted joint, thereby eliminating the need for fresh concrete on site. Deck bulb tees have been widely used in remote areas, and on county roads, which attract less traffic than do major highways.

In the current connection between adjacent deck panels, pieces of plate welded to reinforcing bar anchors are embedded in the girder flanges at approximately 6 ft intervals along the span. When the DBTs have been erected and levelled, a round steel bar is placed in the trough created by the flat bars and is flare-bevel welded, providing the immediate connection between the flanges. Each flange tip is also equipped with a continuous grout key detail. After all the welded connections have been completed, the grout key is filled to complete the connection.

Because DBT bridges can be constructed quickly, the WSDOT is interested in using them on major highways, but the traditional flange connections described above have deteriorated under truck loading. As a result, WSDOT seeks a more robust connection and proposes to use one in

which rebars projecting laterally from the flanges are spliced within a pour strip of Ultra-High Performance Concrete (UHPC).

UHPC is a type of fiber-reinforced concrete which can achieve far superior compression, tension, and bond strengths, and ductility than conventional concrete, mostly due to the addition of steel fibers as reinforcement. These features allow for very short splice lengths and narrow pour strips. Lafarge Cement was one of the early developers of UHPC, and their proprietary material, Ductal®, has been widely used. However, it costs on the order of 20-30 times more than conventional concrete because it uses some high-quality, imported materials. The goal of this project was to investigate the structural performance of a spliced joint made using a new UHPC mix that uses locally-sourced materials to decrease the cost. The mix design was developed by Qiao and Allenas at Washington State University. The structural testing of the joints was conducted at the University of Washington.

To characterize the structural performance of this UHPC, physical experiments were conducted at the University of Washington. They were divided into material tests and structural tests. In the materials tests, emphasis was placed on the tension strength and bond strength of the epoxy-coated #5 reinforcing bars that will be used in DBT flanges. However, other tests to characterize the material properties were also conducted, and included both ASTM-standard and custom experiments. The former showed compression strengths of 15.95 ksi and 13.10 ksi, in 2-inch cubes and 4-inch diameter cylinders respectively. ASTM-standard 4-inch diameter split-tension cylinders, 3-inch by 4-inch flexural beams, and custom 2-inch by 2-inch direct tension experiments revealed tension strengths of 2.16 ksi, 2.65 ksi, and 0.96 ksi, respectively.

Next, bond tests were conducted. Two different types of experiments were performed: one to determine the pullout bond strength ("pullout bond curbs") where the reinforcing bar slips

through the UHPC, and one to determine the tension strength of a non-contact splice ("splice-connection bond curb".) Splices with different lap lengths and side cover values were tested in this series. The bond pullout curb specimens were tested by stressing the reinforcing bar in tension with a center-hole hydraulic ram. The hydraulic ram for the pullout bond curb experiments rested directly on the UHPC and consequently suppressed tension modes of failure, whereas the ram for the splice-connection bond curb experiments did not. The pullout bond curb experiments revealed that an embedment length of 6 inches was sufficient to fracture the reinforcing bar, and in the splice-connection bond curb experiments a splice length of 5 inches (corresponding embedment length of 6 inches) proved to be enough to fracture the rebar.

The final series of experiments determined the bond strength of a real UHPC joint connecting two precast concrete deck panels using a non-contact spliced connection. These experiments were loaded in three-point bending by a simulated truck wheel placed on the joint until the non-contact spliced connection failed. Eight specimens were tested. In four, the joint width (and thus the embedment/splice lengths) varied; in two more, the clear cover over the main tension reinforcement varied, and in the last two the offset between opposing reinforcing bars was varied to simulate the effect of construction tolerances. The results of these experiments and subsequent analyses showed that a joint width of 7.11 inches (corresponding to a splice length of 5 inches) was required to fracture the reinforcing bars.

Analyses were conducted on bridge decks subjected to wheel loads. They showed that the stresses imposed on the UHPC joint by AASHTO truck loading were a small fraction of the joint capacity, and that standard wheel loading should not be expected to even cause cracking at the interface between the UHPC and the conventional concrete panel. Furthermore, wheel loading would be expected to cause punching shear failure at a load much lower than that required to

cause flexural failure of the UHPC joint. It was thus concluded that the strength of the UHPC joint tested here was sufficient for the anticipated wheel loads.

The final recommendation for joint width was approximately 10 inches, based on the bars' failing in fracture rather than bond, and modified to account for fabrication and construction tolerances.

Chapter 1
INTRODUCTION

Bridges that are constructed in remote, rural areas throughout Washington State often present access difficulties for traditional construction equipment like concrete mixing trucks. This leads to the desire to eliminate any major cast-in-place concrete operations and replace them with precast concrete alternatives. Projects which aim to utilize precast construction typically involve using precast girders which are manufactured offsite, transported to the construction site, and lifted into place by a crane. A cast-in-place concrete deck is then poured atop the girders to connect them and create a driving surface. This construction method is faster than a purely cast-in-place approach, but it still requires a concrete truck to be able to access the site to pour the driving deck, as well as time and labor associated with building the formwork and placing deck reinforcement. In response, the Washington State Department of Transportation (WSDOT) created a series of girders which eliminate the need for any significant cast-in-place activities.

In these girders, called decked bulb tees (DBTs), the driving deck is precast monolithically with the girders so that when they are lifted into place (see Figure 1.1) only the adjacent girder flanges need to be connected. This construction method is attractive because it simplifies the construction procedure and reduces onsite congestion, labor, and time, all of which help to minimize the project's overall cost. It also makes possible the use of precast, prestressed concrete girders in remote areas.

Figure 1.1. A precast DBT girder being lifted into place by a crane.

Figure 1.2 shows the connection that is currently being used by WSDOT to connect the adjacent decks (Washington State Department of Transportation 2016). It consists of forming a keyway in the face of each deck element and embedding steel headed studs with welded steel flat bars that are spaced incrementally throughout the bridge's span. Once each DBT is lifted into place, a round steel bar is placed in the trough created by the flat bars, and is flare-bevel welded. There is also an alternate detail which consists of flare-bevel welding steel angle shapes to the ends of the embedded headed studs and fillet welding a rectangular steel bar atop the angles. After all components have been welded, the grout key, shown dashed in Figure 1.2, is filled to finalize the connection. Typically, adjacent girders will not have identical cambers, and they need to be jacked up or down during construction to achieve alignment. The welded detail is used to hold the flanges in place after jacking, and the grout key, which takes time to gain strength, carries most of the traffic loads under service conditions. The steel embedments are spaced at approximately 6-feet on-center, while the grout key is essentially continuous.

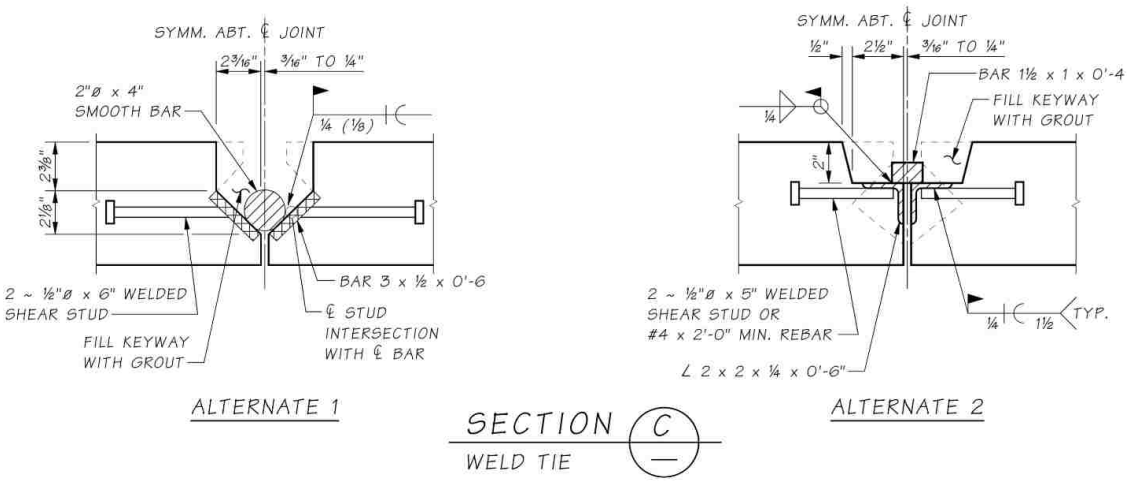

Figure 1.2. Existing WSDOT detail for connecting adjacent DBTs.

In the field, this connection has shown damage under heavy truck loading, largely by spalling of the grout and the concrete surrounding the steel embedments. Consequently, DBT bridges are used primarily on roads with light traffic. WSDOT proposed to eliminate this connection and replace it with one which uses Ultra-High Performance Concrete (UHPC) with the goal of being able to use DBT bridges on highways with heavier traffic.

Figure 1.3 depicts the proposed structural detail which involves projecting the deck reinforcement transversely into the joint where the adjacent DBT's reinforcement will then overlap in a non-contact splice. To replace the grout which the previous connection used, the joint will be filled with UHPC to create a non-contact spliced connection.

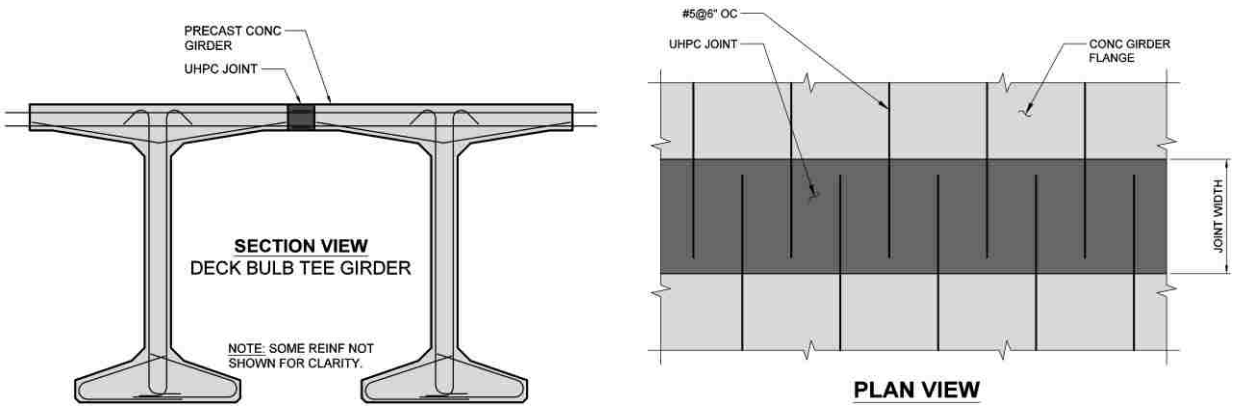

Figure 1.3. Proposed UHPC non-contact splice connection.

UHPC is a type of fiber-reinforced concrete which can achieve far superior compression, tension, and bond strengths and ductility than conventional concrete mostly due to the addition of steel fibers as reinforcement. Several research groups throughout the United States are investigating UHPC, including Iowa State University, Montana State University and the New York State Department of Transportation (NYSDOT), but the most extensive investigations have been conducted under Benjamin Graybeal at the Federal Highway Administration (FHWA). Lafarge has developed their own proprietary UHPC, named Ductal®, and this material both dominates the marketplace and has been the material used in Graybeal's work (Graybeal, Design and Construction of Field-Cast UHPC Connections 2014). It has been extensively tested and has been implemented in multiple bridge projects by the NYSDOT, some of which utilized connections similar to WSDOT's proposal.

The first challenge of using a UHPC connection is its availability and cost. Ductal® is currently the only commercially available mix for any project intending to use UHPC. It can achieve compressive strengths up to 30,000 psi but costs approximately 20-30 times more than conventional concrete largely due to using high-quality, imported materials. For this reason, WSDOT proposed that a new UHPC mix be designed which uses locally-sourced materials to

reduce the cost enough for this connection to be a worthwhile replacement. Apart from administrative considerations such as cost, the other issue is its structural behavior and, more specifically, how well steel reinforcement bonds to UHPC and how the connection performs. UHPC is praised for its high tension and compression strength, the former of which is especially important when designing a non-contact spliced connection because bond strength is a function of tension strength. Although projects have incorporated UHPC in similar connections, they all used Ductal® which means a new set of connection design recommendations must be developed which focus on the structural properties of this specific mix.

Three tasks are required to investigate a new UHPC for this project. First, the UHPC mix design is investigated and optimized for its intended application, then the mechanical properties of the material will be determined, ultimately resulting in a final series of recommendations for the connection design. These responsibilities are split between Dr. Pizhong Qiao and Mr. Zhidong Zhou at Washington State University who designed the mix, and Dr. John Stanton and Mr. Timothy Peruchini at the University of Washington who tested structural connections and developed design criteria.

Chapter 2
PREVIOUS WORK

The initial direction of investigation for this project was largely based on research which has been conducted by Benjamin Graybeal at FHWA over the last decade both on the material characterization of UHPC as well as its structural behavior (Graybeal, Design and Construction of Field-Cast UHPC Connections 2014). Graybeal developed idealized tension stress-strain relationships for the Ductal® brand of UHPC which highlight the effect of steel fibers on post-cracking strength, as illustrated in Figure 2.1.

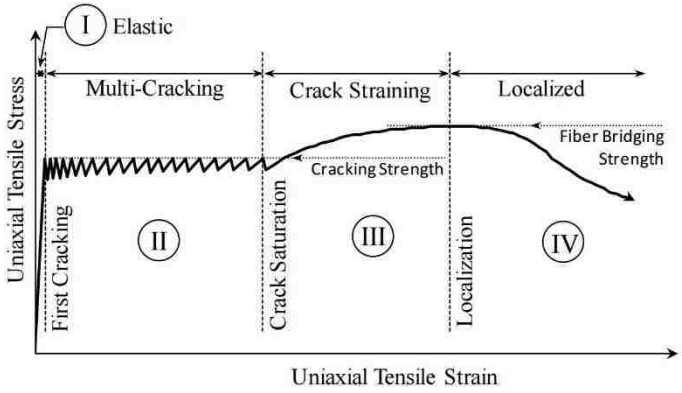

Figure 2.1. Idealized uniaxial tensile mechanical response of UHPC developed by Graybeal.

In this figure, there is a post-cracking stress plateau which accounts for a distribution of fine cracks along the length of the specimen. As the behavior enters the "Crack Straining" region, the cracks widen and the steel fibers slip through the UHPC to provide ductility. The fact that these steel fibers bond strongly to the UHPC allows further strength to be gained while they slip.

Failure occurs after the cracks widen enough to cause the steel fibers to pull out of the cement paste.

Additionally, Graybeal has performed a multitude of material tests to determine various mechanical properties of UHPC, including tension strength, compression strength, creep, shrinkage, fatigue strength, and modulus of elasticity to name a few. Table 2.1 lists typical values for these mechanical properties.

Table 2.1. Summary of Ductal® UHPC mechanical properties.

	Range	
Compressive Strength	20 to 30 ksi	140 to 200 MPa
Tensile Cracking Strength	0.9 to 1.5 ksi	6 to 10 MPa
Modulus of Elasticity	6,000 to 10,000 ksi	40 to 70 GPa
Poisson's Ratio	0.2	0.2
Coefficient of Thermal Expansion	5.5 to 8.5 millionths/°F	10 to 15 millionths/°C
Creep Coefficient	0.2 to 0.8	0.2 to 0.8
Specific Creep	0.04 to 0.30 millionths/psi	6 to 45 millionths/MPa
Total Shrinkage	Up to 900 millionths	Up to 900 millionths

Though the properties provided above are typical, Graybeal notes that the curing method has a notable influence on the strength of UHPC with hot-steam curing creating the strongest and stiffest material (upper range of behaviors in Table 2.1).

In addition to classifying material properties, Graybeal has conducted tests to determine the bond and tensile strength of reinforced UHPC in a non-contact spliced connection similar to the one which this project investigated (Graybeal, Bond Behavior of Reinforcing Steel in Ultra-High Performance Concrete 2014). That testing program utilized uncoated #5 high-strength rebar centered between two uncoated #8 rebar to form an all-tension splice when the #5 rebar is axially stressed. Figure 2.2 shows a sketch for a typical bond curb specimen.

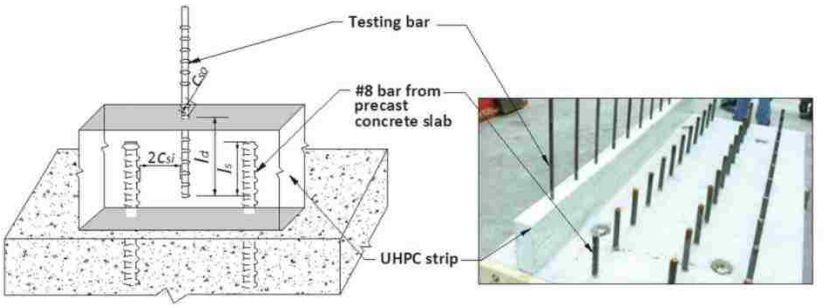

Figure 2.2. Graybeal splice-connection curb schematic.

Graybeal investigated the effects of embedment length, concrete side cover, bar spacing, concrete compressive strength, reinforcing bar type, reinforcing bar size, reinforcing bar yield strength, and casting orientation for his testing program. The measurement of choice for these tests is the #5 bar stress as a function of embedment length, which ranged from approximately 2.25 inches to 6.25 inches. In general, Graybeal observed that there is a linear relationship between bar stress at failure and embedded length, as shown in Figure 2.3, which implies that bond strength is essentially a constant in all tests. Also, increased bar spacing weakened the bond within the connection due to weaker force transfer mechanisms and the connection's strength relies more singularly on the material's properties. Graybeal found that larger rebar sizes decrease the bond and that epoxy-coated rebar have weaker bond than uncoated rebar. Finally, these experiments determined that high-strength rebar which experienced bond failure before yielding have greater bond strength than mild-strength rebar which failed by bond after yielding. This is attributed to the radial contraction which a deformed rebar experiences after it has surpassed its yield strength. Rebar gains its bond strength by the deformations bearing on the concrete, but as the rebar contracts, the deformations disengage from the concrete and the bond strength drops.

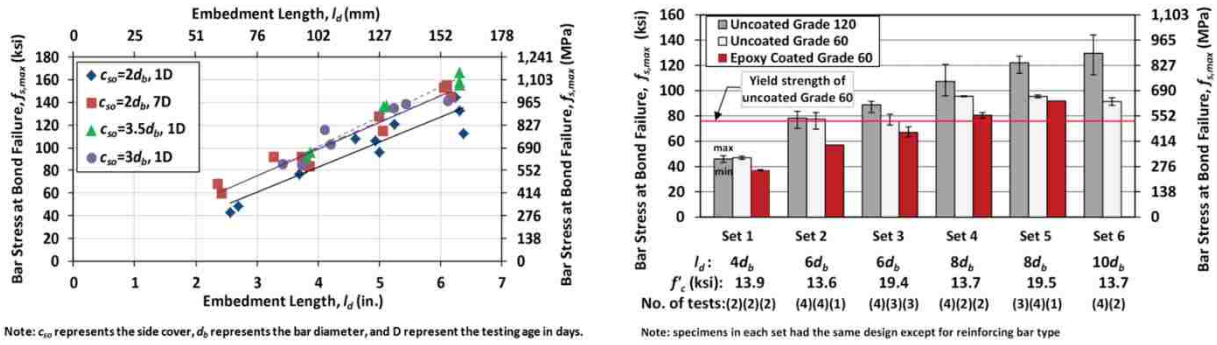

Figure 2.3. Graybeal's results showing bond stress versus embedment length (left) and bond stress versus various types of reinforcing bars (right).

Qiao performed experiments similar to Graybeal's but tested a narrower range of parameters using epoxy-coated #5 rebar (Qiao, Zhou and Allena 2017). Their typical findings are provided in Figure 2.4 which shows the same linear relationship between bar stress and embedment length.

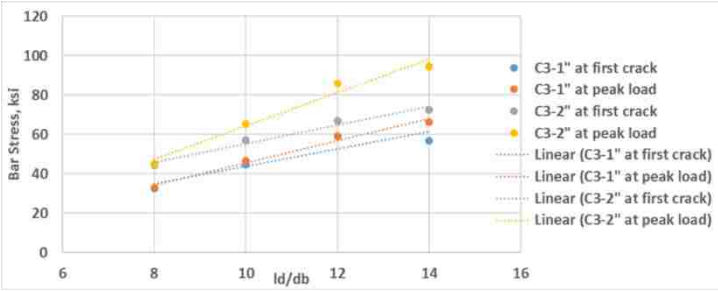

Figure 2.4. Typical plot of bar stress versus embedment length performed by Qiao.

Lee & Lee performed simulated deck tests to determine the behavior of a non-contact spliced connection in a realistic bending application (Lee and Lee 2015). Their specimens consisted of two conventional concrete panels connected by a UHPC joint and loaded in bending. Joint widths ranged from 3.9 to 9.8 inches with lap splice lengths from 2.3 to 6.3 inches. Three different reinforcement splice geometries (see Figure 2.5) were tested: (1) straight bars, (2) 90-degree hook bars, and (3) U-loop bars, each using uncoated #5 rebar. Figure 2.6 depicts one of their typical load-deflection plots for investigating fiber volume where they measured midspan

loads versus displacements as well as moment-curvature curves for precast panels joined by UHPC, all for the straight reinforcement configuration.

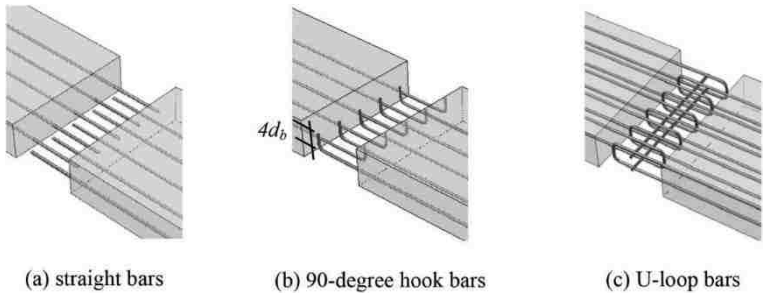

Figure 2.5. Lee & Lee spliced reinforcement geometries.

A second series of experiments was performed on beams entirely made with UHPC which had a lap-spliced connection at midspan. These tests investigated how the steel fiber volume affected performance by varying the fiber volume from 1.0 to 1.6%. The authors found that, as the fiber volume increased, the failure changed from UHPC tension to rebar yield and the ductility capacity increased. However, the effect on strength was small.

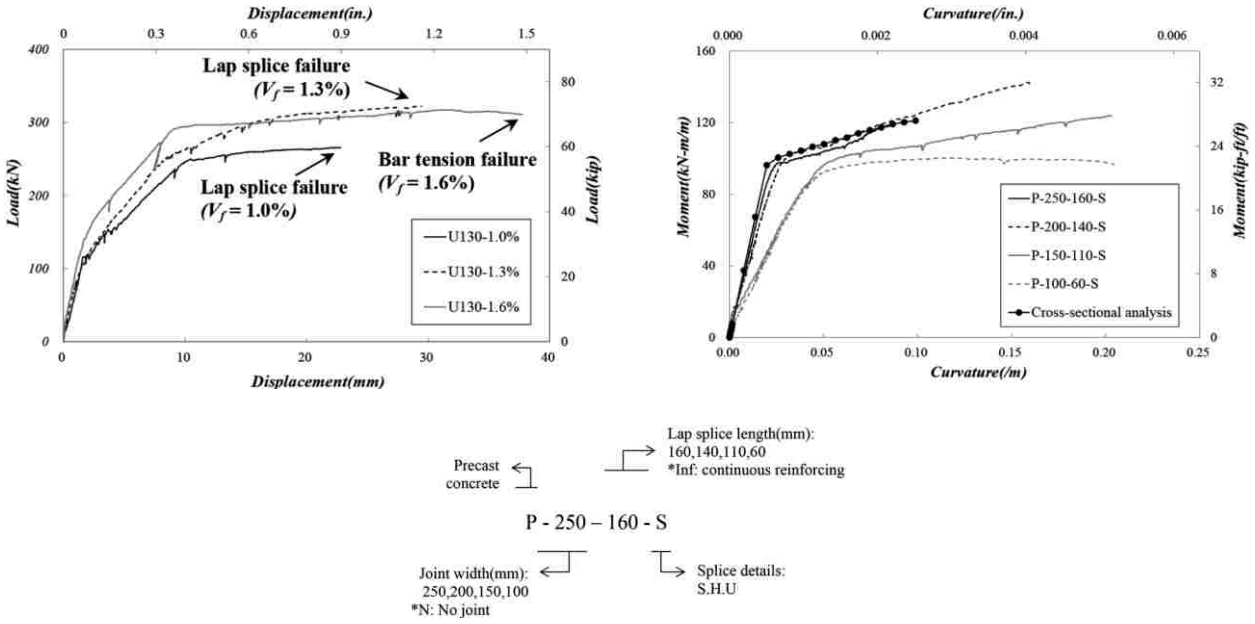

Figure 2.6. Lee & Lee load versus vertical displacement as a function of steel fiber volume for U-shaped reinforcement (top left) and a moment-curvature plot for straight reinforcement (top right) with legend shown (bottom).

In most of their experiments, failure occurred in the precast concrete panel before the UHPC connection. They concluded that a splice length of $7d_b$ or longer was required for the connected panels to behave as a yielding monolithic concrete member.

Chapter 3
STRUCTURAL BEHAVIOR

The primary benefits of UHPC lie in its high compressive strength, high tensile and bond strength, and low permeability. In the present application, the compressive strength and permeability need only match those of the precast concrete in the DBT; if, as is likely, the UHPC properties "exceed" those of the precast concrete, they are no longer critical and further improvements provide no benefit. However, the tension and bond strength are critical because they are the primary factors which influence rebar anchorage and connection performance.

The fibers in the UHPC are the main agent for improving the tension and bond strengths. With respect to those properties, the material's strength is higher and its response is much more ductile than those of conventional concrete. Other researchers have noted that, in addition to the strength, the detailed mechanics of bond may also be different between UHPC and conventional concrete. A few investigators (Karmout, Arafa and Shihada 2009) have studied concrete mixes without fibers that achieve very high compressive stresses, but these are unlikely to provide the tension strength that is necessary for the joints that form the focus of this study, so they are not considered further here.

The behavior of UHPC in general, and particularly the bond in a non-contact spliced connection, are discussed in detail in Appendix A. Here, the following points are emphasized:

The fibers provide both the tension strength and ductility needed for good bond. They are so effective that, in UHPC, the bond strength of epoxy-coated bars is comparable to that of

uncoated bars when sufficient embedment length is provided to ensure the bar yields before bond failure (Yuan and Graybeal 2014).

The length/diameter ratio of the fibers is important, relative to the steel strength. The fibers should fail by ductile pulling out of the paste, and not by brittle fracturing. To achieve this, the length/diameter ratio must satisfy Equation (1).

$$\frac{L}{D} \leq \frac{\sigma_s}{2\tau_b} \quad \textbf{(1)}$$

where σ_s is the tension strength of the fiber and τ_b is its bond strength.

Graybeal found that σ_s of 400 ksi provides good, ductile behavior with $L/D = 65$. The bond strength was unknown but, because the fibers pulled out, Equation (1) suggests that the bond strength was less than 3.3 ksi. For comparison, the bond strength for prestressing strand is about 2.0 ksi at transfer, and 0.7 ksi under ultimate conditions. Strand provides some mechanical interlock with the cement paste while smooth fibers do not, so it can be argued that the bond strength of the fibers was less than 2.0 ksi, in which case the fibers would still have led to ductile behavior if their strength had been less than 400 ksi. The fibers specified by Qiao also have a L/D ratio of 65 and 400 ksi strength.

Consensus is lacking on the subject of fiber orientation. Some claim that the fibers align, at least in part, with the direction of flow during pouring which could influence performance. However, conclusive test evidence has yet to be shown. In any case, control of the fiber orientation is difficult, so it remains a source of uncertainty in the tension and bond strength. Unfortunately, high tension strength is needed perpendicular to the plane of the bridge deck to inhibit splitting in

the plane of the bars, but the flow argument is correct and the fibers are more likely to be oriented in the plane of the deck, which is the least effective orientation.

A deformed rebar that is stressed in tension induces conical struts and hoop stresses in the surrounding concrete. This mechanism exists in both conventional concrete and UHPC. While UHPC has better tension strength to resist those hoop stresses, a mode of failure that depends on such cracking should still be expected in some cases.

Chapter 4
PRELIMINARY COMPUTER MODELING

The overall goal of the research program was to develop details that would provide satisfactory performance in a joint between DBTs subjected to heavy truck loading. This required development of a suitable material, characterization of material, and conducting structural tests to demonstrate that field performance would be satisfactory. The material development was conducted by Qiao (Qiao, Zhou and Allena 2017). To guide the structural tests and to help formulate realistic design guidelines, it was necessary to understand the primary actions that the joint experiences from construction and service (traffic) loading. The most important construction loads are the forces associated with correcting camber differences between adjacent DBT girders. These are analyzed in Appendix G.6.

During service conditions, bending moments due to wheel loads are expected to be the controlling action. To determine the local response of the deck elements to wheel loads, a series of linear-elastic finite element computer analyses (FEA) using Abaqus software was conducted prior to any physical experiments to determine the approximate magnitude and distribution of loads and stresses which the bridge deck must support. The results of these analyses were then used to design the physical experiments and to ensure that their results could be related to the response of a bridge deck in the field.

4.1 Geometry

The purpose of the computer model was to determine the response of wheel loading of a DBT's driving deck using the true geometry. WSDOT's structural drawings for DBT bridges specify a minimum girder centerline spacing of five feet and a maximum of eight feet and both cases are considered in the model. To adequately capture the extent of longitudinal stress distribution, a bridge length of three times the girder spacing was used. This geometry is depicted in Figure 4.1.

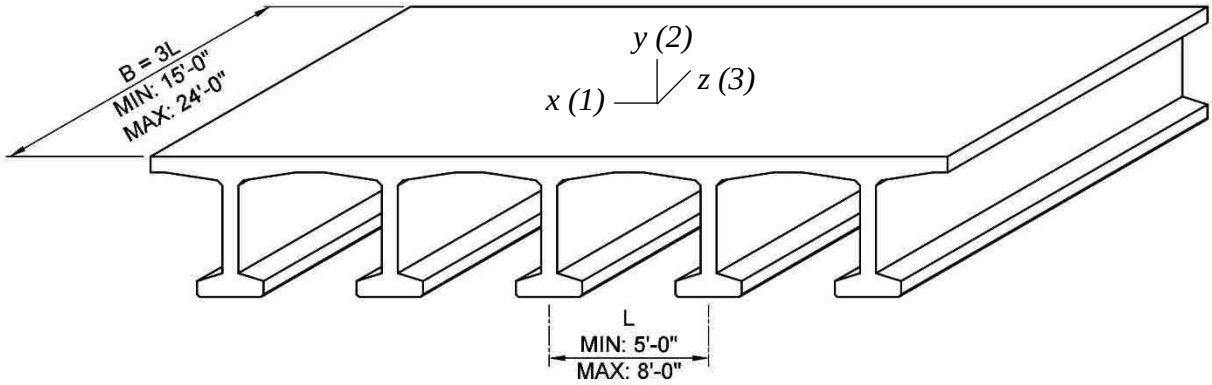

Figure 4.1. Representative bridge geometry considered in the computer analyses.

The girders themselves are shown in Figure 4.1 to illustrate how the various components interact in the bridge, but they are not all explicitly modeled; only the deck profile was modeled and the girder webs were treated as providing rigid vertical supports. The deck of a DBT is haunched and this varying thickness is shown in Figure 4.2

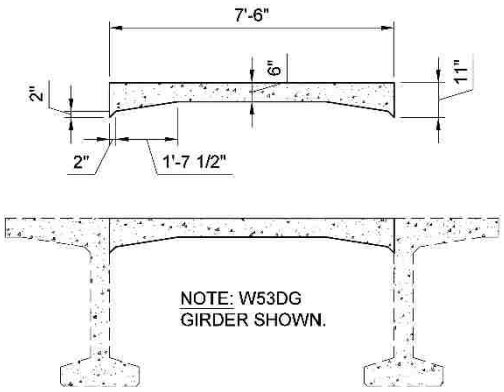

Figure 4.2. Typical deck cross-section dimensions shown for the eight-foot girder spacing.

To capture the effect of the variable deck thickness, 8-node solid elements were used. Boundary conditions are discussed in Section 4.2.

4.2 Boundary Conditions

To keep the size of the model to a manageable level and yet to permit a reasonably fine mesh for viewing the stresses locally, only a part of the deck was modeled. That choice necessitated the selection of boundary conditions at the locations where the model ended but the prototype bridge continued. Each piece of deck was supported at its ends by the girder web with which it is cast monolithically. The webs, which were not included in the model, therefore provided both vertical and rotational constraint to the deck. The vertical constraint was treated as rigid, as discussed below. The rotational restraint is a function of many factors, including geometry and reinforcing layout in the deck, existence of adjacent girder lines, and loading pattern. Furthermore, the torsional stiffness of each girder influences the rotational restraint of the deck. If each girder has low torsional stiffness then the deck will behave like a multi-span element supported on knife-edges, whereas high torsional stiffness will create conditions similar to a single span with fixed ends. It is difficult to determine a representative rotational stiffness for

the deck constraint, so the solution was bracketed by analyzing each loading configuration separately with no ("pinned") and infinite ("fixed") rotational restraint, as shown in Figure 4.3.

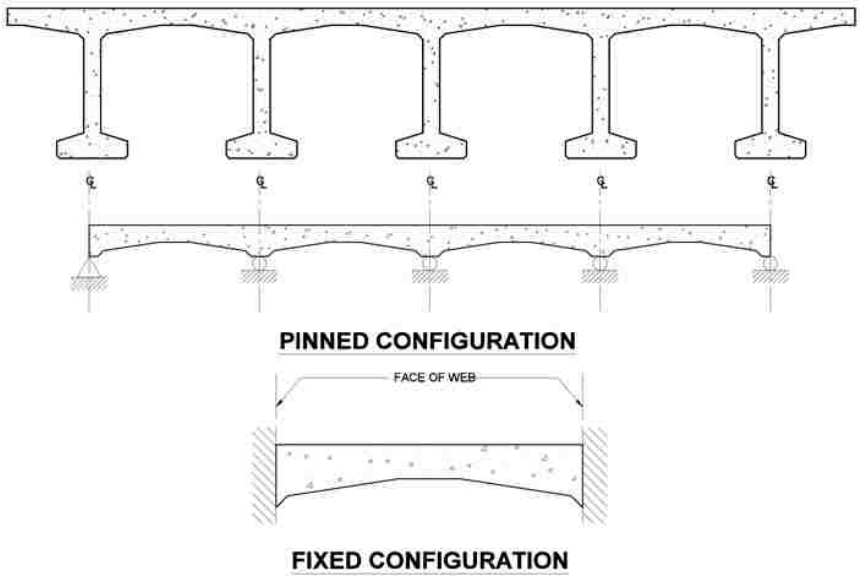

Figure 4.3. Extreme configurations to bound the rotational restraint.

Modeling the girders as rigid vertical supports is nearly, but not exactly, correct. If the truck load is placed as shown in Figure 4.4, the central girder will be more heavily loaded and deflect more than the two adjacent to it. That action will introduce transverse deck bending. However, those bending moments will be approximately symmetric with equal and opposite moments at the end of each deck span, and approximately zero moment at midspan where the UHPC joint is located, as illustrated in Figure 4.4. Thus, the girder vertical flexibility has negligible effect on the joint moments, and accordingly, rigid girders were conservatively assumed for each model.

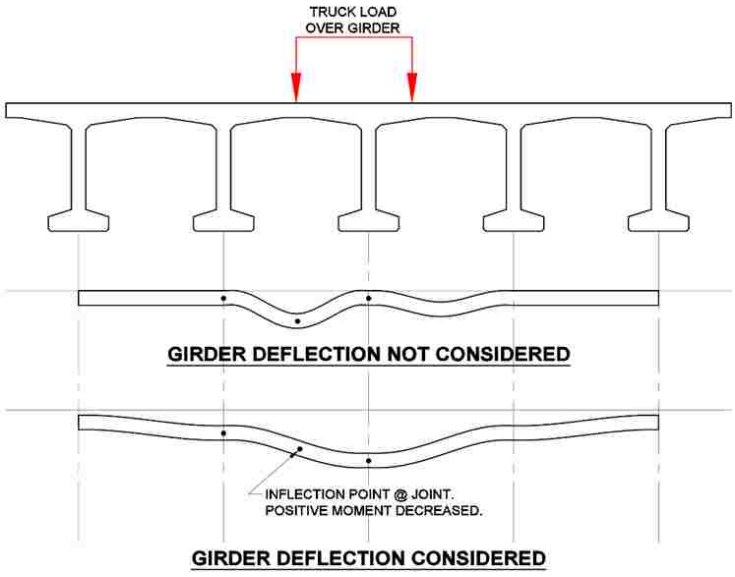

Figure 4.4. Effect of girder bending on the bending moment in the longitudinal deck joint.

4.3 Loads

The most important parameter investigated using the computer models was the stress caused by transverse bending at the location of the UHPC longitudinal joint. Table 4.1 describes the design-level traffic live loads inputted to the model courtesy of the requirements set by the 2012 AASHTO LRFD Bridge Design Specifications. All wheel loads were applied on a 20-inch wide and 10-inch long rectangular patch which represents a truck tire's contact area.

Table 4.1. Code-specified traffic live load cases.

Diagram	Description
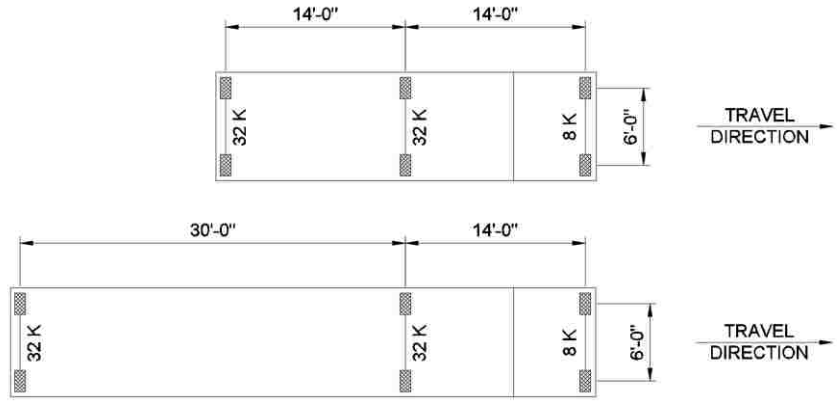	Single Truck Axle (1) 8-kip front axle. (2) 32-kip rear axles. Truck width is 6 feet. Rear axles separated by 14 to 30 feet.

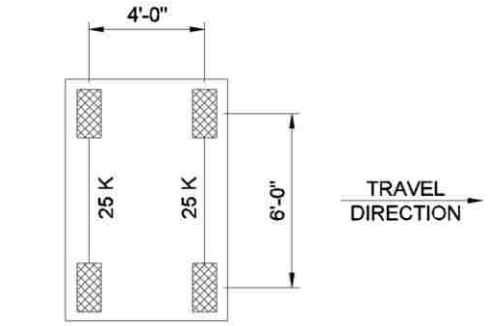	<u>Tandem Truck Axle</u> (2) 25-kip axles. Truck width is 6 feet. Tandem axles separated by 4 feet.
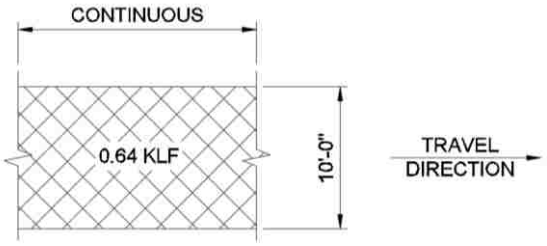	<u>Lane Load</u> 0.64 kip/ft to represent miscellaneous traffic over a 10 foot width along the full length of the bridge.

AASHTO specifies a design live load combination of either the single axle and lane load or tandem axle and lane load, whichever causes the greatest effect.

The results from a preliminary analysis shown in Figure 4.5 of a single wheel load revealed that the highest stresses were located along the transverse line through the load but there was also an approximate 45-degree longitudinal stress distribution. This showed that there was no stress interaction between adjacent loads when separated by a distance greater than the girder spacing. Since the maximum girder spacing is eight feet and the single axle truck loads are separated by a minimum of 14 feet, only one single axle is modeled for simplicity. The tandem axles are spaced are 4 feet on-center, so both were modeled for that load case.

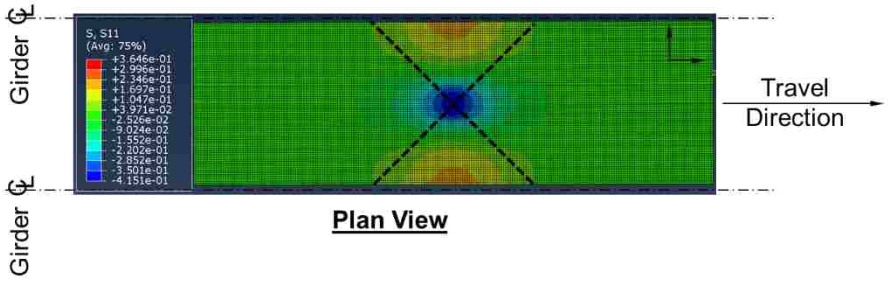

Figure 4.5. Planar stress distribution due to a single wheel load.

4.4 Analysis Cases

To sufficiently bound the results, different geometries and boundary conditions were considered. All three load cases outlined in Table 4.1 were analyzed separately for each model to determine their individual contributions, resulting in a total of 12 analyses. Table 4.2 describes the features of each model.

Table 4.2. Computer model testing matrix.

Model 1	Model 2	Model 3	Model 4
Fixed Supports 5-foot Girder Spacing	Fixed Supports 8-foot Girder Spacing	Pinned Supports 5-foot Girder Spacing	Pinned Supports 8-foot Girder Spacing

The nomenclature used for each model's results is as follows:

Boundary Condition – Geometry – Stress Location – 3D Stress Component

4.5 Analysis Results

Figure 4.6 shows the distribution of transverse bending stress (S_{11}) for both the fixed and pinned configurations for a girder spacing of 8 feet. These responses were typical, and the plots for the other geometries are provided in Appendix F.1. A summary of stresses from each load case is provided in Appendix G.1.

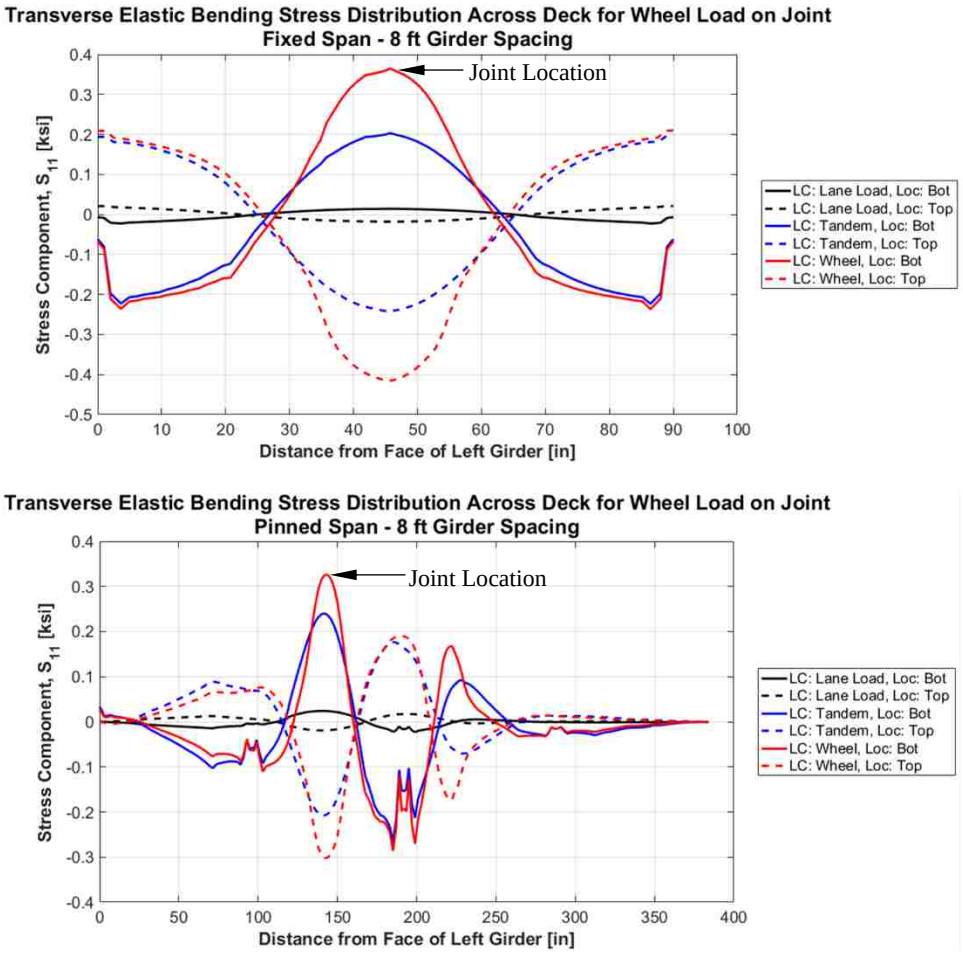

Figure 4.6. Transverse bending stress in the bridge deck due to a single-axle wheel load on the joint for the fixed configuration (above) and pinned configuration (below).

Analysis of the results from each model showed that the maximum tension stress at the joint was approximately 380 psi. The longitudinal bending stresses were similar in magnitude, but decayed much more quickly with respect to distance along the bridge span (see Appendix F.1). AASHTO specifies the modulus of rupture for concrete to be calculated as $0.24\sqrt{f_c'}$, which, for a typical DBT girder deck with 8,000 psi concrete, is approximately 700 psi. This suggests that the maximum design-level traffic loads, here taken as a 16 kip wheel load (half of the single axle), create bending demands on the deck that are well below the cracking stress. It should be noted that the FEA model included the haunch in the deck profile, and that is responsible for

drawing transverse moments away from the joint at midspan of the deck to the supports at the girder webs.

The prototype structure was significantly different from one that can be tested in the laboratory. The primary differences are associated with the geometry of the superstructure (haunched deck, girders, supports, etc.) and the influence of those entities on the moment distribution in the superstructure. Three possibilities can be envisaged:

1. Build a complete bridge in the laboratory and test it. Even for one joint width and one selection of bar offset, this option lay outside the resources available to the project by several orders of magnitude.
2. Build a section of the superstructure and test that. Two arguments exist against this option. First, the locations where the test structure ends but the real one continues must be replaced by boundary conditions that will reproduce the real internal actions, such as moments and shears in the deck. This is extremely difficult in practice and open to endless questioning after the test. Second, the difficulties and associated costs would still be great enough to allow testing of at most one joint width and one bar offset.
3. Use FEA to determine the moments and shears in the prototype deck. Use a statically determinate test setup to test joints in the laboratory and observe their response under the moments and shears predicted by the FEA, and possibly multiples of them.

Option 1 was clearly impossible. Option 2 allows only one configuration to be tested and the static indeterminacy introduces considerable uncertainty about the moments and shears in the location of greatest interest, namely the joint. This is particularly true with the haunched deck panels, which cause the majority of the wheel load to be resisted by negative moments at the

haunch. Consequently, a small discrepancy in stiffness of any part of the test specimen results in a significant discrepancy in the moment occurring at the joint.

Thus, Option 3 was selected. A statically determinate test structure was designed and built, resulting in the moment at the joint being known exactly for any applied load. Furthermore, the structure was simple enough that several combinations of joint width, clear cover, and bar offset could be investigated within the project resources and budget.

Chapter 5
EXPERIMENTAL TEST PROGRAM

The testing program involved four separate phases, most of which consisted of a series of physical experiments that aimed at determining the bond strength of the UHPC in a non-contact spliced connection by attempting to create the unique failure modes outlined in Appendix A. The testing phases were as follows:

1. Mixing
2. Material Strength Tests (including Strength versus Time)
3. Bond Curb Tests
    a. Pullout Bond Strength
    b. Splice-Connection Bond Strength
4. Simulated Deck Tests

The simulated deck experiments were the primary focus of this testing program which imitated a real bridge deck subjected to traffic loads. All the other experiments were used to isolate specific behavior to support and verify the simulated deck test results. Testing matrices for all experiments are provided in their respective sections.

Each specimen was tested after approximately 14 days of UHPC curing to simulate the demands of a construction schedule that cannot afford to be delayed by waiting for the concrete to gain strength.

The bond curbs and simulated deck joints cured at room temperature and humidity and were covered with multiple layers of soaked burlap which were rewet with cold water every day for four days, after which the concrete was exposed to the ambient environment. The standard material test specimens were cured in a controlled temperature/humidity room set at 73 °F and 100% humidity per ASTM C192 for the entire 14-day period[*] (ASTM International 2016). The conventional concrete compression cylinders were an exception because their actual strength was only required for analyzing the simulated deck results, thus they were tested after 267 days of curing in the controlled room when the simulated deck specimens were tested.

5.1 Mix Design

The material proportions specified by Qiao are provided in Table 5.1 (Qiao, Zhou and Allena 2017).

Table 5.1. Mix design quantities. Units: lbs/yd^3.

Water	Cement	Silica Fume	Sand	HRWRA	Steel Fibers	w/cm Ratio	Volumetric % of Steel Fibers
325	1500	260	1574	101	236	0.185	1.80

Sieve analysis results for the type of sand used for all mixes are provided in Appendix G.4.

For this UHPC to be a viable replacement for the proprietary Ductal® mix, it is desirable for the cost to be relatively low, which was a primary goal of Qiao's research. A cost analysis for each mix component is provided in Table 5.2 and Figure 5.1.

[*] For reasons out of this project's control, hot water was not available to the curing room for Simulated Deck specimens 3-8. As a result, the material specimens associated with these tests cured at 50 °F. See Appendix G.3 for further details.

Table 5.2. UHPC mix component providers and associated costs for this project.

	Manufacturer	Location	Unit Size	Cost per Unit	Cost per yd^3 of UHPC	Total Cost %
Cement	Lafarge	Seattle, WA	2,000 lbs/bag	~ $100.00 (bulk cost)	$75.00	5.2
Silica Fume	BASF Construction Chemicals	Seattle, WA	25 lbs/bag	$22.00	$228.80	15.9
Sand	Salmon Bay Sand & Gravel	Seattle, WA	50 lbs/bag	$5.52	$173.77	12.1
HRWRA	BASF Construction Chemicals	Seattle, WA	3 gal/bucket	$103.50	$396.75	27.6
Steel Fibers	Nycon Corporation	Fairless Hills, PA	16.5 lbs/bag	$39.25	$561.39	39.1

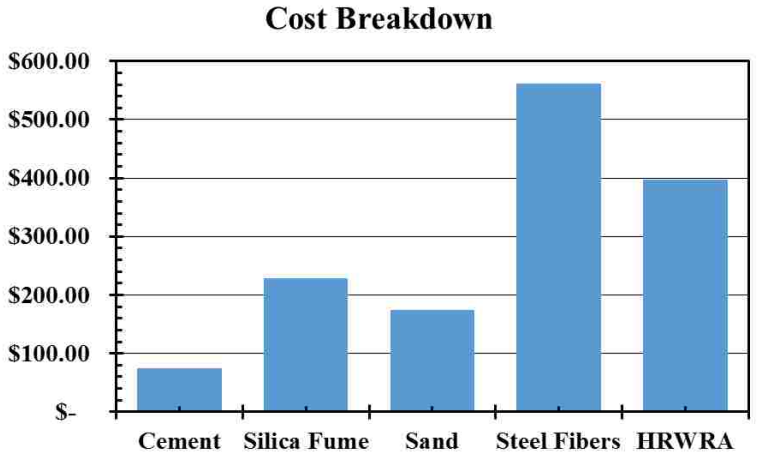

Figure 5.1. Cost breakdown of one cubic yard of UHPC.

Clearly, the steel fibers represented the most significant portion of the total cost. Since they are the primary contributor to UHPC tension performance, further research should be conducted to optimize the volume of steel fibers required. The work of Lee & Lee suggests that the fiber content could be reduced without loss of strength, at least up to yield of the rebar, although ductility would suffer. As is shown in Appendices G.4 and G.5, punching shear, rather than

flexure, controls the wheel load that can be applied. If the joint never reaches yield, there is no need for subsequent ductility, so a reduction in fiber content would be worth investigating.

5.2 Mix Procedure

Optimizing the mix procedure was not a feature of this project but it was necessary to determine the mixing procedure that worked best given the equipment and materials available. The typical mix procedure which was followed for each batch is provided in Appendix D.

5.3 Material Strength Tests

This section introduces the testing methods for each material strength test. All test phases were accompanied by a series of material strength tests to determine the tension and compression strength of the specific batch of UHPC used. General details of each material test are provided below in Table 5.3.

Table 5.3. Material strength specimen descriptions.

Material Test Specimen Name	Dimensions	Reference
Compression Cube	2” x 2” x 2”	ASTM C109 (ASTM International 2016)
Compression Cylinder	4”Ø x 8” (UHPC) 6”Ø x 12” (Conventional Concrete)	ASTM C39 (ASTM International 2017)
Split-Tension Cylinder	4”Ø x 8”	ASTM C496 (ASTM International 2011)
Flexural Beam	3” x 4” x 16”	ASTM C78 (ASTM International 2016)
Pullout Bond Cylinders	#5 epoxy-coated rebar embedded in 6”Ø x 4” cylinder and bonded over 1 inch	N/A (Custom Test)
Direct Tension	Reduced Section	N/A

	(3”x2” at ends, 2”x2” at middle)	(Custom Test)
Modulus of Elasticity Cylinder	4”Ø x 8”	ASTM C469 (ASTM International 2014)

This variety of material strength tests was necessary to determine what type of strength best correlated to the bond strength within a non-contact splice connection.

The edges of all material specimens were lightly ground smooth before loading to eliminate uneven edges and improve handling safety due to the sharp steel fibers. Material specimens which were not ASTM standards are described below. See Appendix E for further details of the ASTM-standard specimens.

Direct Tension

The direct tension material specimens are shown in Figure 5.2 and were intended to determine the UHPC’s direct tension strength calculated by Equation (2) and post-cracking performance.

$$f_{DT} = \frac{T}{B^2} \tag{2}$$

where B is the width of the specimen where failure occurred.

These specimens have reduced-section geometry with 1/2-inch diameter ASTM A307 Gr A Zinc Plated Low Carbon Steel threaded rods embedded in both of the end one-third sections. The threaded rods are assembled with a series of threaded rod couplers and steel plates in the 300-kip Baldwin® such that the specimen is loaded in tension (see Figure 5.2). Each threaded rod is extended 1 inch into the middle one-third section to ensure load transfer into the reduced geometry region.

These specimens follow the design used by Graybeal and Qiao. Graybeal did not use embedded threaded rods and performed the test by clamping the ends of the UHPC bar in the tension testing machine (Graybeal and Baby, Development of Direct Tension Test Method for Ultra-High-Performance Fiber-Reinforced Concrete 2013). That risks introducing bending moments as well as tension into the specimen unless the heads of the testing machine are aligned very accurately. The purpose of the threaded rods was to introduce a flexible element at each end that would cause the specimen to self-align. The two potentiometers on each side of the specimen read similar displacement values which suggests that the threaded rods were successful in minimizing bending moments.

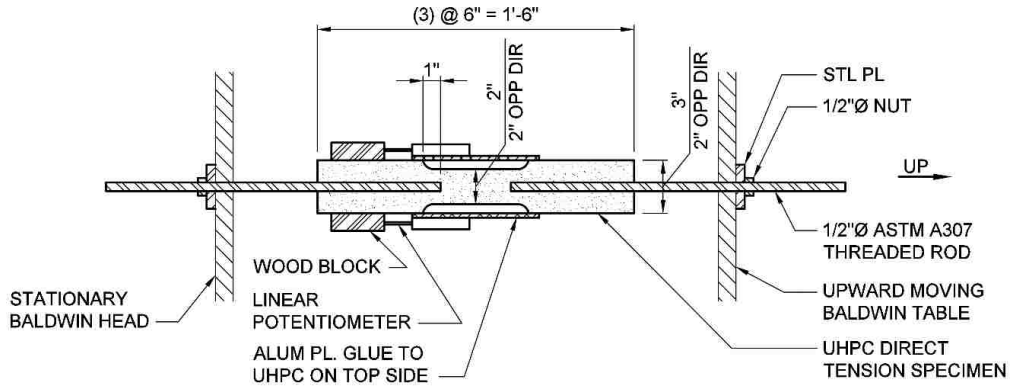

Figure 5.2. Direct tension specimen testing schematic design (longitudinal section view).

Note that each direct tension specimen failed through the beginning of the reduced geometry region at the end of the threaded rod. This suggests that there was not a uniform stress distribution at failure. If such tests are to be used in the future, the embedment of the bar should be such that it stops within the full-sized portion of the specimen and does not risk causing a stress concentration in the reduced section.

Pullout Bond Cylinder

Because tension and bond strength are the critical parameters for the behavior of a non-contact

spliced connection, these pullout bond cylinders provided a measure of the pure bond strength when failure occurs by reinforcement pullout. No ASTM standard procedure exists for testing bond strength of UHPC, so this experiment was developed. The goal was to measure bond stress using equipment that is simple enough to be available onsite so that bond tests could be performed quickly and locally if time was critical.

These experiments were designed based on the pullout test procedure for conventional concrete but to simulate realistic joint reinforcement, an epoxy-coated #5 rebar was cast in the center of a standard 6-inch diameter and 12-inch deep cylinder mold with the bottom 8 inches blocked out to create a 4-inch deep UHPC cylinder (ASTM International 2015). The test was then performed by placing a center-hole hydraulic ram with suitable plates over the rebar, gripping the bar with a 0.6-inch diameter prestressing strand anchor, and applying tension to the bar with the ram which induces bond stresses over the embedded length in the UHPC.

The desired failure mode is rebar pullout where the bar slips through the UHPC. This occurs after the rebar deformations mechanically anchor to the UHPC until the local bearing stresses exceed the bond capacity and the rebar pulls out, leaving a hole with diameter equal to the outer diameter of the rebar including deformations.

In the initial tests, the full four inches of rebar were bonded to the UHPC and this resulted in a radial splitting pattern. The test specimen was then re-designed to reduce the ratio of splitting demand to splitting resistance. This was done by maintaining the gross dimensions, but bonding only a short length of the bar within the concrete. Only the center 1 inch of the rebar was bonded to the UHPC. The remaining two 1.5-inch regions were debonded using duct tape that was thick enough to prevent the rebar deformations from mechanically interlocking with the UHPC. By this means, a high bond stress could be induced without introducing high hoop tension stresses,

resulting in pullout failures with greater ductility and lower variability. The bond stress was treated as being constant over the 1-inch bonded length and was calculated per Equation (3).

$$\tau_b = \frac{T}{\pi d_b L_e} \tag{3}$$

where d_b is the bar diameter and L_e is the embedment length.

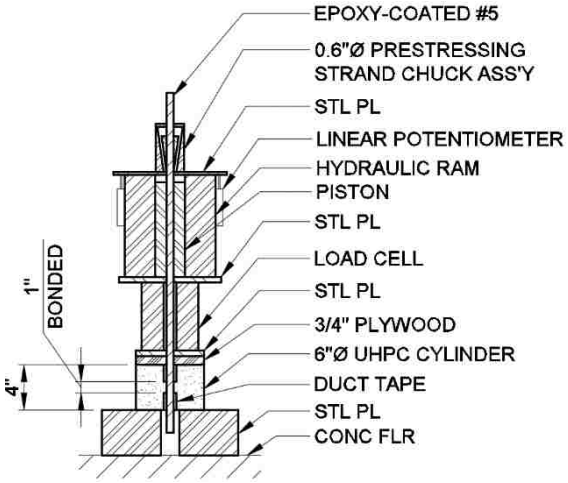

Figure 5.3. Cross-section view of a representative pullout cylinder with testing apparatus.

5.4 Strength Gain with Time Tests

UHPC joints are one of the final steps in the bridge construction process so it would be impractical and costly to wait longer than necessary until the bridge is opened for use. The maximum age was chosen to be 14 days instead of the conventional 28 days for this very reason. The strength gain with time tests (henceforth referred to as S/T tests) intended to relate the 14-day experimental data to different curing ages such that the optimum age can be determined from a strength and construction perspective on a project-by-project basis.

These tests use most of the material specimens outlined in Chapter 5.3 and the testing matrix for all S/T tests is provided in Table 5.4.

Table 5.4. Testing matrix for the S/T tests showing the number of specimens tested at each day.

Age [days]	Compression Cubes	Compression Cylinders	Split-Tension Cylinders	Flexural Beams	Direct Tension	Pullout Bond Cylinders
1	3	3	3	3	2	3
2	3	3	3	3	2	3
3	3	3	3	3	2	3
4	3	3	3	3	2	3
7	3	3	3	3	2	3
14	3	3	3	3	2	3

5.5 Bond Curb Tests

A series of bond curb experiments replicated the performance of a UHPC joint between adjacent DBT girders. One curb experiment aimed to determine the pure pullout bond strength of epoxy-coated reinforcement and the other determined the bond strength in a realistic non-contact spliced connection.

5.5.1 Pullout Bond Curb Test

The overarching goal of the pullout curb tests is to gain an understanding of the pullout bond strength of UHPC in a realistic configuration that resembles the joint geometry of a DBT girder bridge. The test configuration differed from that of the bond cylinder in that splitting of the side face was possible in these tests, whereas it was prevented in the Pullout Bond Cylinder by choice of the dimensions. Each pullout curb consists of a 7-inch wide rectangular curb with #5 epoxy-coated rebar spaced at 6 inches on-center and with different lengths of embedment. See Figure 5.4 and Figure 5.5 for a schematic of the testing apparatus and Appendix E.1 for a detailed description of each specimen. The timber blockouts at the base of each specimen shown in the figures were used to provide sufficient embedment length while reducing the amount of UHPC material needed.

Three curbs were included in the testing program with clear covers of 1 inch, 1.75 inches, and 2.5 inches. WSDOT standard details specify 1-inch clear cover for the bottom layer of deck reinforcement (Washington State Department of Transportation 2016). To increase the cover and determine its strength influence, the cover was increased in 0.75-inch increments to resemble the practical use of 3/4-inch plywood or a piece of 1x2 lumber.

The testing matrix for the pullout curbs is provided below in Table 5.5.

Table 5.5. Pullout curb test schedule with embedment lengths. Units: inches.

Curb 1 1-inch Clear Cover	Curb 2 1.75-inch Clear Cover	Curb 3 2.5-inch Clear Cover
1.5	3	3
3	4.5	4.5
4.5	6	6
6	7.5	7.5
7.5	9	9
9	10.5	10.5

An important feature of these experiments was that the loading assembly bore directly on the UHPC curb which provided a compressive reaction that follows the statically determinate load path to the top of the UHPC curb and offered restraint against tension failure modes.

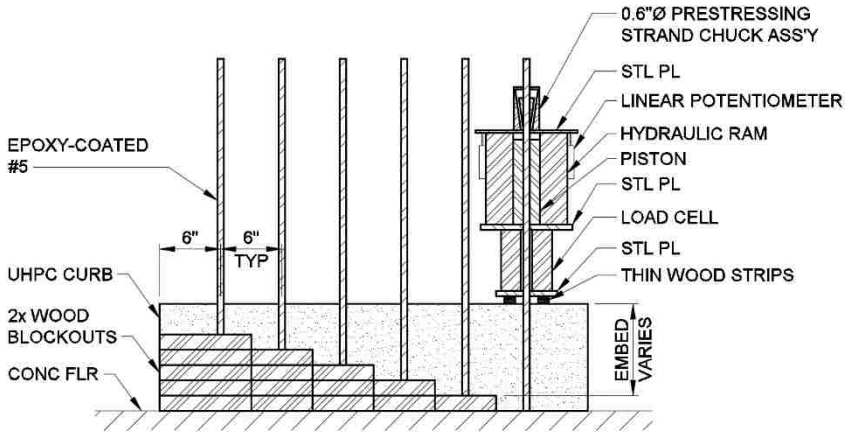

Figure 5.4. Longitudinal section view of a pullout curb with testing apparatus shown on one specimen.

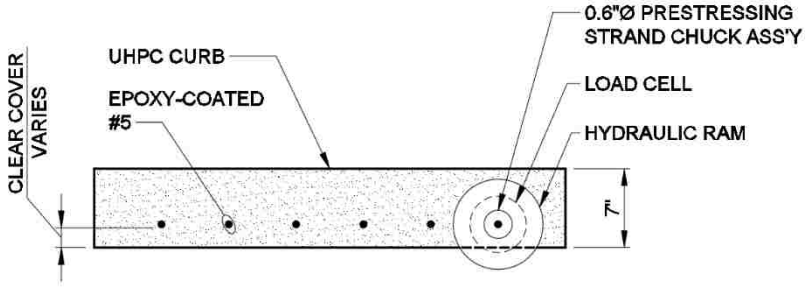

Figure 5.5. Plan view of a pullout curb with testing apparatus shown on one specimen.

5.5.2 Splice-Connection Bond Curb Test

The spliced-connection curbs are designed similarly to the pullout curbs with two important exceptions. The first was that the epoxy-coated reinforcement needed to be spliced with other reinforcement to resemble the non-contact splice connection within the UHPC joint. To achieve a spliced connection, #8 rebars projected from a large conventional concrete base block and the epoxy-coated #5 rebars were positioned between them. The second exception is that the loading assembly was seated on a standoff which bypassed the UHPC curb and prevented a compressive reaction into the curb. This allowed for the connection's performance to be governed solely by the spliced force transfer mechanism and allowed tension failure modes to occur. See Figure 5.6 and Figure 5.7 for a schematic of the testing apparatus and Appendix E.2 for a detailed description of each specimen. Again, different simulated joint widths were achieved by blocking out the bottom of the formwork.

Three curbs were included in the testing program with clear covers of 1 inch, 1.75 inches, and 2.5 inches, using the same reasoning as for the pullout curbs.

The testing matrix for the splice curbs is provided in Table 5.6.

Table 5.6. Splice curb test schedule with splice lengths. Units: inches.

Curb 1 **1-inch Clear Cover**	**Curb 2** **1.75-inch Clear Cover**	**Curb 3** **2.5-inch Clear Cover**
3	1.25	0.25
3.75	2	1
4.5	2.75	1.75
5.25	3.5	2.5
6	4.25	3.25
	5	4

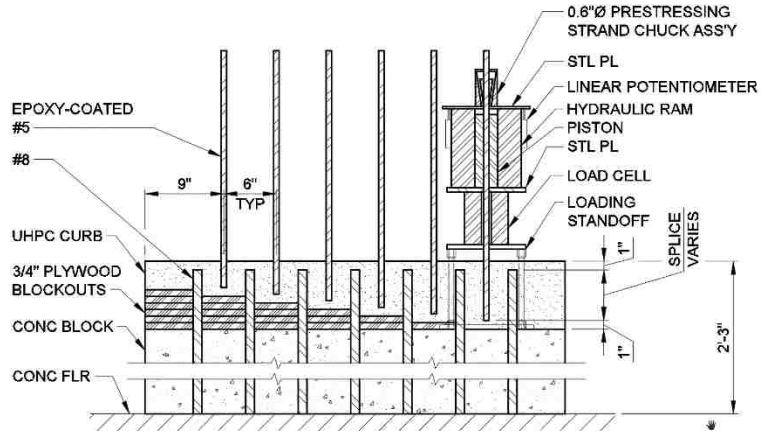

Figure 5.6. Longitudinal cross-section through a representative splice curb with testing apparatus shown on one specimen.

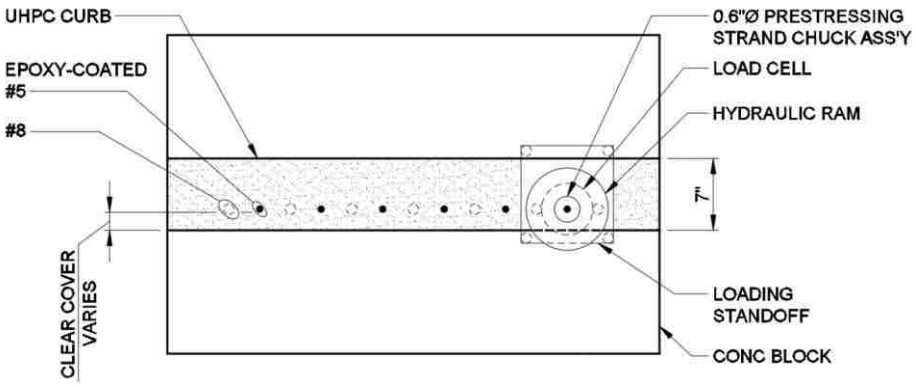

Figure 5.7. Plan view of a representative splice curb with testing apparatus shown on one specimen.

5.6 Simulated Deck Tests

This final series of experiments determined the UHPC joint's performance in the most realistic application. These experiments were representative of a region of a bridge deck that is subjected to positive bending moment demands resulting from a single maximum wheel load centered on the joint, as depicted by Figure 5.8.

Since a real bridge deck subjected to wheel loading is a statically indeterminate system with complications due to nonprismatic geometry, the bending moment at the joint must be found

with FEA, as was shown in Chapter 4. That bending moment is approximately constant over a short length of the joint, so it is satisfactory to build and test statically determinate specimens that focus on the joint region, so the induced moments can be determined with certainty and compared with the demands.

Figure 5.8. Positive bending demand on the UHPC joint from traffic loads.

Each specimen resembled a two-foot wide strip of bridge deck. It is shown in a 3D image of the test apparatus in Figure 5.9 with detailed sketches in Figure 5.10 through Figure 5.12. See Appendix E.3 for a detailed description of each specimen. The tests were conducted upside down with an upwards load applied at midspan by a hydraulic jack beneath the specimen. This was done to facilitate the use of the Optotrak® digital camera tracking system and to simplify visual observations.

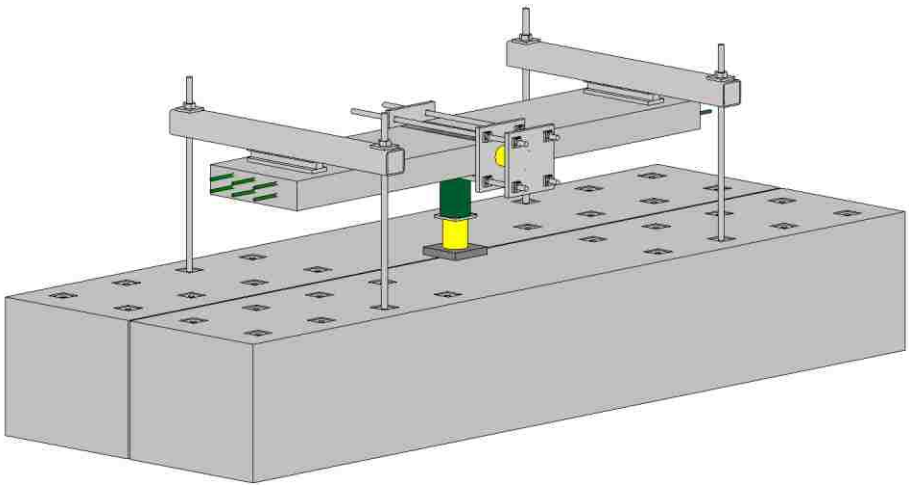

Figure 5.9. 3D model of the simulated deck test apparatus.

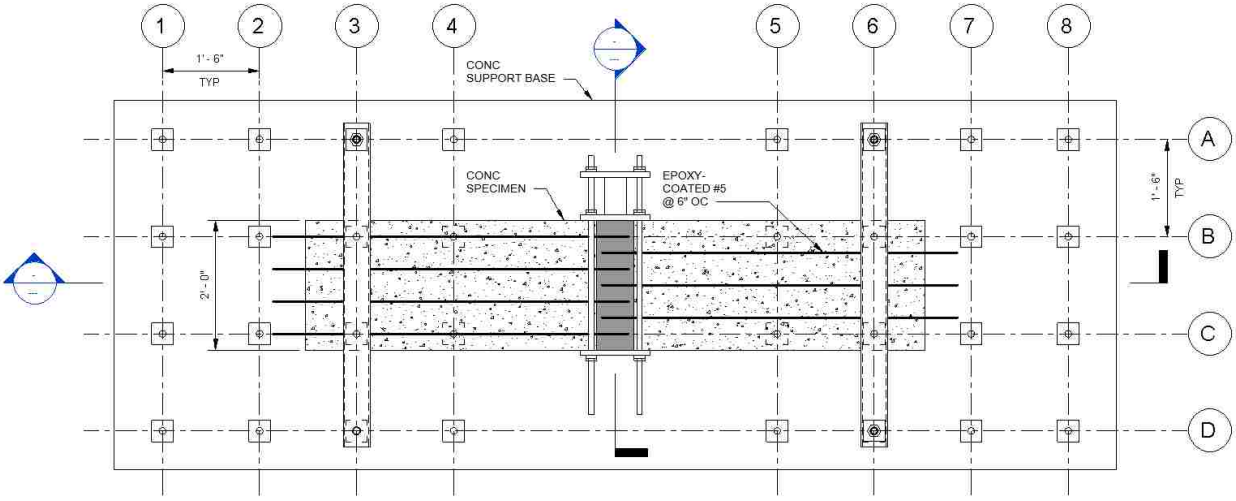

Figure 5.10. Plan view of the simulated deck test apparatus.

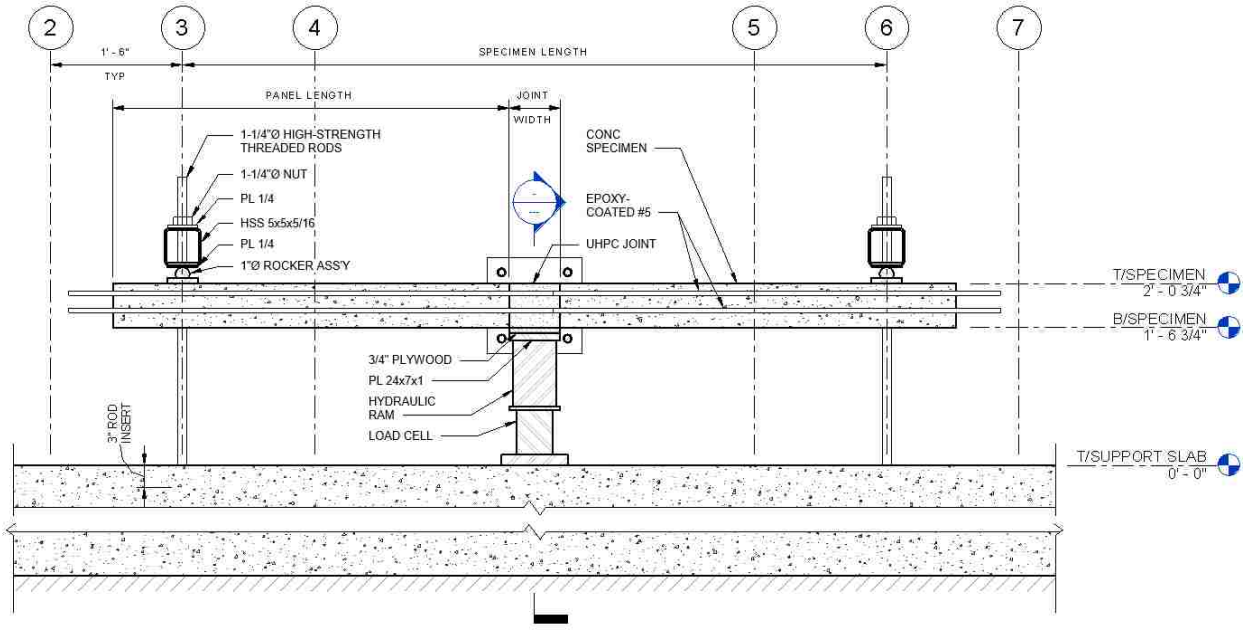

Figure 5.11. Longitudinal section view of the simulated deck test apparatus.

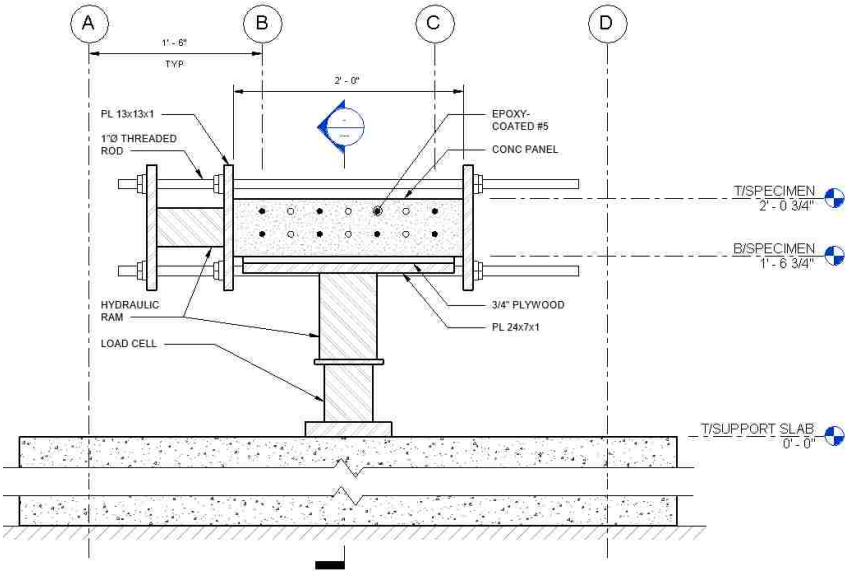

Figure 5.12. Transverse section view of the simulated deck test apparatus.

The critical parameters investigated with these experiments were joint width, clear cover, and lateral rebar offset. The testing schedule for these experiments is provided in Table 5.7. The deck test age represents the age of the UHPC at the time the simulated deck specimens were tested, and the material test age represents the age of the UHPC at the time the standard and

custom material strength tests were performed since it was not possible to perform both series of tests on the same day.

Table 5.7. Testing schedule for flexural simulated deck experiments.

	Joint Width [in]	Clear Cover [in]	Rebar Lateral Offset [in]	Deck Test Age [days]	Material Test Age [days]
Specimen 1	7	1	0	16	14
Specimen 2	3	1	0	18	14
Specimen 3	5	1	0	11	13
Specimen 4	5	1	2	12	13
Specimen 5	5	1	1	9	11
Specimen 6	6	1	0	10	11
Specimen 7	5	1.75	0	13	15
Specimen 8	6	1.75	0	16	15

The lateral rebar offset is investigated to determine the effect of construction tolerances on reinforcement and girder placement. Ideally, the flange reinforcement in DBT girders is spaced at 6-inches on-center, thus creating a spliced connection where the rebar is spaced at 3-inches on-center. If the flange reinforcement is not located exactly or if the girders are not perfectly aligned, this 3-inch spacing within the connection will not be constant and may affect the connection strength.

Chapter 6
EXPERIMENTAL RESULTS

In this chapter, the experimental results are summarized. The material property tests are presented first in Sections 6.1 and 6.2, followed by the bond curb test results in Section 6.3, and finally the simulated deck test results in Section 6.4. Further details of each test's results are given in Appendix E.

6.1 Material Test Results

The 14-day strengths for each individual batch of UHPC as well as the average strength of all batches are provided in Table 6.1.

The cube and cylinder compression strength specimens exhibited very consistent results (coefficients of variation less than 7%) whereas all tension strength specimens were slightly less consistent. More meaningful for this project is the consistency of the bond strength, which surpassed that of all other material specimens with a coefficient of variation of 4.5%.

See Appendix A.1 for histograms of the 14-day strength distribution for all material specimens.

Table 6.1. 14-day material test strength results. Units: ksi.

	Compression Cubes	Compression Cylinders (UHPC)	Compression Cylinders (Conventional Concrete)	Split-Tension Cylinders	Flexural Beams	Direct Tension	Pullout Bond Cylinder	Modulus of Elasticity Cylinders
Pullout Curb Splice Curb 1" Cover	14.09	12.79	N/A†	1.86	2.74	0.79	N/A†	N/A†
Pullout Curb 1.75" & 2.5" Cover	16.55	12.94	N/A†	N/A†	2.87	1.43	N/A†	N/A†
Splice Curb 1.75" Cover	15.76	12.76	N/A†	2.19	2.48	0.93	N/A†	N/A†
Splice Curb 2.5" Cover	15.74	12.54	N/A†	2.16	2.75	0.97	N/A†	N/A†
Simulated Deck Specimen 1 & 2	15.08	12.47	10.80	2.11	2.92	0.99	6.83	N/A†
Simulated Deck‡ Specimen 3 & 4	14.21	14.07	10.80	2.31	1.94	0.78	6.39	N/A†
Simulated Deck‡ Specimen 5 & 6	13.27	13.07	10.80	2.22	2.11	0.75	6.37	4,720
Simulated Deck‡ Specimen 7 & 8	13.73	12.76	10.80	2.41	2.13	0.80	6.52	5,240
TOTALS								
Number§	45	29	8	30	27	25	12	6
Average	**15.95**	**13.10**	**10.80**	**2.16**	**2.65**	**0.96**	**7.12**	**4,980**
Standard Deviation	**1.08**	**0.81**	**0.49**	**0.39**	**0.33**	**0.16**	**0.32**	**370**
Coefficient of Variation	**0.068**	**0.062**	**0.046**	**0.18**	**0.12**	**0.17**	**0.045**	**0.074**

† N/A denotes batches where the specific material specimen was not created.
‡ Results are artificially scaled due to curing condition described in Footnote * on Page 7. See Appendix G.3 for details.
§ This refers to the quantity of material specimens which were tested after approximately 14 days of curing (267 days for the conventional concrete compression cylinders).

6.2 Strength Gain with Time Test Results

The speed at which strength is gained is of interest, particularly for Accelerated Bridge Construction projects, in which the duration of site operations may be critical. ACI Committee 209 specifies the following equation when attempting to model the strength of ordinary concrete with time (ACI Committee 209 2008):

$$f_c'(t) = f_{c,28}'\left(\frac{t}{a + bt}\right) \quad \textbf{(4)}$$

where the coefficients *a* and *b* vary depending on the type of cement used as well as curing temperature. For example, for Type I cement, *a* and *b* are assigned the values 4 and 0.85, respectively (ACI Committee 209 2008). Note that, for the equation to be valid at 28 days, the parameters must satisfy $b = 1 - a/28$, so the equation has only one parameter that can be chosen freely.

A least-squares residual analysis can be performed to determine these coefficients for all the material tests performed, using the 14-day strength in place of the conventional 28-day strength. This is provided below in Equation (5) and the coefficients for each material test are provided in Table 6.2.

$$f_c'(t) = f_{c,14}'\left(\frac{t}{a + bt}\right) \quad \textbf{(5)}$$

A parameter of interest using this relationship is the time required for the UHPC to gain 50% of its 14-day strength which can be calculated using Equation (6).

$$t_{50} = \frac{a}{2 - b} \quad \textbf{(6)}$$

Table 6.2. Parameters for strength gain with time to be used with Equation (5).

	a	b	r^2	t_{50} [days]
Compression Cube	2.03	0.83	0.95	1.74
Compression Cylinder	1.38	0.84	0.97	1.20
Split-Tension Cylinder	1.89	0.94	0.93	1.78
Flexural Beam	1.88	0.96	0.91	1.81
Direct Tension	0.97	0.96	0.98	0.94
Pullout Bond Cylinder	0.98	0.90	0.98	0.89

A plot for each material test is generated using Equation (5) and is provided in Appendix F.4. Table 6.2 shows that, in all the tests, half of the 14-day strength was reached in less than 2 days.

6.3 Bond Curb Test Results

The two most common failure modes were splitting of the UHPC which occurred both before and after the rebar yielded, and rebar fracture. The splitting usually occurred on the side face of the specimen (see the photographs in Appendices K.2 and K.3). Load-displacement curves corresponding to these failure modes are shown in Figure 6.1.

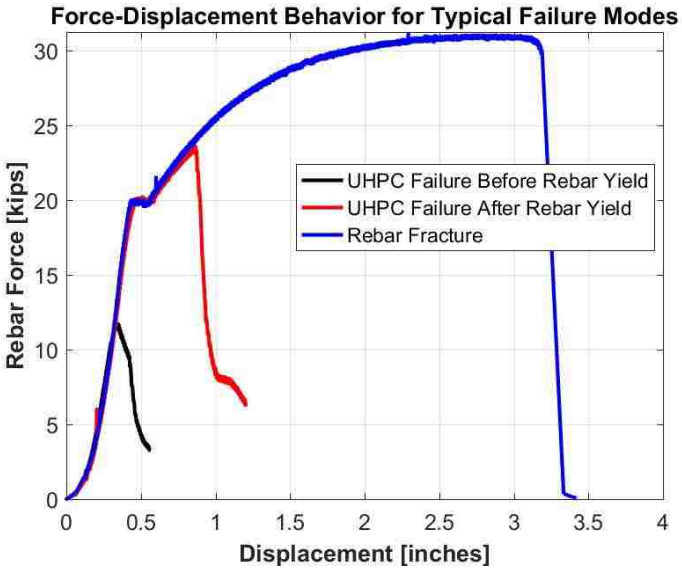

Figure 6.1. Load-deflection curves corresponding to typical failure modes.

As a general trend, the "UHPC Failure Before Rebar Yield" is more representative of failure with short embedment lengths whereas the "UHPC Failure After Rebar Yield" is representative of failure with longer embedment lengths.

6.3.1 Pullout Curb Test Results

The bar stress at failure for each specimen was plotted in Figure 6.2 with respect to the embedment length. The stress is based on the nominal bar area of 0.31 square inches.

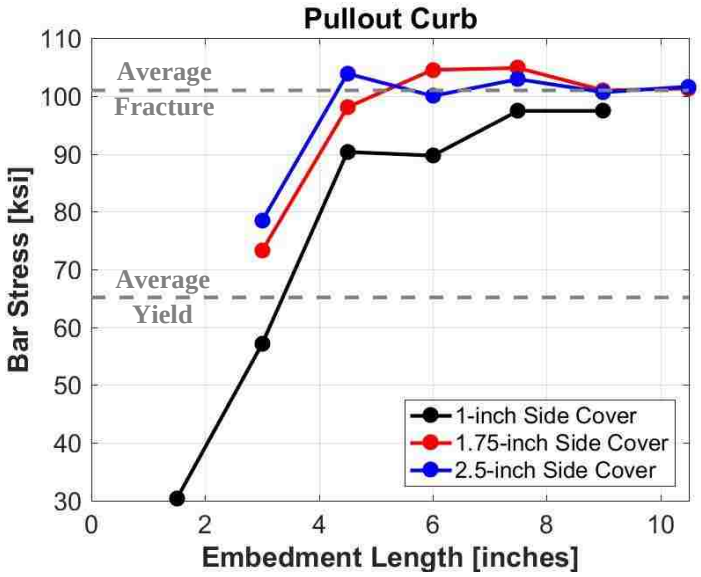

Figure 6.2. Bar stress versus embedment length plot for all pullout curbs[**].

Some specimens exhibited pullout and splitting behavior, but the primary failure mode was splitting, as shown in Figure 6.3. The failure mode for each specimen is outlined in Table 6.3. Specimens with small embedment lengths showed the most pullout and breakout behavior anywhere in the range of zero to 2.5 inches of slip. Figure 6.2 shows that rebar fracture was achieved with embedment lengths around $10d_b$ (6.25 inches). Each curve corresponding to a different clear cover has a fairly similar slope. They are grouped together closely. For any embedment length, a slight strength gain can be seen between covers of 1.0 inches and 1.75 inches, but further increase to 2.5 inches offers no corresponding increase in strength. This suggests that the thickness of the clear cover, at least within the range tested, had little effect on strength.

Photographs of each specimen which show the various types of structural damage are provided in Appendix K.

[**] The 1-inch cover specimen used rebar from a separate steel batch which had a slightly lower fracture point.

Figure 6.3. Typical structural damage observed during bond curb experiments.

Table 6.3. Failure mechanisms for each pullout curb specimen.

1-inch Clear Cover				1.75-inch Clear Cover				2.5-inch Clear Cover			
L_e [in]	f_s [ksi]	f_t [ksi]	Failure Mode	L_e [in]	f_s [ksi]	f_t [ksi]	Failure Mode	L_e [in]	f_s [ksi]]	f_t [ksi]	Failure Mode
1.50	30.3	1.86	Splitting								
3.0	57.1	1.86	Splitting	**3.0**	73.2	2.19	Splitting	**3.0**	78.4	2.16	Splitting
4.50	90.3	1.86	Splitting	**4.5**	98.1	2.19	Splitting	**4.5**	103.9	2.16	Fracture
6.0	89.7	1.86	Splitting	**6.0**	104.5	2.19	Fracture	**6.0**	100.0	2.16	Fracture
7.5	97.4	1.86	Fracture	**7.5**	104.8	2.19	Fracture	**7.5**	102.9	2.16	Fracture
9.0	97.4	1.86	Fracture	**9.0**	101.0	2.19	Fracture	**9.0**	100.6	2.16	Fracture
				10.5	101.3	2.19	Fracture	**10.5**	101.6	2.16	Fracture

Despite the naming convention, pure pullout failure (without splitting) was not observed during any pullout curb test which shows that, for the range of clear covers tested, the pullout strength of UHPC is significantly greater than the tensile splitting strength for all embedment lengths. Only after the UHPC's tensile strength was reached did significant slip occur. If cover greater than 2.5 inches was provided, the failure mechanism might be expected to transition from splitting to pullout or breakout, but such large cover would likely be impractical.

6.3.2 Splice-Connection Curb Test Results

The behavior of each specimen closely resembled the behavior of each Pullout Bond Curb specimen with the exception that conventional breakout deformations like those seen in Figure 6.4 were observed in addition to pullout and splitting. Breakout in concrete occurs when the tensile capacity is exceeded and the specimen fails along a cone-shaped failure surface as depicted in Appendix Figure A.7.

Figure 6.4. Breakout deformations observed after testing splice-connection curb specimens.

A summary of failure mechanisms for all splice-connection curb specimens is provided in Table 6.4 and the experimental data is also plotted in Figure 6.5. This figure shows rebar fracture with splice lengths around $7d_b$ (4.375 inches). The splice length is the distance by which adjacent bars overlap. The data for each clear cover value are plotted as separate curves. As with the Pullout Bond Curbs, the curves have similar slopes and are grouped together closely. This suggests, again, that clear cover had little effect on strength.

Note that the tension strength of the UHPC was slightly difference for each cover thickness (the specimens were cast in different batches), as was the bar strength. They were both lowest for the 1-inch cover curb. Normalization with respect to either bar strength or UHPC tension strength

would thus raise the strengths of the 1-inch cover results and reduce to almost nothing the difference between the results for different covers.

That finding suggests that, between 1-inch and 2.75-inch, cover has no effect on splice strength. However, that conclusion is at odds with the data in Table 6.4 which show that additional cover reduced the embedment length at which failure transitioned from splitting to bar fracture. The test arrangements between the two bond curbs were different, so the results are not directly comparable. However, it is concluded that cover thickness does affect bond and splice strength, but, in the range of clear cover studied, the effect is small enough to make little difference in practice.

Table 6.4. Splice-connection curb results summary.

1-inch Clear Cover				**1.75-inch Clear Cover**				**2.5-inch Clear Cover**			
L_{spl} **[in]**	f_s **[ksi]**	f_t **[ksi]**	**Failure Mode**	L_{spl} **[in]**	f_s **[ksi]**	f_t **[ksi]**	**Failure Mode**	L_{spl} **[in]**	f_s **[ksi]]**	f_t **[ksi]**	**Failure Mode**
								0.25	11.0	2.16	Pullout
				1.25	37.4	2.19	Splitting	**1.00**	25.5	2.16	Pullout
				2.00	58.4	2.19	Splitting	**1.75**	37.1	2.16	Pullout
3.00	66.8	1.86	Splitting	**2.75**	75.5	2.19	Pullout	**2.50**	55.8	2.16	Splitting
3.75	85.2	1.86	Splitting	**3.50**	90.3	2.19	Pullout	**3.25**	90.3	2.16	Splitting
4.50	94.5	1.86	Splitting	**4.25**	100.0	2.19	Fracture	**4.00**	96.8	2.16	Splitting
5.25	95.2	1.86	Fracture	**5.00**	99.7	2.19	Fracture				
6.00	95.5	1.86	Fracture								

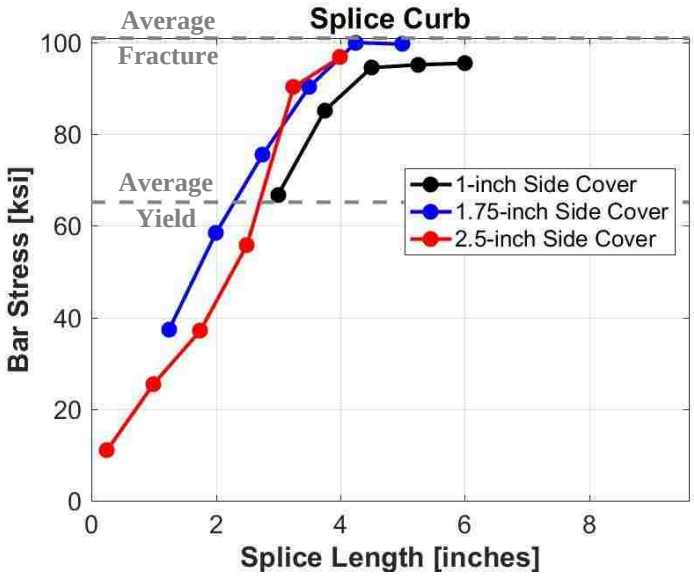

Figure 6.5. Bar stress versus splice length plot for all splice curbs[††].

6.4 Simulated Deck Test Results

The primary data measured for these tests is the UHPC joint's bending capacity for any given joint width. The peak bending moment at the interface between the deck panel with three reinforcing bars and the UHPC joint is listed in Table 6.5 along with the split-tension cylinder strength of each joint. Figure 6.6 depicts the full normalized bending moment versus midspan displacement data and the peak bending moment for each specimen is plotted against joint width in Figure 6.7. Maximum moment at the middle of the UHPC joint plotted against the joint width.

Table 6.5. Parameters for all simulated deck experiments.

Specimen	Joint Width/Cover/Offset [in]	Interfacial Bending Moment [k-in]
Specimen 1	7/1.00/0	562.2

[††] The 1-inch cover specimen used rebar from a separate steel batch which had a slightly lower fracture point.

Specimen 2	3/1.00/0	245.8
Specimen 3	5/1.00/0	391.7
Specimen 4	5/1.00/2	336.9
Specimen 5	5/1.00/1	400.6
Specimen 6	6/1.00/0	474.1
Specimen 7	5/1.75/0	487.4
Specimen 8	6/1.75/0	471.5

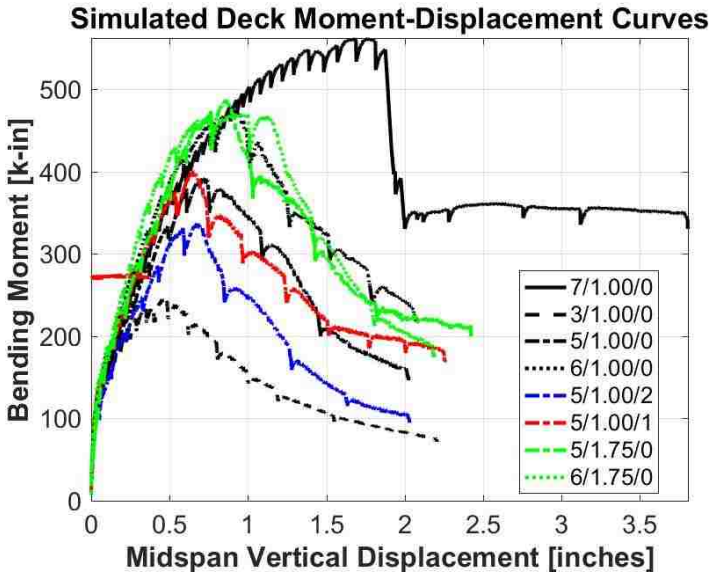

Figure 6.6. Bending moment versus midspan displacement curves for all simulated deck tests. The legend notation is Joint Width/Clear Cover/Rebar Offset.

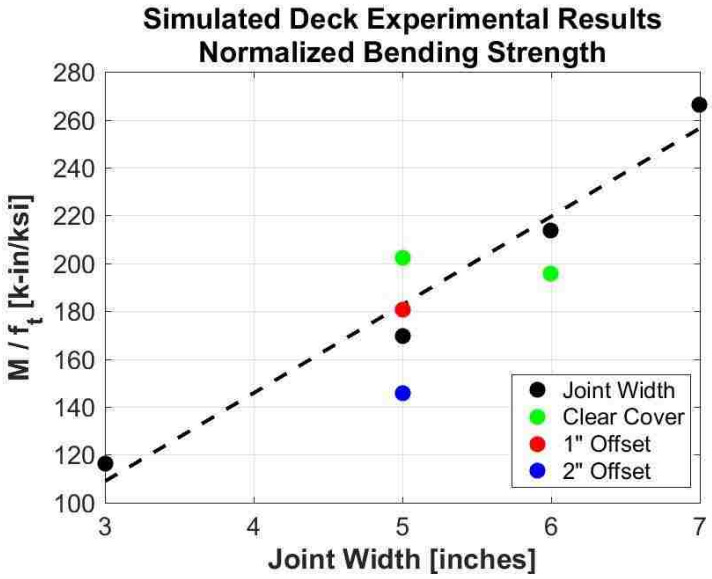

Figure 6.7. Maximum moment at the middle of the UHPC joint plotted against the joint width.

There exists a relatively linear relationship between maximum bending moment and joint width with a coefficient of determination of 0.97. As was shown with the bond curbs, clear cover did not seem to have a significant effect on strength. The five-inch joint width specimen displayed increased capacity with additional cover but the six-inch joint width specimen displayed decreased capacity. The one-inch lateral offset did not affect the strength of the connection whereas there was a clear strength decrease of approximately 14% with the two-inch lateral offset, in which the spliced bars were essentially in contact.

Each specimen failed by the same tension splitting that caused failure in the bond curbs. Surface cracks propagated through the joint width and were observed on the surface of the joint during each experiment. However, cover splitting did not cause failure. The steel fibers were able to sufficiently bridge these cracks and provide additional strength and ductility to the joint until the horizontal split shown in Figure 6.8 formed through the plane of the tension rebar.

Figure 6.8. Tension splitting planes through the cover (top) and between rebar (bottom).

During each experiment, there was no indication of flexural cracks within the body of the UHPC. The cracking was all concentrated at the interface between the two materials, as shown in Figure 6.9. The size of the interfacial crack was monitored by the Optotrak® camera system and its growth with respect to the applied load is provided in Figure 6.10.

Figure 6.9. Interfacial cracking.

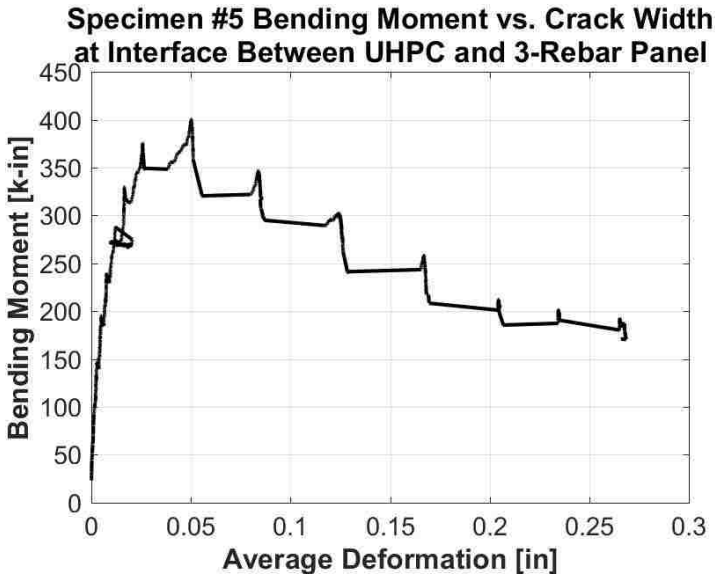

Figure 6.10. Typical bending moment versus interfacial crack width for the interface between the UHPC joint and conventional concrete panel.

This figure is representative of all specimens and shows that the interfacial crack did not begin to open until an approximate bending moment of 100 kip-inches which corresponds to an elastic stress of approximately 690 psi.

Chapter 7
ANALYSIS AND COMPARISON OF RESULTS

7.1 Material Strength

The different researchers mentioned in Chapter 2 all performed material strength tests to some degree (mix designs are given in Table 7.1 and specimen sizes in Table 7.2) and their results are compared to the results of this program in Figure 7.1.

Table 7.1. UHPC mix designs from other organizations.

	Water	Cement	Silica Fume	BF Slag	Gypsum	Sand	Coarse Aggregate	HRWRA	Steel Fiber
Qiao	325	1500	260	0	0	1574	0	101	236
Graybeal	219	1200	390	0	0	1720	0	50	263
Lee & Lee	253	966	179	297	46	962	1461	0	212
Karmout	303	1011	157	0	0	530	1670	30	0

Table 7.2. Material specimen sizes used by other UHPC programs.

	Testing Age [days]	Compression Cube	Compression Cylinder	Split-Tension Cylinder	Flexural Beam	Direct Tension
This Project	14	2”	4”Ø x 8”	4”Ø x 8”	3” x 4” x 16”	2” x 2” (reduced section)
Qiao	14	2”	N/A	6”Ø x 12”	3” x 4” x 16”	2” x 2” (reduced section)
Graybeal	28	2”	3”Ø x 6”	6”Ø x 12”	3” x 4” x 16”	2” x 2” x 12” (prismatic)
Lee & Lee	28	N/A	?	N/A	?	N/A

Karmout	14	4”	N/A	6”Ø x 12”	4” x 4” x 20”	N/A

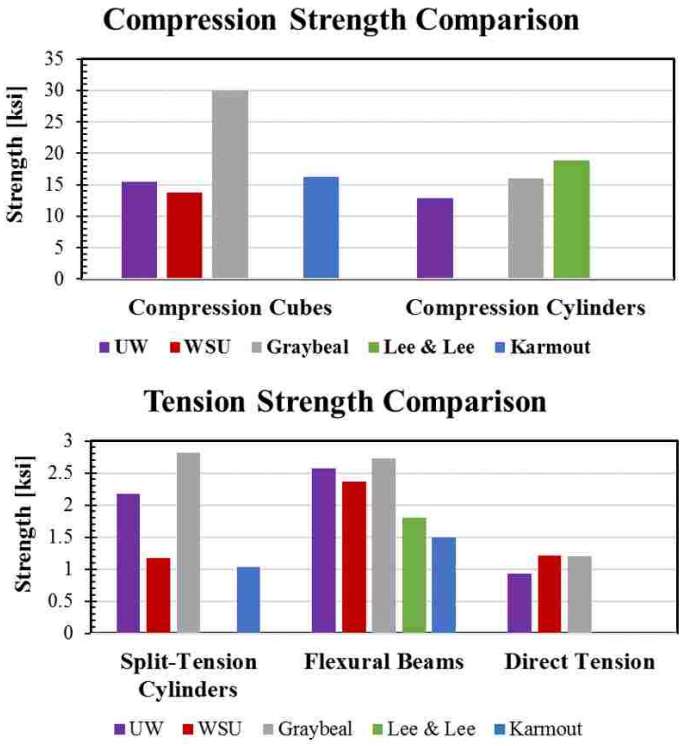

Figure 7.1. Material strength comparison.

Graybeal’s tests on Ductal® clearly exhibit the highest cube compression strength but his compression cylinders are more consistent with the results from the other organizations. It should be noted that his tests were conducted at 28 days, whereas those conducted by others were at 14 days. Compression cubes are typically stronger than cylinders because of the friction on the loading head which inhibits lateral expansion near the loading surfaces and affects the small cubes more than the taller cylinders. Typical cube-to-cylinder strength ratios for conventional concrete are on the order of 1.25 which is close to what was found in this project. Because the fibers in UHPC already provide considerable confinement, the additional confinement provided by friction at the test platen might be expected to play a smaller role, in which case the cube/cylinder ratio would be expected to be closer to 1.0 for UHPC. However,

Graybeal's ratio is closer to 2.0, suggesting that his cube strengths are an outlier in strength prediction.

Since compression strength is not of significant interest for longitudinal non-contact spliced joints, the main comparison should focus on tension strength, which was measured in three ways. In all cases, the results found here were lower than Graybeal's, but the differences were about 21%, 4%, and 25% for the split-tension cylinder, flexural beam, and direct tension tests, respectively. The direct tension results may have been adversely affected by the stress concentration noted in Section 5.3. On average, the tension strengths achieved in this testing program were about 85% of Graybeal's.

An additional benefit of UHPC apart from strength is its ductility and post-cracking performance. In direct tension tests, the Ductal® UHPC maintained the initial peak load over a wide strain range and experienced crack straining where the specimen gained additional strength while a wide cracking field formed as seen in Figure 7.2.

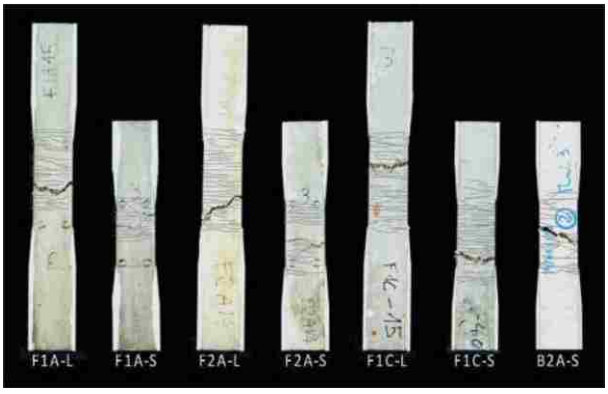

Figure 7.2. Ductal® UHPC direct tension cracking field.

Figure 7.3 depicts a sample direct tension stress-strain relationship which not only shows excellent tension strength but also substantial ductility due to maintaining the peak load (Yuan and Graybeal 2014). The direct tension response for the UHPC mix developed by Qiao was able

to achieve comparable peak stresses but was less ductile, as illustrated in Figure 7.4. In those specimens, the cracking at the peak load was typically concentrated at a single location, after which the strength dropped fairly rapidly to a constant value of approximately 40-50% of the peak strength. If a gage length of 4 inches is assumed, then the direct tension specimens hold approximately 50% of its strength at 1.25% strain. While the same degree of ductility and post-cracking strength was not observed during this testing program as it was with Graybeal's (Graybeal observed minimal net strength loss at 1.25% strain), the UHPC still displayed a meaningful contribution from the steel fibers to prevent a complete loss in post-peak strength.

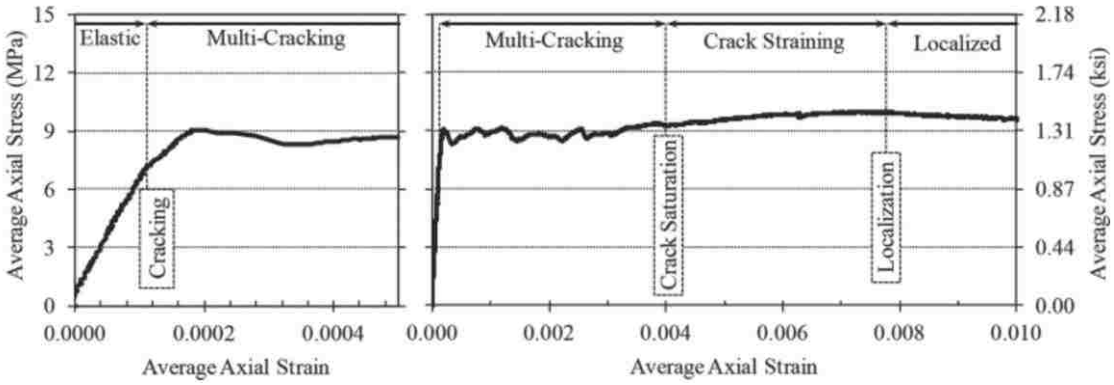

Figure 7.3. Ductal® UHPC direct tension performance. Axial strains are calculated using a gage length of 3 inches.

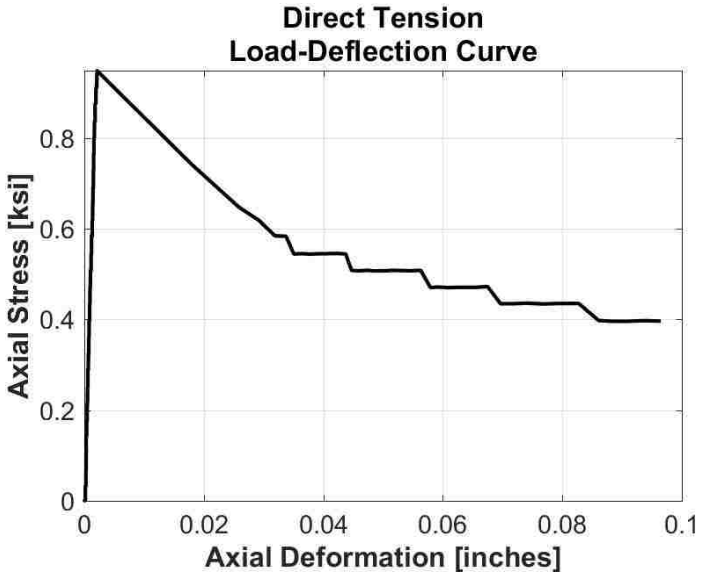

Figure 7.4. Typical direct tension test load-deflection curve (this research).

In the split-tension cylinder strength tests, this project's and Qiao's results, which both used the same mix design, differed by a factor of approximately two, but the cylinder sizes differed. The UW results were still approximately 20% lower than Graybeal's. The flexural beam tests showed comparable results in all three test programs.

Karmout's UHPC did not contain any steel fibers; it only focused on having varied particle sizes (Karmout, Arafa and Shihada 2009). This clearly helped their UHPC achieve high compression strengths but the lack of fibers proved detrimental to the tension strength.

7.2 Splice-Connection Curb Strength

As mentioned in Chapter 2, both Graybeal and Qiao performed similar spliced-connection bond curbs. Table 7.3 compares the different parameters investigated between this project and Qiao. Graybeal's program tested over 200 bond curbs which will not be recreated here. See reference material for specifics (Graybeal, Bond Behavior of Reinforcing Steel in Ultra-High Performance Concrete 2014).

Table 7.3. Splice-connection bond curb testing matrix comparison between this project and Qiao.

Qiao			This Project		
c_b [inches]	L_e [inches]	f_t (7 days) [ksi]	c_b [inches]	L_e [inches]	f_t (14 days) [ksi]
1	5.00 6.25 7.50 8.75	1.12	1	4.00 4.75 5.50 6.25 7.00	1.86
2	5.00 6.25 7.50 8.75	1.12	1.75	2.25 3.00 3.75 4.50 5.25 6.00	2.19
			2.5	1.25 2.00 2.75 3.50 4.25 5.00	2.16

Graybeal's experiments utilized high-strength uncoated rebar and specimens were tested at one and seven days of curing. His results in the left plot of Figure 2.3 showed that 100 ksi bar stress, which was the fracture point of Grade 60 rebar used in this project, could be achieved with approximately a 4.75-inch embedment at one day of curing and $2d_b$ (1.25-inch) cover, and a 4-inch embedment for those specimens which cured longer or had extra cover (Graybeal, Bond Behavior of Reinforcing Steel in Ultra-High Performance Concrete 2014). Because rebar contracts radially when yielding in tension, the lugs on the bar start to disengage from the UHPC and decrease the bond capacity, so bond strength will inherently be higher for high-strength rebar

than Grade 60 rebar when both are subjected to the same stress above 60 ksi. Tension splitting was the primary failure mode, and diagonal cracks were observed that were consistent with those typically observed in non-contact splice connections in conventional concrete (see Figure 7.5) (Yuan and Graybeal 2014).

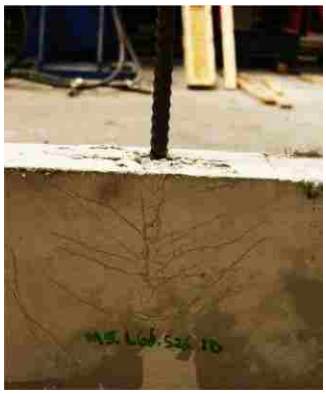

Figure 7.5. Diagonal crack pattern observed by Graybeal.

Figure 2.4 showed that with $14d_b$ (8.75-inch) embedment length, Qiao was able to achieve approximately 65 ksi bar stress with 1-inch cover and 95 ksi bar stress with 2-inch cover after seven days of curing.

In this project 100 ksi bar stress was achieved with a 4 to 5-inch splice after 14 days of curing. These lengths are comparable to those in Graybeal's experiments. Two differences separated the behavior of the splice curb specimens tested in this project from those of Graybeal and Qiao. The first was that, in those experiments, diagonal cracks parallel to the presumed compressive struts formed within the connection, but the specimens tested for this project displayed no such diagonal cracks; failure was always preceded by surface splitting, primarily of the side cover. The second was that, in the present project, additional side cover beyond 1-inch appeared to make almost no difference to the splice strength. These differences suggest that the internal load paths through the UHPC in this project's specimens differed from those observed by others. The

reasons for the different behaviors are unknown, but the matter deserves further investigation, particularly if different configurations, such as wider bar spacings with the same splice length, are planned for use in the field.

Of all the material tests, the splice-connection curbs resembled most closely the conditions in the simulated deck tests, so the data from them was analyzed to find a splice length that would guarantee failure by rebar fracture. To achieve this, two steps were necessary. First, every specimen that failed by rebar fracture or pullout was omitted, because every simulated deck specimen failed by tension splitting. Second, to eliminate the variability in UHPC strength between the three different curbs, each data point was normalized by the split-tension cylinder strength for that particular batch. The normalized data is then fit with the linear distribution produced by Equation (7) and plotted in Figure 7.6. Each curve passes through a splice length of -1 which corresponds to zero strength when the bar is not embedded in the UHPC curb at all. All bars had 1-inch clear end cover.

$$\frac{f_s}{f_t} = aL_{spl} + b \qquad \textbf{(7)}$$

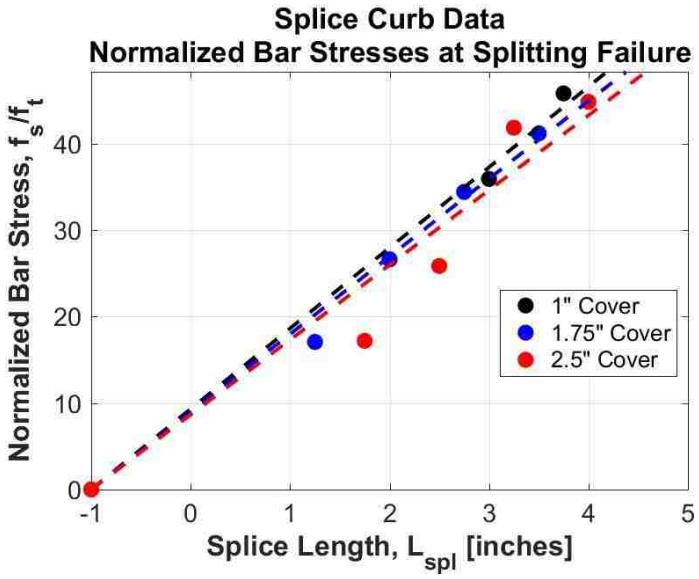

Figure 7.6. Spliced connection bond curb normalized data for only splitting failures.

The slope of each curve is proportional to the bond strength in that series of tests. Since the curves are already normalized by the material tension strength (f_t), the only remaining parameter that separates the curves is the effect of the clear cover. The normalized tension stress in the bar is given by Equation (8).

$$\left(\frac{f_s}{f_t}\right)_{avg} = a_{avg}L_{spl} + b_{avg} \cong 8.982L_{spl} + 8.982 = 8.982\left(L_{spl} + 1\right) \quad \textbf{(8)}$$

where L_{spl} is the splice length and a_{avg} and b_{avg} are linear curve-fit parameters.

The coefficient of variation of the three curves is 0.0368, which is small enough to suggest that the influence of the cover was very small. Furthermore, the fact that the thicker cover is associated with the lowest slope, and thus the lowest bond strength, suggests that the observed variations are affected more by inherent scatter than by any systematic trend. Thus, the average slope of 8.982 was used. The average bar fracture stress was 100 ksi, and the average UHPC

tension strength was 2.07 ksi, so the corresponding splice length needed to fracture the bar calculated by Equation (8) is 4.38 inches.

7.3 Simulated Deck Strength

The Simulated Deck Strength tests represent the most realistic evaluations of the flexural response of a real bridge deck. The tests conducted for this project are analyzed first, at both the service and peak load levels, and then the results are compared with those generated by others.

7.3.1 Serviceability Level Analysis

The goal here is to determine the wheel load in the real bridge that corresponds to the first departure from uncracked linear elastic behavior. This knowledge provides some estimate of the susceptibility of the joint to damage caused by truck passage.

Figure 6.10 shows the moment versus interfacial crack width relationship measured in Specimen 5 of this series. The plots for the other specimens are shown in Appendix Figure F.37 through Appendix Figure F.42. As mentioned in Section 6.4, opening of the interface crack could first be detected at a bending moment of approximately 100 kip-inches, which caused a stress of 690 psi. The corresponding crack width, defined by the resolution of the Optotrak® system, was about 0.0004 inches. When compared to the elastic FEA results (380 psi maximum tension stress), this corresponds to an axle load of approximately 58 kips (see Section 4.5), showing that the bridge deck would need to be overloaded by a factor of almost two before the interface begins to exhibit signs of cracking. Note that the crack that opens in the deck would be on the bottom face and would not be likely to allow ingress of surface water or chemicals.

If there was a pre-existing crack at the interface, it would make the joint region more flexible, so more of the bending moment would be carried at the haunched support and the joint stresses

would be smaller than the ones calculated by the FEA program. In the interests of conservatism, this reduction in bending moment is ignored in the process of determining the corresponding rebar stresses. Furthermore, the FEA showed that compressive membrane stresses are present in the region surrounding the wheel patch load. Those stresses would increase the cracking moment and reduce the real bar stress below the computed value. However, again in the interests of simplicity and conservatism, those beneficial stresses are ignored. To obtain the bar stress from the bending moment stresses, the section is analyzed as a cracked, elastic reinforced concrete member with two layers of steel. This relationship between the bar stress in the extreme layer of tension reinforcement and the applied bending moment is provided in Equation (9). The unites are inches and kips.

$$f_{s,t} = \frac{M_n}{4.568} \quad \textbf{(9)}$$

This relationship uses standard principles of elastic beam theory and assumes a 24-inch wide by 6-inch deep cross-section with two layers of #5 rebar spaced at 6 inches on-center, a steel modulus of elasticity of 29,000 ksi, and a concrete modulus of elasticity of 5,000 ksi. The steel layers were located 2.3125 inches and 4.6875 inches from the compression face.

The bending moment corresponding to 380 psi taken from the FEA assuming uncracked behavior and ignoring membrane compression is approximately 54.7 kip-in/foot. Using Equation (9), this produces an approximate bar stress of 12 ksi. This may be compared with the AASHTO limit on bar stress for a fatigue load case which is recreated in Equation (10).

$$(\Delta F)_{TH} = 24 - 0.33 f_{min} \quad \textbf{(10)}$$

where f_{min} represents the live load bar stress resulting from AASHTO's Fatigue I load combination which is the same maximum wheel load described in Section 4.2 amplified by a load factor of 1.50 (American Association of State Highway and Transportation Officials 2012). The maximum tension stress due to only the single axle load was 380 psi (see Appendix G.1). After applying the load factor and inputting into Equation (10), the fatigue threshold bar stress is 23.8 ksi, which is almost twice the computed bar stress.

7.3.2 Strength Level Analysis

The behavior of the test decks at peak load can be analyzed to determine bar stresses and evaluate performance.

All of the panels failed by splice failure rather than rebar fracture, so the results can be used to relate bar stress to splice length, and thus find the splice length needed to guarantee rebar fracture. But, this requires knowledge of the rebar stresses in the tests, and those were not available since the rebar stress could not be measured directly during the simulated deck experiments. The bending moment in the joint was known from the applied load, and the geometry of the joint was known, but the distribution of force between the two layers of rebar was not known. First, the layer closest to the compression face was ignored, on the basis that it would probably carry compression. This assumption allowed the tension stress in the primary layer to be calculated uniquely, but that stress was found to exceed by a significant margin the fracture stress of the rebar, so the assumption was rejected. Thus, an assumption was made that the force was equal in both layers of deck reinforcement. The argument to validate this assumption is that both layers of reinforcement were sufficiently yielded at deck failure such that they were both on a part of the steel stress-strain curve where the tangent modulus is low, so

moderate differences in strain imply only small differences in stress. Design code-based procedures based on Figure 7.7 were used to develop Equation (11) which relates rebar force to the bending capacity of each specimen. The calculations in Appendix G.1 were used to calculate the bending demand from the collapse load which was then substituted in for M_n in Equation (11), allowing the bar forces to be explicitly solved.

$$M_n = \left(\frac{2}{0.85 f_c' b}\right) T_{tot}^2 + d_{avg} T_{tot} \tag{11}$$

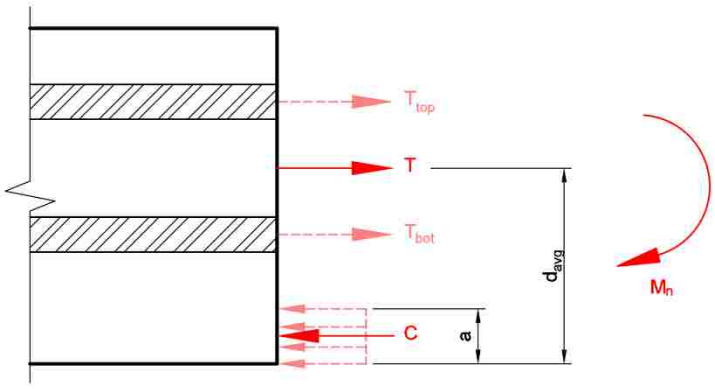

Figure 7.7. Axial forces acting on the cross-section caused by bending moment.

Table 7.4. Normalized stresses used to compare normalized peak bar stresses from the splice-connection bond curb tests and those computed from the simulated deck test bending moments.

	Specimen 1	Specimen 2	Specimen 3	Specimen 6	Specimen 7	Specimen 8
Splice Length [in]	5	1	3	4	3	4
Calculated T for Simulated Decks [kip]	30.2	12.3	20.2	24.9	25.6	25.1
Calculated f_s for Simulated Decks [ksi]	97.4	39.7	65.2	80.3	82.6	81.0
Calculated f_s/f_t for Simulated Decks	44.4	18.5	27.5	35.1	33.3	32.1

[-]						
Predicted f_s/f_t from Bond Curbs [-]	48.3	18.0	35.9	44.9	35.9	44.9
ζ	0.919	1.031	0.766	0.782	0.923	0.715
ζ_{avg}	**0.856**					

Table 7.4 outlines the bar forces and stresses which result from solving this equation, both in raw form and as normalized by their individual split-tension cylinder strengths for all simulated deck specimens except the ones with laterally offset rebar (Specimens 4 and 5) since they involved a different parameter. Also included are the bar stresses at failure predicted from the splice-connection curb data using Equation (8), and the splice lengths in the simulated deck tests.

In all cases but Specimen 2 (3" joint width and 2" splice length) the bars had yielded, because the bar stress was higher than the 65 ksi yield stress established in the bond curb tests. This finding supports the assumption that the bars in both layers experienced the same stress. If that assumption is not exactly true, the bar furthest from the compression face, which experiences the higher strain, will also experience the higher stress. That stress will be higher than the value in Table 7.4, implying better bond as well.

Comparison Between Spliced-Connection Bond Curb and Simulated Deck Analyses

The normalized peak bar stresses (f_s/f_t) from the simulated deck tests and the splice-connection bond curb tests are compared in Table 7.4. The ratio between them is given in Equation (12).

$$\zeta = \frac{\left(\frac{f_s}{f_t}\right)_{calculated}}{\left(\frac{f_s}{f_t}\right)_{curb\ prediction}} \quad \textbf{(12)}$$

Table 7.4 shows that the rebar in the simulated deck experiments had an average stress at failure of 85.6% of the rebar in the splice-connection bond curb. One possible factor which could have caused this strength difference is the casting direction. The bond curbs were cast with the rebar projecting vertically whereas the simulated deck joints were cast more realistically with the rebar projecting horizontally. Casting direction may influence the orientation of steel fibers, which have been reported by some investigators to align with the direction of flow. However, consensus is lacking and Graybeal explicitly investigated different casting directions and concluded that there was no significant effect on the UHPC's material strength (Yuan and Graybeal 2014).

A second possibility is that the assumption that the two layers of steel were equally stressed was not valid. However, if that were the case, the ζ value would be expected to be closer to 1.0 for the longer splice lengths. No such correlation exists, so the assumption is accepted as valid.

The third and most probable cause for the decreased strength is because the simulated deck tests were loaded in bending whereas the bond curbs were loaded axially. Figure 7.8 shows that, as the simulated deck bent upward, the reinforcement bent with it and imposed outward forces on the cover. This outward force would add to the splitting stress in the UHPC caused by wedging of the rebar deformations against the UHPC, which further promoted the horizontal splitting plane formation and caused splitting to occur at a lower axial bar stress.

Figure 7.8. Upward force distribution from bent reinforcement.

7.3.3 Comparison with Others

The simulated deck experiments investigated in this project were similar to those performed by Lee & Lee. While each specimen for this project had one conventional concrete panel reinforced with four epoxy-coated rebar and the other with three, Lee & Lee's conventional concrete panels were identically reinforced with five uncoated rebar which created more symmetry and allowed cracks to form at both interfaces. The typical load-deflection plot for their specimens (see Figure 2.6) showed significant ductility; the specimen reached an initial peak load and maintained that load through large deformations. This behavior was not observed during the experiments reported here. The load-deflection curves of the deck tests resembled those of the direct tension tests in which a peak load was reached, followed by a capacity that decreased gradually to a residual strength on the order of 40% of the peak strength.

As mentioned in Chapter 2, Lee & Lee observed mostly compressive failures in the 220mm (8.7-inch) thick precast concrete deck and only a few connection failures within the UHPC for the straight reinforcement configuration with joint widths ranging from 3.9 to 9.8 inches. The compressive failures were interpreted as specimens that behaved as monolithic precast members, in which the UHPC joint did not contribute significantly to the overall performance. Lee & Lee

ultimately concluded that a $7d_b$ (4.375-inch) splice length of uncoated rebar corresponding to an approximately 6-inch wide joint was sufficient to transition from a spliced connection failure mode to a compressive failure mode within the precast deck corresponding to its yield strength. The UW's simulated deck experiments all failed because of tension splitting in the UHPC and not from compressive failure in the precast concrete. The maximum 7-inch joint width (5-inch splice) very nearly developed the full rebar yield strength of the precast deck.

Finally, Lee & Lee performed lap-spliced connection tests using beams made entirely of UHPC (details in Figure 7.9) and concluded that the strength and ductility from these tests increased with fiber content, but not uniformly. The yield and ultimate strengths as well as ductility factors (calculated as the ratio between the ultimate midspan displacement and yield midspan displacement) for three fully UHPC beam experiments are replicated in Table 7.5 and plotted in Figure 7.10 (Lee and Lee 2015). These results show diminishing increases in strength and ductility for a given increase in fiber volume which suggests the 1.8% volume in the UHPC mix developed by Qiao and used here could be reduced without a significant bond strength penalty.

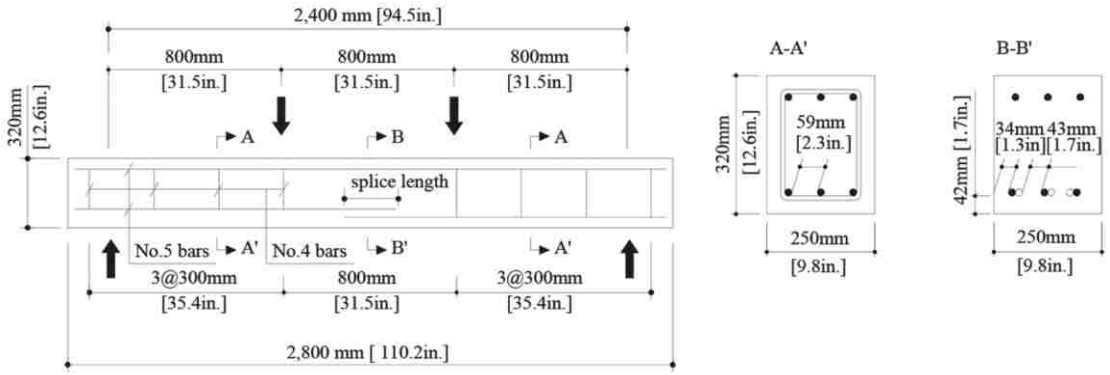

Figure 7.9. Lee & Lee lap-spliced full UHPC beam specimens.

Table 7.5. Strength and ductility as a function of steel fibers developed by Lee & Lee from their lap-spliced full UHPC beam experiments.

	1.0% Fiber Volume	1.3% Fiber Volume	1.6% Fiber Volume
Failure Mode	Lap Splice Bond	Lap Splice Bond	Rebar Yield
Yield Strength [k-ft]	165.0	188.7	212.3
% Change	-	+14.4	+12.5
Ultimate Strength [k-ft]	193.1	237.9	224.5
% Change	-	+23.2	-5.6
Ductility	2.6	3.3	3.7
% Change	-	+26.9	+12.1

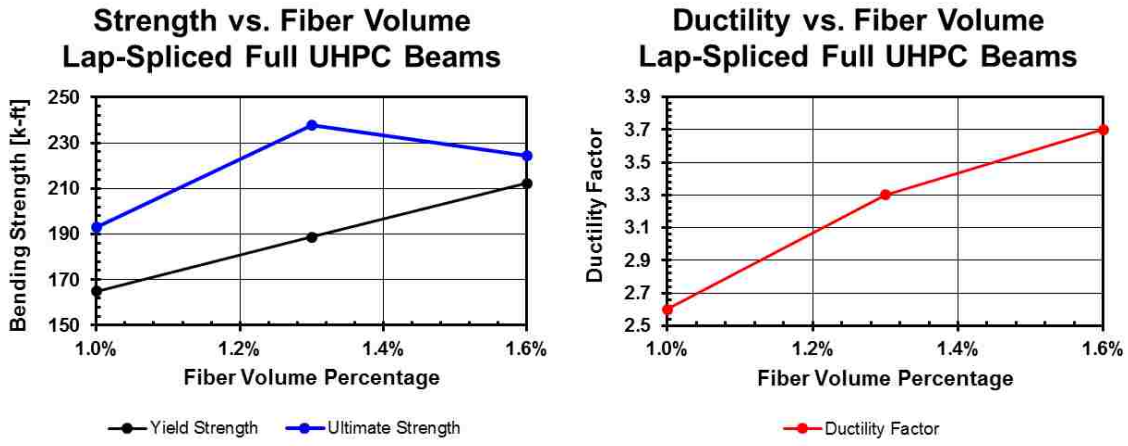

Figure 7.10. Strength and ductility as a function of steel fibers developed by Lee & Lee from their lap-spliced full UHPC beam experiments.

Chapter 8
DESIGN RECOMMENDATIONS AND DISCUSSION

In this project, the parameter of interest for designers is the joint width. Two separate design criteria were developed for determining the joint width: the Equal Strength Design Method and the Serviceability Design Method.

8.1 System Performance at Different Levels

The precast DBTs and the UHPC joint constitute a structural system, the performance of which merits review at different levels of loading demand. Because all of the testing conducted in this investigation was for bending demand under wheel loading, that is considered first.

It was shown in Appendix G.4 that the system will fail in bending under a single wheel load of 545-575 kips (depending on girder spacing) applied over the standard AASHTO contact area of 10 inches by 20 inches. However, that failure mode can never occur because the deck would fail in punching shear at a load of 90 kips, as shown in Appendix G.5. It is thus evident that the primary reason for providing the joint with the same flexural strength as the precast deck is to satisfy the AASHTO LRFD requirement that the concrete deck be "sufficiently connected to act as a unit" (AASHTO LRFD Section 4.6) in order to benefit from the highest level of wheel load distribution (American Association of State Highway and Transportation Officials 2012). Well-distributed wheel loads reduce the loading on any one girder and may allow the use of fewer girder lines at wider spacing.

This objective is somewhat irrational because wheel load distribution depends on the relative stiffness of the various components of the superstructure, but the criterion for deciding whether the full distribution factors can be used is widely interpreted as being a strength criterion. Nonetheless, that criterion will lead to a lower bound on the required joint width. This approach is referred to herein as the "Equal Strength Requirement", indicating equal strength in the joint and deck panels, and is discussed in Section 8.2.

The joint should also be expected to perform satisfactorily under service loads. Again, bending under wheel loading is the most important action. Satisfactory performance is difficult to define in a system containing cold joints such as the one between the precast concrete and the UHPC. In a deck cast in one continuous pour, a no-cracking criterion might be deemed appropriate, but that is hard to apply here because of the difficulties of detecting first cracking at the interface in the test, and of ensuring adequate bond between the two materials in the field.

Thus, some other criterion must be chosen. Here, tensile bar stress caused by wheel load is used, supplemented by the need to achieve a low crack width at the interface, as judged from the test results. This approach implicitly accepts that a crack will form on the bottom surface at the interface and that the region will behave as a cracked elastic section. The goal of limiting the bar stress is to avoid fatigue failure of the bars. The purpose of requiring fine cracks is to inhibit ingress of moisture and chemicals. This approach is referred to here as the "Serviceability Requirement", and is discussed in Section 8.3.

Shear capacity, both within the UHPC and at the interface between the two materials was not addressed in the test program. However, it is possible to calculate the shear induced at the interface by correcting a given camber differential between adjacent girders. This calculation is performed in Appendix G.5.

8.2 Equal Strength Design Method

The Equal Strength Design Method is intended to produce a joint that is at least as strong as the conventional concrete deck elements that it connects. This is important for two reasons:

- The undesirability of creating a potentially weak spot in the structure that is also a connection location, and thus susceptible to potential further weakness caused by construction errors.
- The requirement that the concrete deck must be "sufficiently connected to act as a unit" to benefit from the highest level of wheel load distribution (American Association of State Highway and Transportation Officials 2012). Well-distributed wheel loads reduce the loading on any one girder and may allow the use of fewer girders at wider spacing.

The primary need is for the capacity of the splice in the UHPC joint to be greater than the fracture capacity of the rebar. It could be argued that the deck should be "sufficiently connected to act as a unit" if the bars were to reach yield, rather than fracture, before failing in bond. However, the more conservative interpretation is used here to avoid dispute. Other characteristics, such as the true bending strength within the UHPC joint, will almost certainly exceed that of the precast deck elements because the reinforcement is identical and the compressive strength of the UHPC is likely to exceed that of the concrete. For that reason, they are not investigated further here.

The characteristics that may affect splice strength are the material properties, the splice length, and the clear cover. The material to be used is assumed to be the one used in this study (mix C3 from Qiao) (Qiao, Zhou and Allena 2017). The cover was shown in Section 7.2 to have negligible influence on the splice strength within the range of cover thicknesses tested here (1.00

– 2.50 inches). This allows the use of 1-inch cover with no strength penalty. That choice is convenient for construction because it is also the bottom cover typically used in the precast deck elements, so it allows for the simplest joint formwork, consisting only of plywood attached to the soffit of the two deck elements. Thus, the width of the joint is the critical characteristic remaining to be chosen.

The simplest approach would be to identify and use the smallest joint width that led to rebar fracture rather than splice failure in the panel tests, but this is not possible because all panel tests suffered splice failure. However, the methods shown in Section 7.3.2 show that, in the widest joint (7 inches), the bars were stressed to 97.4 ksi, which is very close to the fracture stress. This suggests that the necessary joint width is only slightly larger than 7 inches.

To determine the necessary width, the splice-connection bond curb data can be used. It was shown in Section 7.3.2 that the simulated deck specimens had a connection strength that was an average of 85.6% of that of the spliced-connection bond curbs with the same cover and embedment length. The procedure adopted here is to find the splice length to satisfy the Equal Strength criterion for the splice-connection bond curb specimens and increase it by a factor of $1/\zeta_{avg} \cong 1.16$ to give the necessary joint width in the simulated deck specimen. This splice length was determined in Section 7.2 to be 4.38 inches which becomes 5.11 inches when amplified by 1.16. This length assumes the girders are fabricated perfectly with the exact rebar projection lengths. If the rebar projection is 1-inch too short, or the girder sweep is 1-inch in an unfavorable direction, the splice will be shortened by 1 inch, so an additional inch of splice is needed to ensure the splice is adequate. If the effect of lateral rebar offset is considered in the most severe case where the connection becomes lap-spliced, an additional 16% is needed to

compensate for the reduced strength. This ultimately causes a required joint width of approximately 9.09 inches, which is rounded up here to 10 inches.

8.3 Serviceability Design Method

The Serviceability Design Method is intended to ensure that the rebar stresses when subjected to wheel loading are low enough to avoid fatigue failure in the rebar and excessive opening of the interfacial crack.

To find the embedment length needed to sustain the bar stress calculated in Section 7.3.1, a service load allowable bond stress is needed. It is taken here as 50% of the pullout bond stress at failure in the splice-connection bond curb experiments. The allowable bond stress in each of the splice-connection bond curb experiments is calculated by Equation (13).

$$\tau_{ba} = \alpha f_t \left(\frac{T/f_t}{\beta \pi d_b L_e} \right) \quad \textbf{(13)}$$

where β is 1.0 and 0.5 for uniform and triangular bond stress distributions, respectively, and α represents the fraction of the ultimate bond strength which is used as the allowable bond stress which will be taken here as 0.5.

By invoking bar stress equilibrium and inputting Equation (8), the required embedment length calculated by Equation (14) is 1.30 inches. Applying any safety factors will still result in a joint width which is considerably narrower than that which was calculated by the Equal Strength design method. Thus, the serviceability criterion is always satisfied if the joint is designed per the Equal Strength criterion.

$$L_e = \frac{A_b f_{sa}}{2.773 \alpha f_t} \quad \textbf{(14)}$$

As mentioned in Section 7.3.1, there is an approximate factor of safety of two against the interface cracking an amount which is noticeable on the load-deflection plots as illustrated in Figure 6.10. The actual crack width for the serviceability criterion (bending moment of 54.7 kip-inches which causes the 12 ksi bar stress) was approximately 0.00037 inches (read from Figure 6.10). This crack width may be compared to limiting values. Suitable standards of comparison include:

- Optotrak® camera resolution (0.000394 inches).
- Maximum crack width permitted by ACI for exposure to humid air (0.012 inches), deicing salts (0.007 inches), and for liquid-retaining structures (0.004 inches) (ACI Committee 224 2001).

This measured crack width is far below the ACI-specified allowable crack widths and is on the order of the Optotrak's® resolution capability. Thus, if the joint is designed based on the Equal Strength criterion, it will easily satisfy all serviceability criteria.

8.4 Implementation Considerations

Several issues associated with implementation arose during the research. Many were brought up in discussions with the Association of General Contractors (AGC) during a meeting held on March 10, 2017. Detailed notes from that meeting are provided in Appendix B (Contractors 2017). The main issues are summarized here.

Contracting Arrangements

Most UHPC joints in bridges in the United States have been achieved with Lafarge's Ductal® UHPC. This is reported to cost approximately $3,000/yd^3 but company representatives typically

are on-site to ensure that problems do not arise, and they implicitly absorb any risk (Graybeal 2016). The cost of the materials for the mix used in this research is approximately $1,500/yd^3 (see Section 5.1), but contractors believed that the potential savings did not adequately compensate for the risk of working with a new and relatively unknown material. The consequences of mistakes, such as the extreme difficulty of jack-hammering hardened UHPC, played a part in this evaluation. The Buy-America clause plays no part, because all the materials for the mix used here are available domestically.

The picture could change if WSDOT were prepared to carry some of that risk in the short term, for example, by specifying a mix design. In the longer term, when contractors have become more familiar with the material, the use of a performance specification might be a beneficial approach. It is now being used successfully in many states for conventional concretes, because the approach allows the contractor to price the risk and profit from their expertise (Ferluga and Glassford 2015). That approach would require materials acceptance tests, and defining them requires planning because many of the common ASTM-standard tests measure properties that are not critical (e.g., compression strength), or are not well suited to fiber-reinforced materials such as UHPC (e.g., split cylinder tension, flexural beam tests.) For important properties, such as bond, ASTM A944 addresses bond strength, but may need to be analyzed for its appropriateness with fiber-reinforced concrete (ASTM International 2010).

Speed of Construction

One of the goals of using DBTs is to shorten on-site construction time by eliminating the deck-casting operation. The speed at which the UHPC gains strength must therefore be considered. WSDOT plans to use an overlay or wearing course on its DBT bridges, and, because this operation takes a few days, the UHPC is expected to have a week or more to gain strength before

the joint needs to carry truck loads. In that time, sufficient strength can be easily achieved. If the bridge is on a slope, top forms may be needed for the UHPC joint, in which case the surface may not be completely flush with the deck, and grinding may be necessary. However, this could (and should) be undertaken within a day or so of pouring, lest the UHPC gain too much strength and make grinding more arduous. Grinding is therefore unlikely to impact overall schedule. Equipment needed to correct differential camber (e.g., strongbacks and jacks) would have to remain in place until the UHPC was strong enough to resist the shear forces. However, the calculated interfacial shear demands (see Appendix G.6) concerning differential camber correction were on the order of less than 10 psi, which could easily be achieved in a day or two. The strongbacks could then be removed to make way for pouring the overlay.

Skew Bridges and Bar Conflicts

In a skew bridge, attention must be paid to the orientation of the transverse bars in the deck elements. In cast-in-place decks, they are usually oriented parallel to the end supports, and gradually splayed so they are oriented perpendicular to the longitudinal steel in the majority of the span. Splayed bars might create difficulties for the precast fabricator, and any bar placement errors would risk bar conflicts on site. The problem is one of detailing, and is soluble, but lies outside the scope of this project.

Stability and Shipping Weight

DBTs are inherently heavier than their I-section counterparts and may pose potential trucking weight problems, particularly when site access and crane capacity are taken into account. Thus, weight may limit the spans that can be achieved. The AGC participants saw no serious overall problem, but emphasized that the matter should be evaluated on a case-by-case basis. The

center of gravity of a DBT is also higher than that of a comparable I-girder and will affect stability. That fact needs to be considered in plans for shipping and handling.

Chapter 9
SUMMARY, CONCLUSIONS, AND RECOMMENDATIONS

9.1 Summary

Goals

This project aimed to determine the mechanical properties (tension strength, compression strength, ductility, etc.) of a non-proprietary UHPC mix and create design recommendations for its use as a longitudinal joint in DBT girder bridges.

Demand Analysis

A preliminary series of FEAs were performed using realistic geometry and design-level live loads as specified by the AASHTO LRFD Specification. The results of these analyses provided estimates the demand on the bridge decks which were then used to design the physical experiments. These results showed that the bridge deck is relatively lightly stressed under design-level loads which created the necessity for simplified physical experiments which intensified the stresses at the longitudinal joint.

Mixing Procedures

The first step in the experimental program was to optimize the mixing procedure to best suit the available equipment since mix quality is especially important for fiber-reinforced concrete. In drum mixers, motion of the coarse aggregate achieves most of the mixing of the other materials.

Because this UHPC contained no coarse aggregate, a pan mixer was used for the purpose, in which the paddles mixed the materials by scraping and folding them together.

Material Strength Experiments

A combination of standard and custom material strength tests was then performed to determine the UHPC's tension and compression strength.

Bond Curb Experiments

Bond curb specimens were then tested to determine the bond performance in a realistic configuration. These experiments varied parameters such as embedment length and clear cover to determine bond strength relationships when the UHPC is used for a non-contact spliced connection.

Simulated Deck Experiments

The final series of physical experiments were conducted on deck panels, which simulated the connection of two adjacent DBT girders connected by a UHPC joint. These experiments had objectives similar to those of the bond curbs, but were as realistic as possible; that is, the panels were subjected to a single load on the joint which caused bending similar to that experienced by the joint between DBTs under traffic loading.

Analysis of Results and Recommendations

The results of each series of experiments were then analyzed to compare with other organizations which developed similar UHPCs and ultimately develop design recommendations for the joint design considering both strength and serviceability limit states.

9.2 Conclusions

The following conclusions were drawn from the study:

Suitability of UHPC Joints

UHPC in general, and the mix developed in this research in particular, is capable of producing bond to reinforcing bars that has both high strength and high ductility, making it a suitable choice for use in longitudinal bridge joints connected by a non-contact splice.

Mix Properties

The non-proprietary mix design developed by Qiao and tested in this study showed mechanical properties that closely rival those of the proprietary Ductal® mix, but at a significantly lower cost. Strength gain with time experiments revealed that this UHPC gains its strength relatively quickly, with at least 50% of its 14-day strength achieved after two days of curing. Discussions with contractors revealed that this speed is fast enough for practical purposes.

Bond Strength

The high bond strength between UHPC and epoxy-coated #5 rebar was attributed to the presence of steel fibers. Karmout's research using UHPC with no fiber reinforcement showed comparable compressive strength but lacked tension strength. He conducted no bond tests. Almost all the tests conducted for this research program failed by tension splitting because the pullout bond strength was high (allowing a large force to be transferred over a short distance) and the side cover was not excessive. Significant strength remained even after the splits initiated, so the bond behavior was ductile.

Effect of Clear Cover

Increases in clear cover in the range of 1 inch to 2.5 inches did not have a significant influence

on bond strength. This finding conflicts with that of others, both for conventional concrete and UHPC. In the case of UHPC, it may be explained by the fact that some of Graybeal's experiments were performed using high-strength, uncoated rebar stressed to approximately 160 ksi. It is possible that the benefits of larger cover are realized only for rebar with yield strengths higher than 60 ksi, and that is why they were not seen here.

Location of Cracks within the Joint

The simulated deck experiments showed essentially no cracking in the body of the UHPC joint and significant cracking at the cold joint interface between the UHPC and conventional concrete. Note that the joint faces received no special preparation before casting the UHPC. At this interface, the crack began to open at a load equivalent to approximately two times the design-level load in a real bridge. Note that this cracking will exist on the underside of the driving deck which means that ingress of moisture and chemicals is improbable and will not affect the bridge deck's performance.

Interface Shear Transfer

The vertical shear demand and capacity at the joint interface was not investigated experimentally, but a simple calculation shows that, for every inch of differential camber that needs to be adjusted to align the driving surface, the shear stress is on the order of less than 5% of just the cohesive component of the shear friction strength specified in Section 5.8.4.3 in the AASHTO LRFD Specification for roughened surfaces. If much higher shear demands were expected (for example from permit load trucks) the shear friction capacity would be further increased by the clamping force generated by the #5 rebar crossing the crack and by the membrane compression stresses present in the deck which were on the order of approximately 10-75 psi as shown by the FEA.

Failure Hierarchy and Design Criteria

Simple analyses showed that deck failure due to wheel loads will be controlled by punching shear and not by bending of the deck and yielding of the reinforcement. Thus, the joint will never be subjected to bending moments large enough to fracture the bars. Nonetheless, the joint should be designed using the Equal Strength criterion, which requires that it fail by rebar fracture rather than splice failure. Doing so ensures that the deck behaves as a single unit and so permits use of the highest level of wheel load distribution allowed by the AASHTO LRFD Specification. Service load performance criteria were found to be easily satisfied if the joint was designed according to the Equal Strength criterion. That would anyway be true for a prismatic deck, but it is all the more true in the DBT system because the positive bending demand on the joint is reduced by the existence of the haunches in the deck profile which attract bending moments from the joint at midspan toward to the supports at the girder web.

Joint Width

The simulated deck experiments most closely resembled the behavior of the deck in the real bridge and revealed that a joint width greater than 7.11 inches (splice length of 5.11 inches) will fracture the rebar at the face of the UHPC joint. Use of a narrower joint will amplify the effect of construction tolerances such as girder sweep, differential camber, and rebar projection length and the marginal economies associated with decreasing the joint width are insignificant compared with the total project cost. Including construction tolerance factors conservatively increases this joint width to 10 inches.

Contractual Risk and Responsibility

General contractors showed a reluctance to adopt a non-proprietary material for use in their projects because of the perceived high risk. These contractors believed that the risk of

developing and working with their own UHPC mix was far greater than the cost savings associated with using a non-proprietary mix. WSDOT will need to address this perception of risk if a non-proprietary mix is to be used. Specifying a mix design and therefore carrying some of the risk is a possible short-term approach. In the longer term, the use of a performance specification, accompanied by acceptance tests and criteria, might be preferable.

9.3 Recommendations

9.3.1 Recommendations for Implementation

The following guidelines are recommended for implementing UHPC for this construction method.

UHPC Mix

Throughout this project, it appeared that mix quality was an important parameter that should be considered carefully. This project used the same mix design as Qiao and achieved similar material strengths when comparing ASTM-standard tests, but Qiao used a conventional drum mixer whereas this project used a pan mixer. Pan mixers are better suited for pasty concretes, especially when coarse aggregate is lacking. While it is difficult to argue, the difference in mix quality provided by these two mixers could have been the reason for the significant difference in bond strength observed when comparing the splice-connection bond curb results.

Furthermore, since this mix has a low water-cement ratio, it is important to ensure all dry materials are adequately incorporated into the mix to prevent the formation of dry pockets in the final product.

Ultimately, the C3 mix specified by Qiao should be used and the incentives and risks associated with using this mix should be addressed by contractors on a project-by-project basis.

Structural Design

Following the final recommendation from Chapter 8, the Equal Strength design method satisfies all serviceability and ultimate strength criteria, and thus should be used to design the joint. This will not create any further impact on the structural design.

The system investigated here may be used for connecting DBTs in the field. For 6-inch thick decks reinforced with #5 epoxy-coated rebar in the top and bottom layers, a 10-inch wide joint will provide satisfactory performance at all load levels.

Construction Quality Control

For this application, the UHPC's tension and bond strengths are of utmost importance. ASTM-standard material strength tests have shown to be the most attractive option for contractors as opposed to custom tests. Accordingly, the split-tension cylinder test shall be used as the primary indicator of the UHPC's splitting tension strength as it is most directly related to the type of splitting failure observed within the connection during experiments.

Per the contractor's discretion, it may be useful to use a mock joint to perform a practice run with the UHPC to become comfortable with mixing and pouring the concrete before the real joint is poured. This UHPC is flowable, which should be a good indicator of mixing quality and thoroughness, and it should easily fill any corners without additional aid, such as vibration.

Joint Construction

When constructing the UHPC joint, the faces of the deck which will form the joint shall be roughened per AASHTO specifications. A formed shear key shall not be used because of the stress concentration that forms at the corner of the key and causes premature tension failure. The

interfacial shear demand due to differential camber corrections are well within allowable limits even without the roughened surface.

The UHPC joint shall not be overfilled and then ground flush with the deck, especially when an asphalt overlay is to be constructed. However, if grinding is deemed necessary, it shall be performed as soon after pouring as possible.

Each joint shall be filled in one continuous operation to prevent unfavorable steel fiber alignment between successive pours. The joint shall not be constructed by filling the length of the joint with a shallow layer of UHPC and incrementally adding layers atop the previous one. The pour sequence shall completely fill the joint through the thickness as construction moves down the length of the joint.

9.3.2 Recommendations for Further Research

Steel Fiber Quantity

The cost analysis of this particular UHPC revealed that the steel fibers were the single most expensive material in the mix, constituting almost 40% of the total cost. Cost reductions could be achieved by investigating the effect of decreasing the volume fraction of steel fibers. Alternative mixes with lower fiber contents should be investigated with the goal of relating bond and tension strength to fiber volume fraction.

Shear Demand and Capacity

Both the computer and physical experiments performed by this project only focused on the bending strength of the bridge deck and UHPC joint. The shear demand caused by traffic loading as well as the shear capacity of the UHPC material and interface between the UHPC and

conventional concrete deck should be investigated, especially if considering formed keys or prepared surfaces within the joint.

Reinforcement Configuration

This project only focused on epoxy-coated #5 rebar spaced at six inches on-center throughout the bridge deck. Since the Equal Strength design method satisfies all strength and serviceability criteria, if a bridge is to be designed using different reinforcement configurations (i.e.: different bar sizes, bar spacings, bar coatings, etc.), then the relationship between these parameters and the non-contact splice connection strength needs to be investigated to determine what joint width is appropriate.

REFERENCES

ACI Committee 209. 2008. *ACI 209.2R-08 "Guide for Modeling and Calculating Shrinkage and Creep in Hardened Concrete".*

ACI Committee 224. 2001. *ACI 224R-01 "Control of Cracking in Concrete Structures".* American Concrete Institute.

American Association of State Highway and Transportation Officials. 2012. *AASHTO LRFD Bridge Design Specifications.*

ASTM International. 2010. "ASTM A944-10 "Standard Test Method for Comparing Bond Strength of Steel Reinforcing Bars to Concrete Using Beam-End Specimens"."

—. 2016. *ASTM C109 / C109M - 16a "Standard Test Method for Compressive Strength of Hydraulic Cement Mortars (Using 2-in. or [50-mm] Cube Specimens)".*

—. 2014. *ASTM C1611 / C1611M - 14 "Standard Test Method for Slump Flow of Self-Consolidating Concrete".*

—. 2016. *ASTM C192 / C192M - 16a "Standard Practice for Making and Curing Concrete Test Specimens in the Laboratory".*

—. 2017. *ASTM C39 / C39M - 17 "Standard Test Method for Compressive Strength of Cylindrical Concrete Specimens".*

—. 2014. *ASTM C469 / C469M - 14 "Standard Test Method for Static Modulus of Elasticity and Poisson's Ratio of Concrete in Compression"*.

—. 2011. *ASTM C496 / C496M - 11 "Standard Test Method for Splitting Tensile Strength of Cylindrical Concrete Specimens"*.

—. 2016. *ASTM C78 / C78M - 16 "Standard Test Method for Flexural Strength of Concrete (Using Simple Beam with Third-Point Loading"*.

—. 2015. *ASTM C900 - 15 "Standard Test Method for Pullout Strength of Hardened Concrete"*.

Concrete Technology Corporation. 1995. "65" Decked Bulb Tee." *Concrete Technology Corporation.*

Contractors, Association of General, interview by University of Washington. 2017. (March 10).

Ferluga, Eric, and Patrick Glassford. 2015. "Evaluation of Performance Based Concrete for Bridge Decks." Washington State Department of Transportation.

Graybeal, Benjamin, interview by John Stanton. 2016. (November 12).

Graybeal, Benjamin. 2014. "Bond Behavior of Reinforcing Steel in Ultra-High Performance Concrete." Research, Development, and Technology, Federal Highway Administration.

Graybeal, Benjamin. 2014. "Design and Construction of Field-Cast UHPC Connections." Research, Development, and Technology, Federal Highway Administration.

Graybeal, Benjamin, and Florent Baby. 2013. *Development of Direct Tension Test Method for Ultra-High-Performance Fiber-Reinforced Concrete.* ACI Materials Journal.

Hong, Sungnam, and Sun-Kyu Park. 2011. "Uniaxial Bond Stress-Slip Relationship of Reinforcing Bars in Concrete." Department of Civil and Environmental Engineering, Sungkyunkwan University.

Karmout, Mahmoud, Mohammed Arafa, and Samir Shihada. 2009. "Mechanical Properties of Ultra High Performance Concrete Produced in Gaza Strip." Civil Engineering Department, The Islamic University of Gaza.

Lee, Jun Ki, and Seung Hoon Lee. 2015. "Flexural Behavior of Ultra-High-Performance Fiber-Reinforced Concrete Moment Connection for Precast Concrete Decks." *ACI Structural Journal.*

Portland Cement Association. n.d. *Cement & Concrete Basics - Aggregates.* http://www.cement.org.

Qiao, Pizhong, Zhidong Zhou, and Srinivas Allena. 2017. "Developing Connections for Longitudinal Joints Between Deck Bulb Tees - Development of UHPC Mixes with Local Materials." Department of Civil and Environmental Engineering, Washington State University.

Silica Fume Association. n.d. *What is Silica Fume?* http://www.silicafume.org.

Thomas, Jeff, and Hamlin Jennings. n.d. *The Science of Concrete.* http://iti.northwestern.edu.

Washington State Department of Transportation. 2016. *Bridge Design Manual (LRFD).*

Wight, James K, and James G. MacGregor. 2012. *Reinforced Concrete Mechanics & Design.* Upper Saddle River, New Jersey: Pearson Education, Inc.

Yuan, Jiqiu, and Benjamin Graybeal. 2014. "Bond Behavior of Reinforcing Steel in Ultra-High Performance Concrete."

Appendix A
STRUCTURAL BEHAVIOR AND MECHANICS

A.1 Ultra-High Performance Concrete

When observed at the microstructure level, all concretes perform as a function of the percentage of voids present in the mix's matrix. Conventional concrete typically mixes three primary ingredients together with water to form a strong, hardened paste. These include cement, fine aggregate (i.e.: sand), and coarse aggregate (i.e.: gravel or crushed rock). When these materials are combined in a mix their packing density is controlled by the particle size distribution. Appendix Table A.1 lists the approximate particle sizes of each component used in conventional concrete (Thomas and Jennings n.d.) (Portland Cement Association n.d.).

Appendix Table A.1. Typical particle size distribution for conventional concrete materials.

Cement	Fine Aggregate	Coarse Aggregate
1 μm – 100 μm	< 0.375 in	0.375 – 1.5 in

When these materials are mixed and packed together as shown in Appendix Figure A.2, the gap-graded particle sizes create voids. As concrete is stressed in compression these voids function as stress concentrations where microcracks begin to form due to the accompanying shear stresses on inclined surfaces created by the coarse aggregates in addition to tension stresses from Poisson expansion. When the stress approaches the material's capacity these microcracks propagate throughout the structure until they connect to form a failure plane (Appendix Figure A.1).

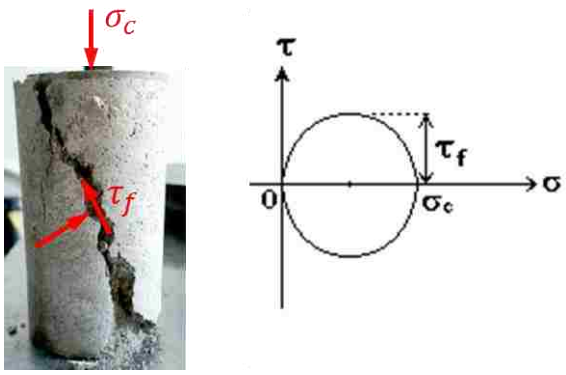

Appendix Figure A.1. State of stress on the inclined failure plane of a compression specimen.

A larger volumetric percentage of voids in the paste (caused by gap-graded materials or a high water content) creates more locations for microcracks to form which results in fast crack propagation and a weaker, brittle structure. The overarching goal of UHPC is to gain extra strength and ductility by reducing the void volume to inhibit rapid microcrack propagation. This is typically achieved by removing components with a large particle size (i.e.: coarse aggregate), adding cementitious materials with a very small particle size (i.e.: silica fume, which is on the order of 1/100th the size of cement) to fill in the voids, and stitching together the microstructure with steel fibers, as illustrated by Appendix Figure A.2 (Silica Fume Association n.d.).

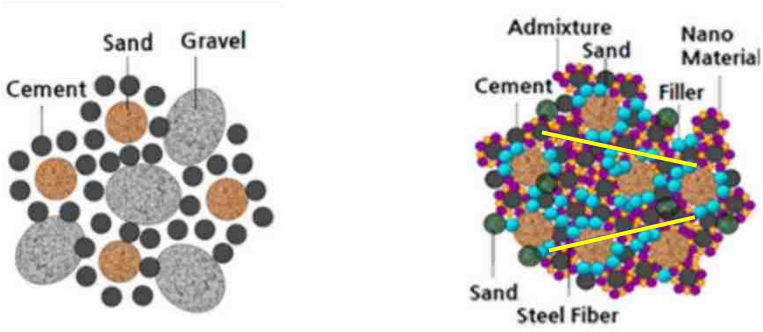

Appendix Figure A.2. Microstructure composition of conventional concrete (left) and UHPC (right).

A microstructure which has changed in this manner creates a concrete which is more resistant to microcracks forming and widening. The denser packing of particles reduces the volume of voids and the steel fibers bridge any microcracks which do form and use their tensile strength to resist those cracks from widening and propagating. This ultimately creates a stronger concrete with impressive ductility, as depicted in Appendix Figure A.3.

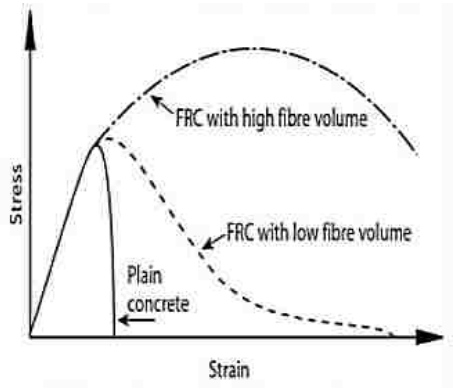

Appendix Figure A.3. Compressive stress-strain behavior comparison between conventional concrete and fiber-reinforced concrete.

A.2 Reinforced Concrete Bond

The bond strength of epoxy-coated rebar in UHPC is of primary interest for understanding the behavior of a non-contact spliced connection. Both layers of reinforcement in the deck of a DBT girder will be spliced with adjacent reinforcement and the bottom layer will be subjected to the highest tensile stresses caused by positive bending moments from traffic loading. Tension-loaded rebar relies on local bond stresses around its perimeter as well as bearing forces on the bar deformations to anchor itself in the concrete and achieve the design yield stress of the bar at minimum. Appendix Figure A.4 depicts the variation in bond stress along the length of the bonded reinforcement as a function of the amount of slip between the rebar and the concrete (Hong and Park 2011).

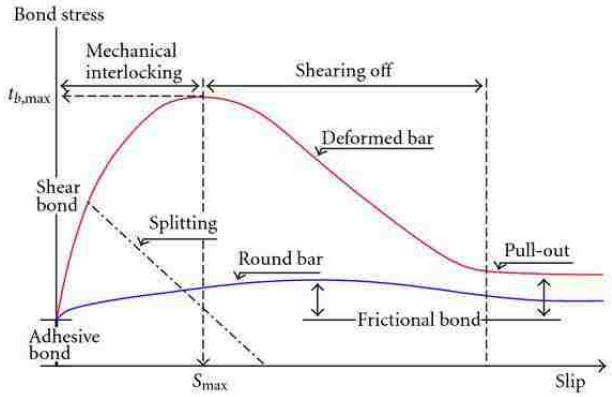

Appendix Figure A.4. Bond stress variation with respect to slip.

The adhesive bond limit in this figure is due to the small amount of chemical adhesion between the concrete and smooth region of a rebar which prevents any shear slipping. Once this adhesive capacity is exceeded, rebar gains the majority of its capacity from the mechanical interlocking caused by the deformations bearing on the concrete. After enough slip has occurred to diminish the contribution of the deformations, the ultimate bond capacity is exceeded and the rebar is smoothly pulled through the concrete and the bond strength steadily diminishes. If the rebar is

able to sustain significant slip relative to its bonded length and if the tensile capacity of the concrete exceeds the pullout bond strength, the bond stress eventually becomes uniform and the failure mechanism is rebar pullout. A pullout failure mechanism will typically occur when the clear cover and/or reinforcement spacing are relatively large whereby the rebar is surrounded by enough concrete to provide sufficient tensile capacity.

If the tensile capacity of the concrete is exceeded at any point along the "Deformed bar" curve in Appendix Figure A.4, then the concrete will either split through the concrete cover or form a breakout cone and the bond resistance will sharply decrease. The tension force which the concrete must resist originates from any bearing surface on the embedment. Traditional rebar generates these bearing forces from the bar deformations and concrete anchors generate them from the anchor heads, both of which exert the radial forces shown in Appendix Figure A.5 on the concrete when the embedment is stressed in tension.

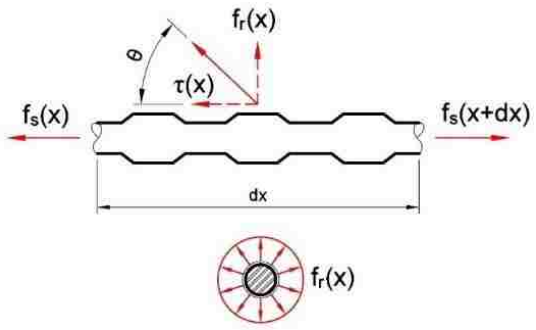

Appendix Figure A.5. Forces from a tension-loaded rebar showing the radial component created by the bar deformations.

Appendix Figure A.6 shows that a splitting failure will typically occur for any embedment length when the clear cover dimension is small such that it provides insufficient tensile capacity or when the reinforcement is closely spaced such that the radial forces from adjacent rebar compounds and creates tensile stresses which exceed the concrete's capacity. A breakout failure

will typically occur when the embedment length is insufficient to allow the radial forces to adequately spread out and be safely resisted by the concrete.

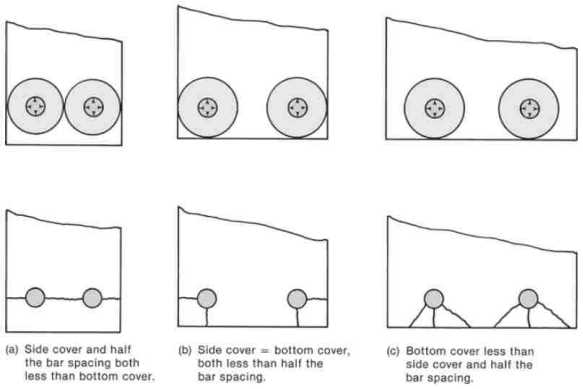

Appendix Figure A.6. Typical splitting planes formed at tension and bond failure.

All bond failure mechanisms are depicted in Appendix Figure A.7.

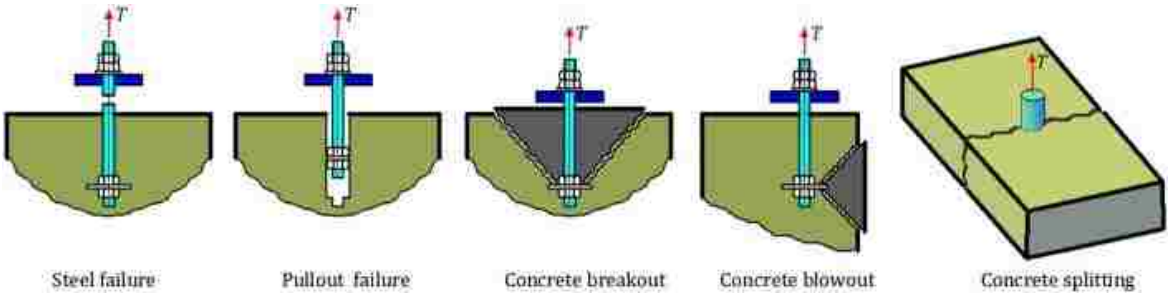

Appendix Figure A.7. Rebar bond failure mechanisms.

A.3 Non-Contact Spliced Connection

As previously mentioned, the proposed construction method creates a non-contact spliced connection. Appendix Figure A.8 shows the connection's force transfer mechanism where the radial forces exerted on the concrete by adjacent tension-loaded reinforcement create uniaxial compression struts in the concrete (Wight and MacGregor 2012).

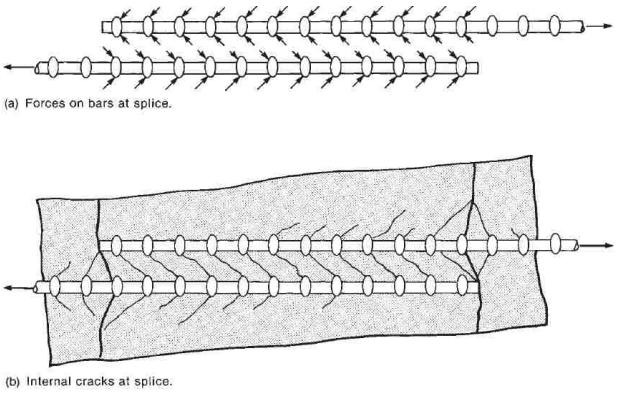

Appendix Figure A.8. Force transfer mechanism for a non-contact spliced connection.

Appendix Figure A.1 showed how shear and tension stresses develop when concrete is uniaxially compressed and form cracks. In a non-contact splice connection, these cracks follow the diagonal orientation of the struts until a failure plane forms between the adjacent reinforcement in a plane connecting the two rebar.

The design for a non-contact spliced connection should include embedding the rebar a sufficient length to allow for a distribution of bond stresses which sufficiently spreads the radial tension stresses such that they do not exceed the concrete's tension strength.

Appendix B
IMPLEMENTATION NOTES FROM MEETING WITH THE ASSOCIATION OF GENERAL CONTRACTORS

The following are common questions asked to the Association of General Contractors and their responses concerning current practices and opinions involving the use of UHPC for this type of construction.

Q: How crucial is the joint width to construction activities? Should conventional concrete be used with a wider joint instead?

A: If an asphalt overlay is required to finish the driving surface, pouring the UHPC and waiting for it to gain sufficient strength is not on the critical path for the construction timeline. The cost of UHPC as a material itself is more significant than the labor, mixers, formwork, etc., so the joint width should be forced as narrow as possible to decrease material costs. A wider joint made of conventional concrete should not be used because it would completely defeat the purpose of this type of construction method.

Q: What are the stability concerns with using DBT girders?

A: Lateral stability on the interior span of the girders should be addressed during the structural design phase. The girders are sufficiently braced at their ends by the pier caps. Upward

buckling instabilities while lifting the girders are the more common and severe issue due to the amount of prestressing, especially for long spans. The transverse girder spacing should be kept as short as reasonable to reduce this risk.

Q: What are the limits on shipping weight?

A: The absolute maximum weight limit is typically 270,000 lbs. The real weight consideration should be based on the capacity of on-site cranes. Depending on the type of site, large cranes may not be able to access the site, especially since this type of construction is being proposed for sites which are difficult to access. Overall, it is difficult to generalize and weight limits should be evaluated on a site-by-site basis.

Q: How is differential camber corrected to prepare for pouring the UHPC?

A: Common practice is to use strongbacks to push the girders vertically into place and correct the differential camber between girders. These strongbacks are not a critical item for scheduling, so they can stay in place as long as necessary for the UHPC to achieve sufficient strength.

Q: Will the exposed deck reinforcement pose a conflict issue with adjacent girders when lined up to pour the joint?

A: Uniform rebar spacing could clash with adjacent rebar, especially with skewed girders. For standard girders, this should not be problematic and any individual conflict can easily be correct by bending the rebar. From a strength perspective, a lateral rebar offset should be addressed

during design. For bridge widening projects looking to use this type of construction, there may be an issue when demolishing the existing barrier. This can be mitigated by adjusting the new construction rebar to avoid the known locations of existing rebar.

Q: How is the top surface of the joint prepared after pouring?

A: A top form will be necessary due to the fluidity of the UHPC and the slope of the deck. The joint will typically be overfilled to allow for settling while curing and then ground flush with the top of the deck. Grinding UHPC can be quite difficult, especially if done by hand. If an overlay is used on the deck, grinding is not necessary unless a membrane is used. If grinding is required, it needs to be done as early as possible before the UHPC has gained too much strength.

Q: What should be included in a performance specification for UHPC?

A: Before components of a performance specification are addressed, it should be decided on a project-by-project basis whether the general contractor shall mix their own UHPC. Due to the infancy of this material and the associated construction methods, the consensus is that the risk is currently too great for the general contractor to mix the UHPC and all mixing activities should be monitored by the UHPC manufacturer. The overall cost of UHPC may not be a significant percentage of the total project cost to warrant the general contractor to save the money to perform all mixing operations themselves.

Q: How will pouring mistakes be corrected?

A: If there is a bad pour, it will be best to isolate only the affected region. Since it is very difficult to remove UHPC with conventional techniques (i.e.: jackhammering), it may be necessary to sawcut the conventional concrete deck adjacent to the joint. If the reinforcement is cut in the process, it may be necessary to dowel new rebar which can be difficult, especially for narrow joint widths.

Q: What material tests should be used for quality assurance?

A: ASTM material tests are preferred because of the repeatability and access to labs which can perform them. Custom tests, while potentially providing more pertinent information (like bond), are not preferred.

Q: What is the availability of the various materials required to mix UHPC on a large-scale project?

A: All materials involved in this mix are readily available from local manufacturers. A Certificate of Material Origin is required by law to ensure all materials originate from the United States of America.

Appendix C
ASTM MATERIAL STRENGTH SPECIMENS

Compression Cube

Each compression cube was tested in the 300-kip Baldwin® machine with two linear potentiometers to measure the movement of the loading head (see schematic in Appendix Figure C.1). The cubes provided a measure of compressive strength calculated by Equation (15).

$$f_c = \frac{P}{B^2} \tag{15}$$

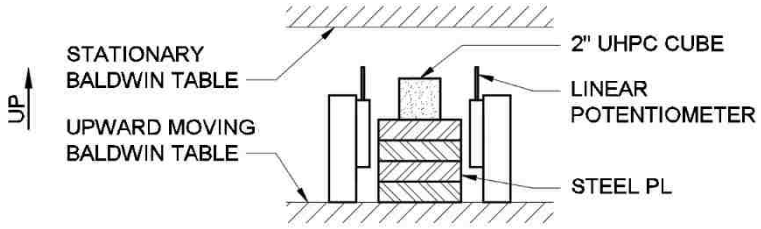

Appendix Figure C.1. Section view of the compression cube testing setup.

Compression Cylinder

Each compression cylinder was capped with a molten sulfur compound to provide a level loading surface. The loading procedure mimicked the compression cube procedure (see schematic in Appendix Figure C.2). The cylinders provided a secondary measure of compressive strength, calculated by Equation (16).

$$f_c = \frac{4P}{\pi D^2} \quad \textbf{(16)}$$

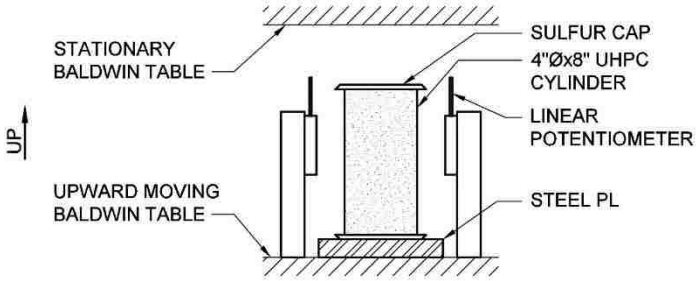

Appendix Figure C.2. Section view of the compression cylinder testing setup.

Split-Tension Cylinder

The split-tension cylinder was placed in the standard ASTM apparatus to load the cylinder using the 300-kip Baldwin® (see schematics in Appendix Figure C.3 and Appendix Figure C.4). The cylinders provided a measure of the UHPC's tensile splitting strength, calculated per Equation (17).

$$f_t = \frac{2P}{\pi DL} \quad \textbf{(17)}$$

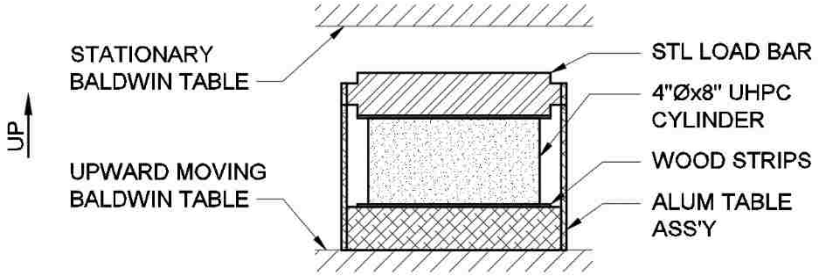

Appendix Figure C.3. Longitudinal section view of the split-tension cylinder testing setup.

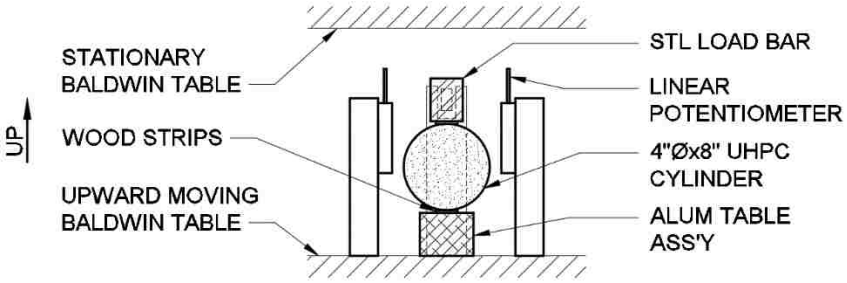

Appendix Figure C.4. Transverse section view of the split-tension cylinder testing setup.

Flexural Beam

Each flexural beam was placed in the ASTM-standard assembly with 12-inch support spacing and loading using the 300-kip Baldwin® (see schematics in Appendix Figure C.5 and Appendix Figure C.6). The beams provided measure of the UHPC's modulus of rupture, calculated per Equation (18).

$$f_r = \frac{3PL}{4BD^2} \tag{18}$$

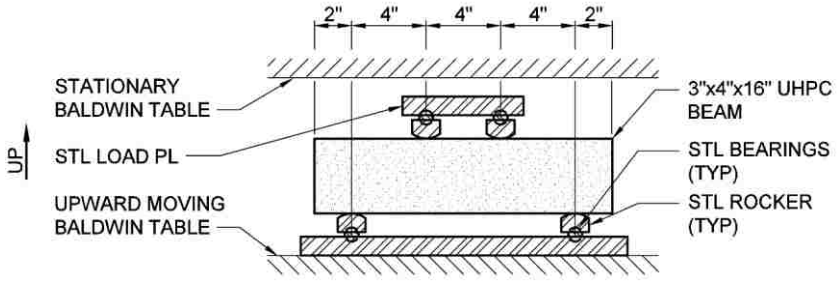

Appendix Figure C.5. Longitudinal section view of the flexural beam testing setup.

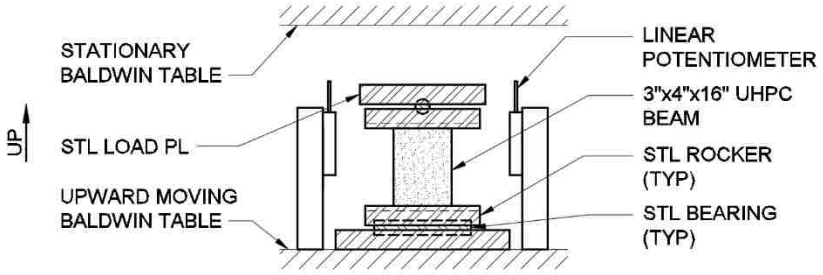

Appendix Figure C.6. Transverse section view of the flexural beam testing setup.

Modulus of Elasticity Cylinder

The cylinders were placed with the ASTM-standard bracket mount shown in Appendix Figure C.7 to measure parameters in Equation (19) to calculate the modulus of elasticity.

$$E_c = \frac{S_2 - S_1}{\varepsilon_2 - 0.000050} \quad \textbf{(19)}$$

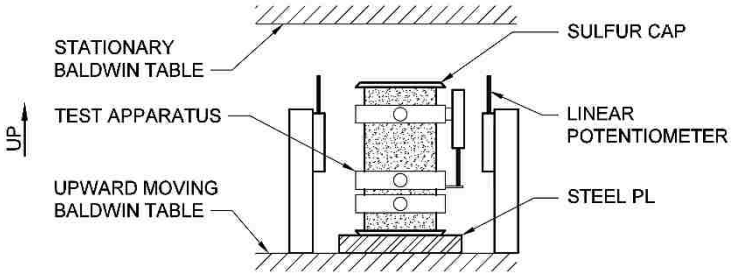

Appendix Figure C.7. Section view of the modulus of elasticity cylinder testing setup.

Appendix D
UHPC MIXING PROCEDURE

1. Weigh two-thirds of the required water in a small bucket, two-thirds of the required HRWRA in a separate small bucket, all the silica fume in a separate large bucket, and an amount of sand equal to the silica fume weight in a separate large bucket.
2. Divide and combine these materials in multiple large buckets. Add the silica fume first, the sand second, the water third, and the HRWRA last.
3. Weigh the remaining one-third of water in a separate small bucket, and the remaining one-third of HRWRA in a separate small bucket.
4. Weigh the remaining required sand and all the required cement in separate large buckets.
5. Weigh the required steel fibers in a separate large bucket.
6. Pour the remaining sand from Step 4 in the mixer, then pour in all the cement. Turn on the mixer and mix for 2-3 minutes until the sand becomes easily visible on the surface.
7. Empty the contents of the mixer into a series of large buckets.
8. Mix the constituents from Step 2 with a power drill attached with a mixing paddle for 1-2 minutes until the mix forms a slurry. Rinse the mixing paddle in the bucket containing the remaining one-third of water.
9. Pour the silica fume slurry into the mixer and use most of the remaining one-third water to rinse the remains of the slurry buckets into the mixer.
10. Pour the remaining one-third of HRWRA into the mixer and use the remaining one-third water to rinse out the bucket containing HRWRA.

11. Turn on the mixer.
12. Very slowly add the buckets of dry-mixed sand and cement into the mixer. Allow the added dry constituents to become well-hydrated before continuing and ensure any large clumps have been eliminated. Continue until the mix forms a paste with consistency similar to that of a fluid grout. This should require 30-40 minutes.
13. Slowly add all steel fibers while the mixer continues to run. This should require 5-6 minutes.
14. Once all steel fibers have been added, continue mixing for 3-4 minutes.
15. Empty the contents of the mixer into a wheelbarrow for transport and pouring.

The total time allotted for mechanical mixing ranges from 41-55 minutes, with additional time required for weighing materials. An average spread of 8.5 inches was achieved with no disturbance and this was increased to an average of 9 to 9.5 inches after performing ASTM C1611-specified table-drops (ASTM International 2014).

This procedure was developed when mixing close to the maximum capacity of the relatively low-powered mixer, so the required mixing times may be reduced with smaller batches or more powerful mixers. Mixing in a larger-capacity commercial mixer would doubtless require different procedures and mixing times, and trial batches should be mixed before filling a joint. However, the differences between this mixing procedure and Qiao's, and the structural results obtained, suggest that the thoroughness of the mixing has a significant effect on the material properties.

Appendix E
EXPERIMENTAL TEST SPECIMEN DESCRIPTIONS

E.1 Pullout Bond Curb

WSDOT's DBT girders have a 6-inch thick deck at the location of the UHPC joint, but a 7-inch curb was implemented to accommodate any potential changes in the clear cover parameter (Washington State Department of Transportation 2016). For construction simplicity, each curb was filled with the reinforcement projecting vertically. Although this is not same casting direction as would be realized on-site, the rationale was that the combination of a low water-cement ratio and absence of large aggregate eliminated concern with settling aggregate or excessive water bleeding to the surface that would create variation in concrete quality through the thickness. Graybeal also concluded that casting direction does not significantly influence UHPC strength (Graybeal, Bond Behavior of Reinforcing Steel in Ultra-High Performance Concrete 2014).

The 6-inch rebar spacing was a deck reinforcement specification per WSDOT requests (see figure of WSDOT cross-section) (Washington State Department of Transportation 2016). Each curb hosted the rebar at varying embedment lengths intended to obtain load versus embedment length information. The bases of the pullout curbs were incrementally stepped to minimize cost and provided a means for varying embedment lengths while maintaining similar boundary

conditions at the end of each rebar, that is, there was no UHPC present below the rebar to participate in the bond stress transfer mechanisms.

Each curb was tested using a 50-kip load cell, a 100-ton hydraulic ram, BEI Sensors® linear potentiometers with a 3.5-inch stroke, a prestressing strand chuck, a series of steel plates, and strips of thin wood. The load cell was placed directly atop multiple layers of 1/8-inch thick wood strips that rest on the UHPC curb and spanned the through-thickness direction on two sides of the rebar to provide a compressive load reaction. The hydraulic ram was placed on the load cell with a steel plate in between. Finally, a steel plate was positioned on top of the hydraulic ram's piston and the prestressing chuck was anchored to the rebar at the top of the assembly (see Figure 5.4).

During each test, the hydraulic ram's piston was extended at a controlled rate of approximately 10 kips per minute (monitored while in the elastic region) which pushed against the prestressing chuck and uniaxially stressed the rebar until failure occurred by means of bond failure or rebar fracture.

Deformations were measured by gluing two pre-compressed linear potentiometers to the sides of the hydraulic ram, measuring the piston's travel, and averaging the readings.

E.2 Spliced Connection Bond Curb

Rebar spacing was maintained at 6 inches to represent the reinforcement pattern for DBT girders and the curb thickness was 7 inches for the same reason as the pullout curbs. The epoxy-coated #5 rebar was spliced with #8 rebar which provided a semi-rigid boundary condition such that most deformation was forced into the UHPC between the #5 and #8 bars; any slip or cracking that occurred within the conventional concrete block could not be measured.

Each curb was tested using a 50-kip load cell, a 100-ton hydraulic ram, BEI Sensors® linear potentiometers, a prestressing strand chuck, a series of steel plates, and a loading standoff. The loading standoff consisted of a 1-inch plate and four legs made of 1.5-inch diameter threaded rods which straddled the curb. Each threaded rod leg bears on steel plates atop the conventional concrete base to reduce localized damage. The load cell was placed directly on the loading standoff and the hydraulic ram was then placed on the load cell with a steel plate in between. Finally, a steel plate was positioned on top of the hydraulic ram's piston and the prestressing chuck was anchored to the rebar at the top of the assembly (see Figure 5.6).

The load rate, casting direction, and deformation measuring method was identical to that used for the Pullout Bond Curb experiments.

E.3 Simulated Deck

Rectangular conventional concrete panels reinforced with two layers of epoxy-coated #5 rebar spaced at 6 inches represent one-half of a standard DBT bridge girder flange. Each test specimen utilized one panel with four rebars and one panel with three rebars which overlapped in non-contact spliced configuration joined by UHPC. The panels were 2 feet wide as required to fit the #5 rebars spaced at three inches within the joint. WSDOT imposes a 5-foot minimum and 8-foot maximum transverse girder spacing limit based largely on shipping weights, thus this project utilized the maximum spacing to determine the maximum possible demands. This lead to individual panel lengths of approximately 4.5 feet.

The simulated deck assembly bonded two panels together by means of a UHPC joint in the middle. The joint width varied from 3 inches to 7 inches which was determined to adequately bound the expected results from UHPC failure before the rebar yields up to failure by rebar fracture. These widths were determined by analyzing data from the pullout and splice-

connection curbs. Like the splice-connection curbs, a 1-inch clearance was provided for construction purposes between the end of each rebar and the edge of the conventional concrete panel. The casting orientation for these panels directly mimicked on-site conditions where the rebar with 1-inch clear cover was on the bottom of the panel.

Each simulated deck specimen was tested after approximately 14 days of curing, four of which involved curing within the formwork with wet burlap placed on the top surface to ensure proper curing and minimize shrinkage cracks. The specimen was loaded in 3-point bending by a hydraulic ram with the load applied at midspan to represent a maximum wheel load. HSS rocker assemblies were provided as simple supports to allow for end-rotation and maximize the positive bending moment at the joint. The load from the hydraulic ram was transferred to a 1-inch thick steel plate across the full width of the panel and over a 7-inch length across the joint. A diagram of the test setup was provided in Figure 5.9 through Figure 5.12.

These tests represented an isolated segment of a bridge span, thus there is no splice-connected concrete adjacent to the test specimen as there would be in a real bridge. Thus, there will be no force transfer mechanism for the rebar at the edges of each panel. As a result, the edge rebar will create a weaker splice connection and there will be nothing to prevent side-splitting cracks from laterally propagating to the edge of the panel.

To simulate the real behavior of the splice-connected joint and offset this effect, an assembly of steel plates was mounted to both sides of each panel with threaded rods to connect them. An additional hydraulic ram was mounted to one side of the panel centered at mid-thickness which will incrementally post-tension the panel as it is loaded.

Ultimately, this setup aimed to provide plane strain boundary conditions by restraining displacements along the width of the slab like how adjacent concrete restrains the splice connection in a real bridge. Displacements were monitored by attaching one linear potentiometer in between the confinement plates at both the top and bottom of the slab which measure the lateral expansion of the joint at each load stage. The hydraulic rams were activated when the expansive displacement read 0.01 inches which brought this displacement back near zero.

Data acquisition for each panel specimen involved a load cell, linear potentiometers, and an Optotrak® camera system. The load cell was used to measure the midspan load. Linear potentiometers were implemented to monitor the lateral expansion of the panel as mentioned above, record any vertical slip at the supports, and record the vertical midspan deflection of the panel. The Optotrak® system recorded the movement of LED markers which were placed atop the UHPC joint and on both sides of the interface between the concrete panel and UHPC such that cracks can be measured and mapped. Any cracks which formed due to bond failure were expected to be located close to the centerline of each rebar and at the interface of the joint. Thus, these markers were strategically placed on the surface of the joint above where the rebar is located and on either side of the interface.

Appendix F
ADDITIONAL DATA FIGURES

F.1 Finite Element Analysis Stress Distribution

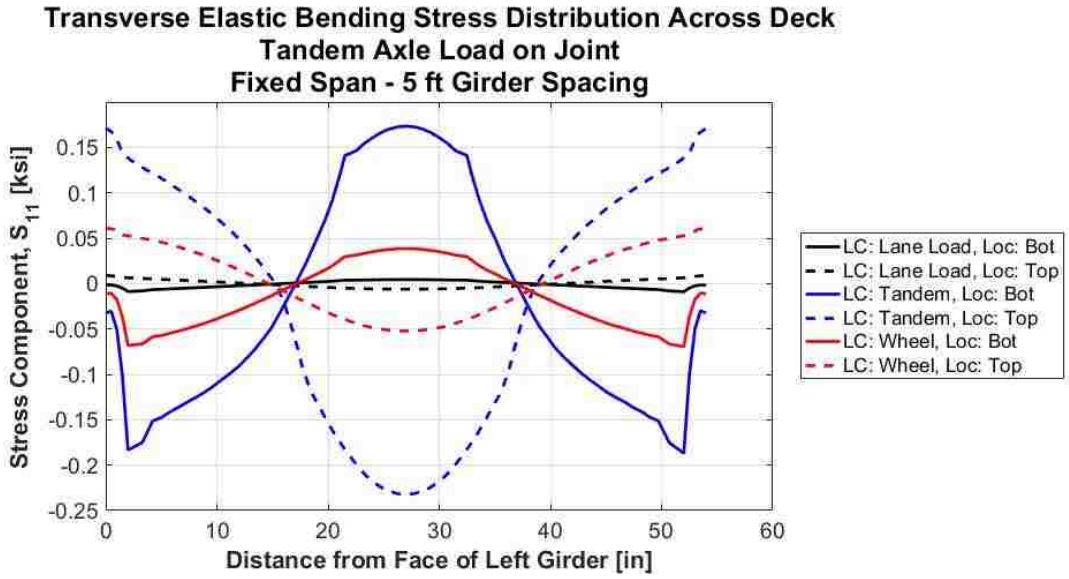

Appendix Figure F.1. Transverse elastic bending stress distribution across the bridge deck for a tandem axle load placed on the joint for the fixed-boundary configuration with 5-foot girder spacing.

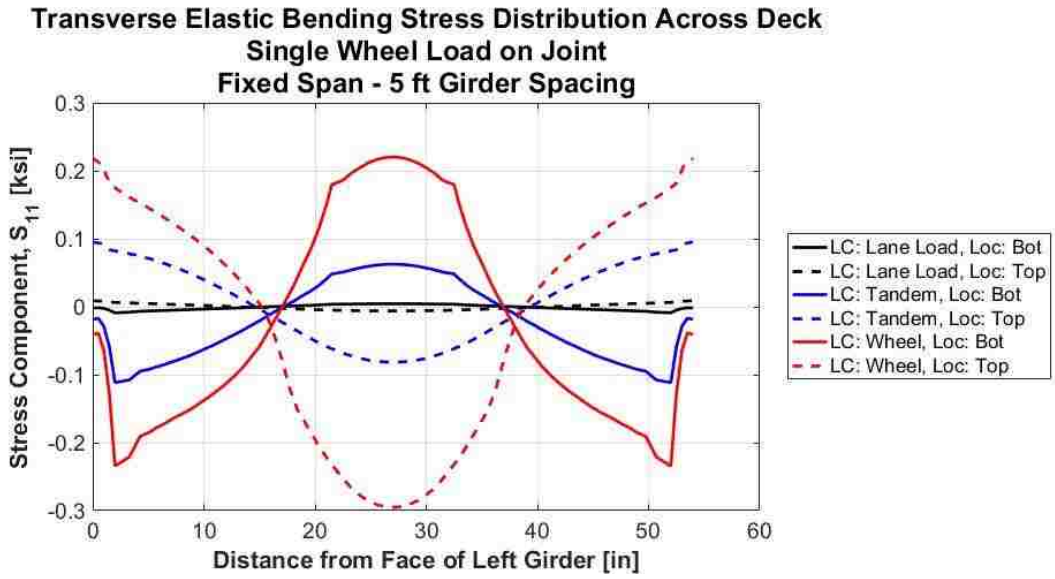

Appendix Figure F.2 Transverse elastic bending stress distribution across the bridge deck for a single wheel load placed on the joint for the fixed-boundary configuration with 5-foot girder spacing.

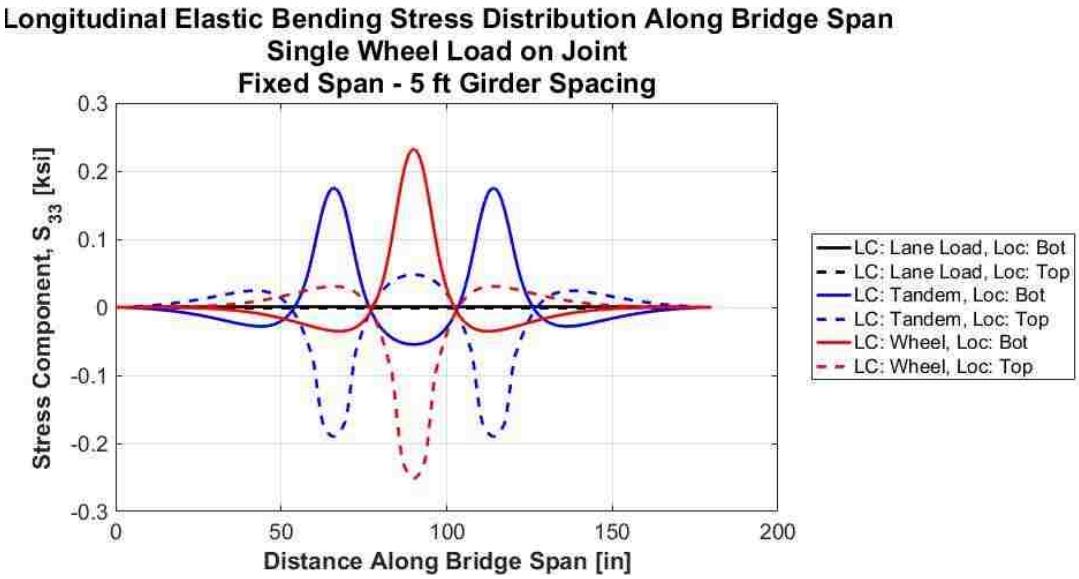

Appendix Figure F.3 Longitudinal elastic bending stress distribution along the bridge span for a single wheel load placed on the joint for the fixed-boundary configuration with 5-foot girder spacing.

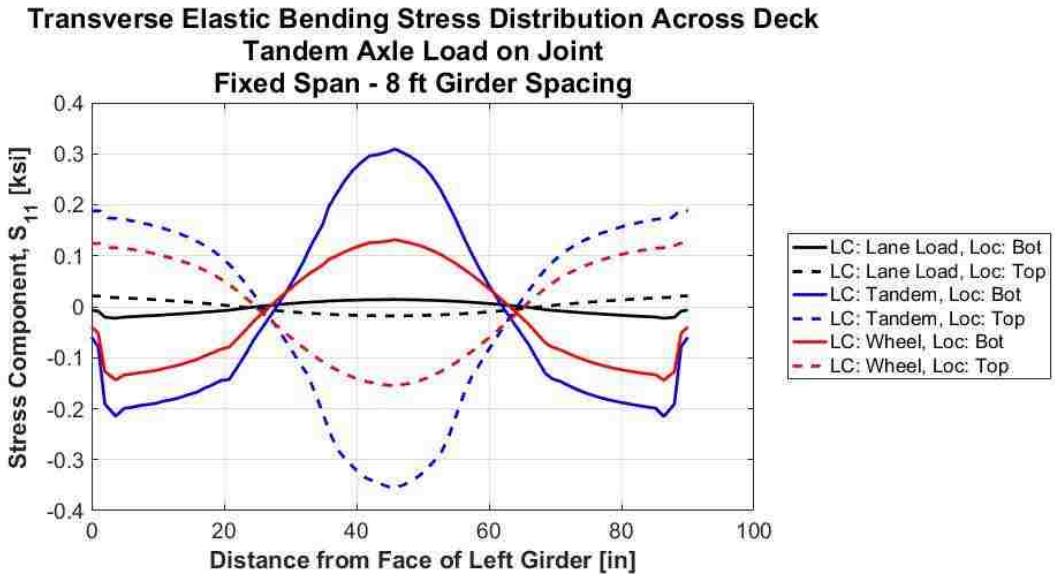

Appendix Figure F.4 Transverse elastic bending stress distribution across the bridge deck for a tandem axle load placed on the joint for the fixed-boundary configuration with 8-foot girder spacing.

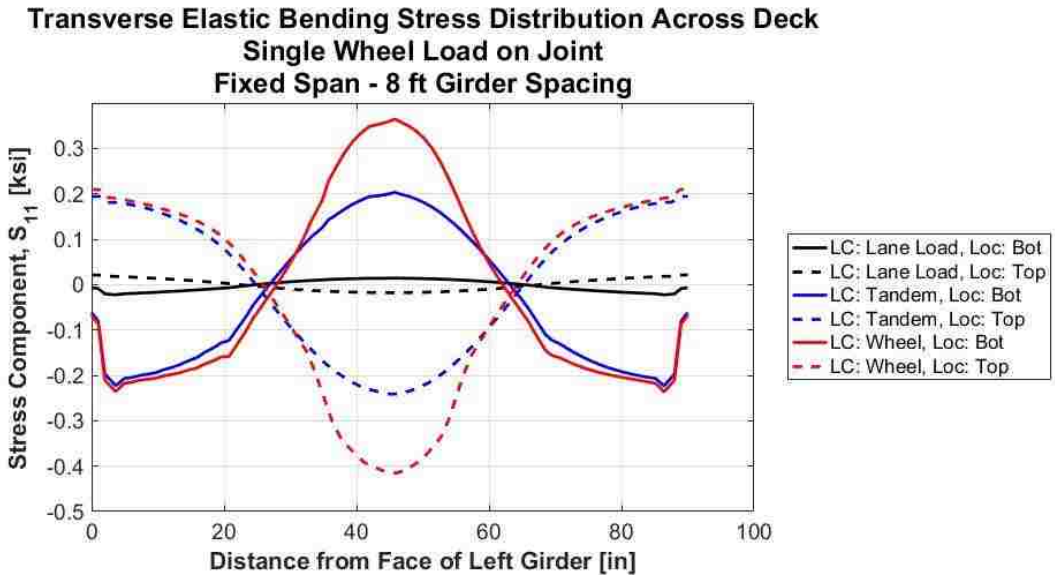

Appendix Figure F.5 Transverse elastic bending stress distribution across the bridge deck for a single wheel load placed on the joint for the fixed-boundary configuration with 8-foot girder spacing.

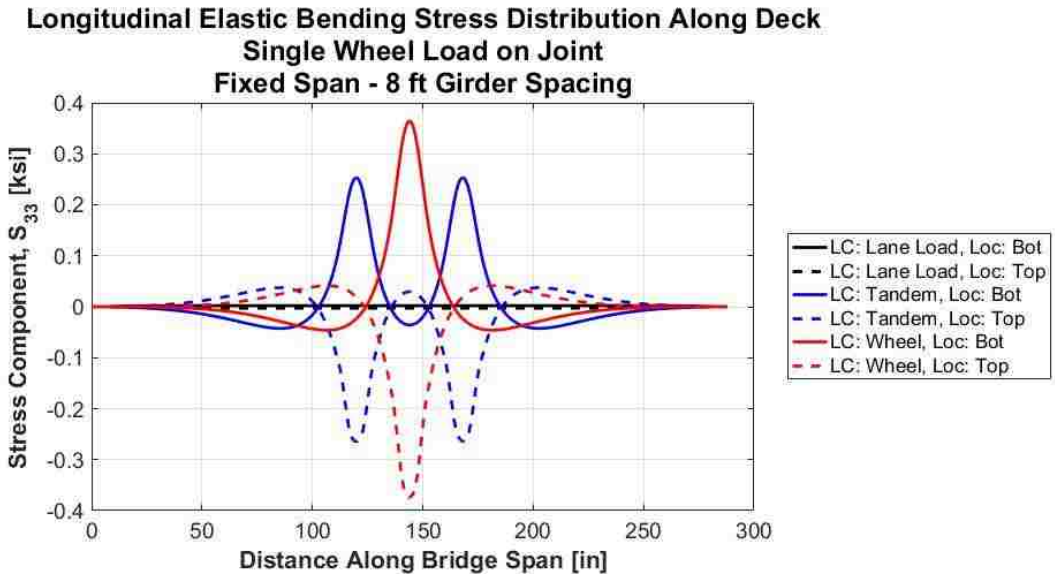

Appendix Figure F.6 Longitudinal elastic bending stress distribution along the bridge span for a single wheel load placed on the joint for the fixed-boundary configuration with 8-foot girder spacing.

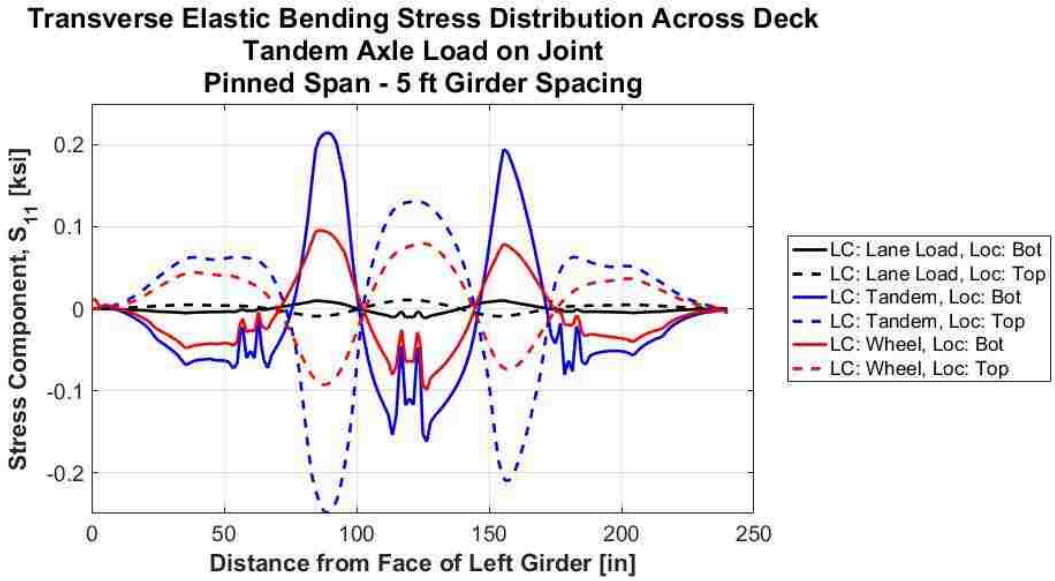

Appendix Figure F.7 Transverse elastic bending stress distribution across the bridge deck for a tandem axle load placed on the joint for the pinned-boundary configuration with 5-foot girder spacing.

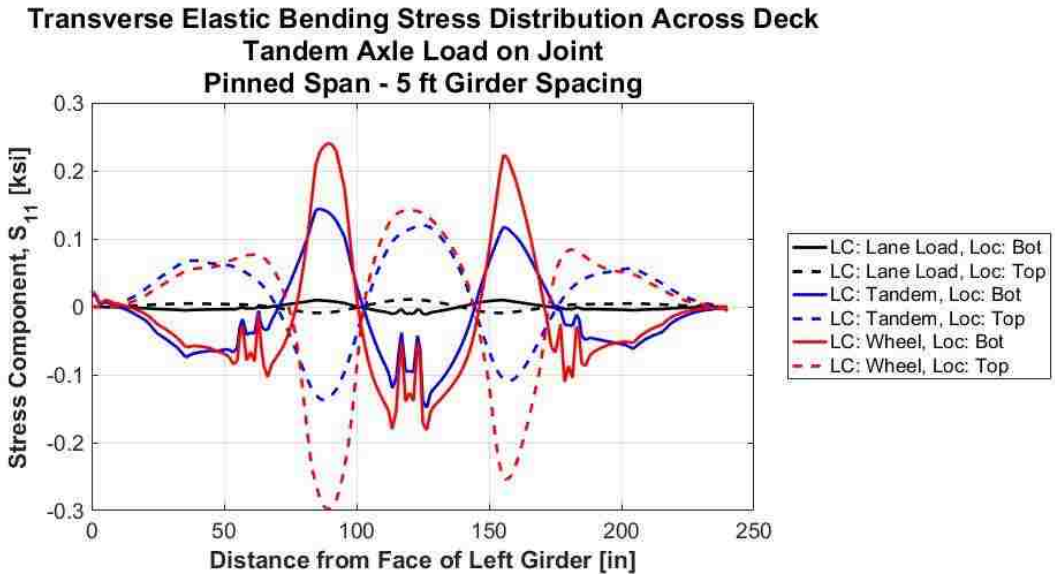

Appendix Figure F.8 Transverse elastic bending stress distribution across the bridge deck for a single wheel load placed on the joint for the pinned-boundary configuration with 5-foot girder spacing.

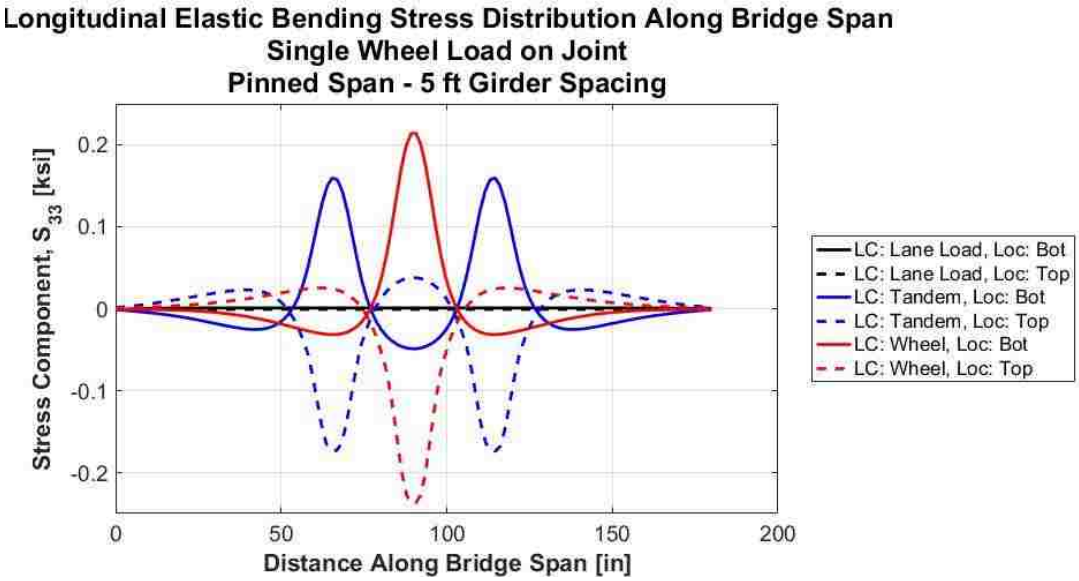

Appendix Figure F.9 Longitudinal elastic bending stress distribution along the bridge span for a single wheel load placed on the joint for the pinned-boundary configuration with 5-foot girder spacing.

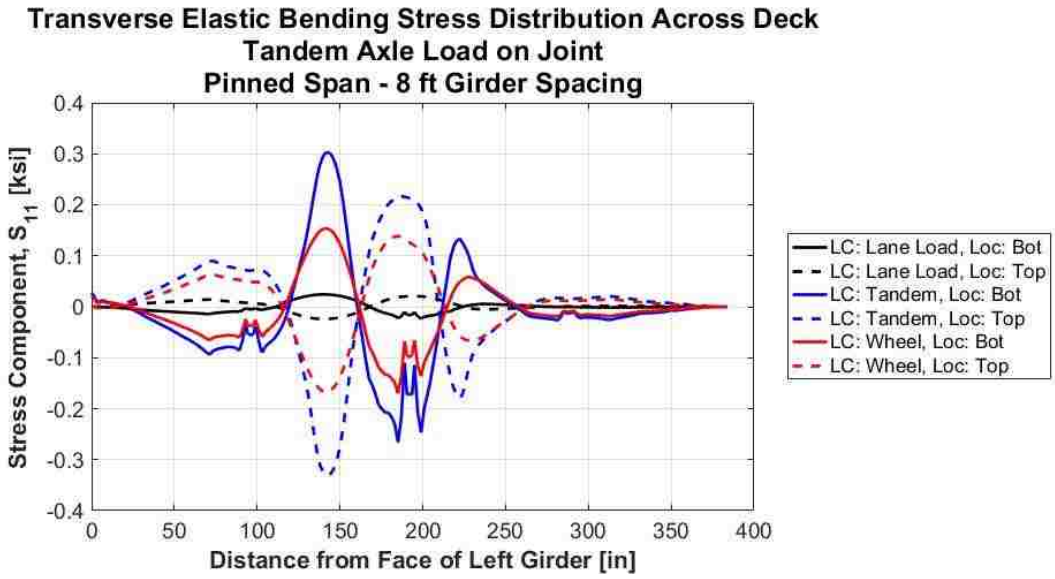

Appendix Figure F.10 Transverse elastic bending stress distribution across the bridge deck for a tandem axle load placed on the joint for the pinned-boundary configuration with 8-foot girder spacing.

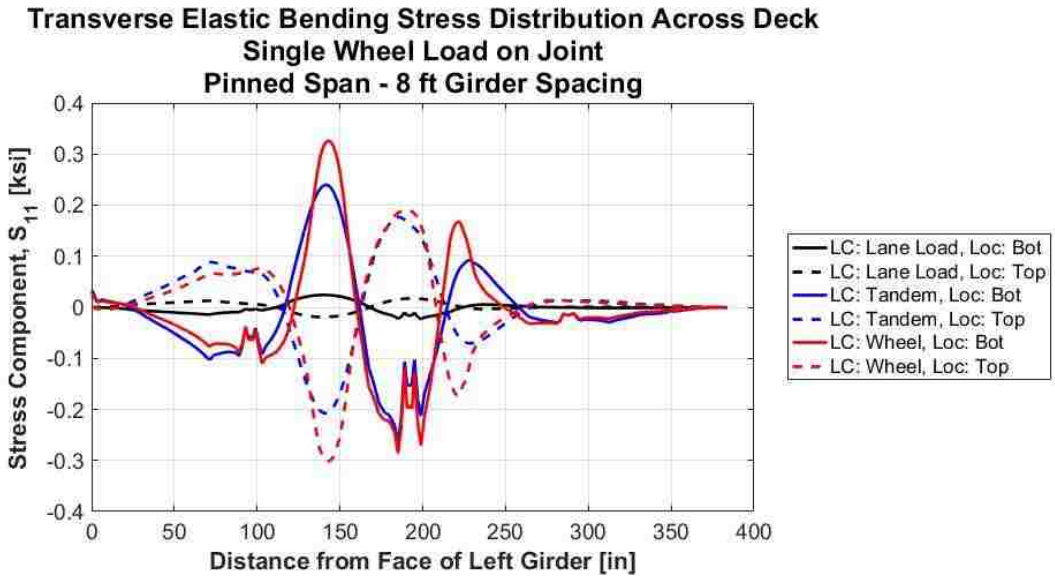

Appendix Figure F.11 Transverse elastic bending stress distribution across the bridge deck for a single wheel load placed on the joint for the pinned-boundary configuration with 8-foot girder spacing.

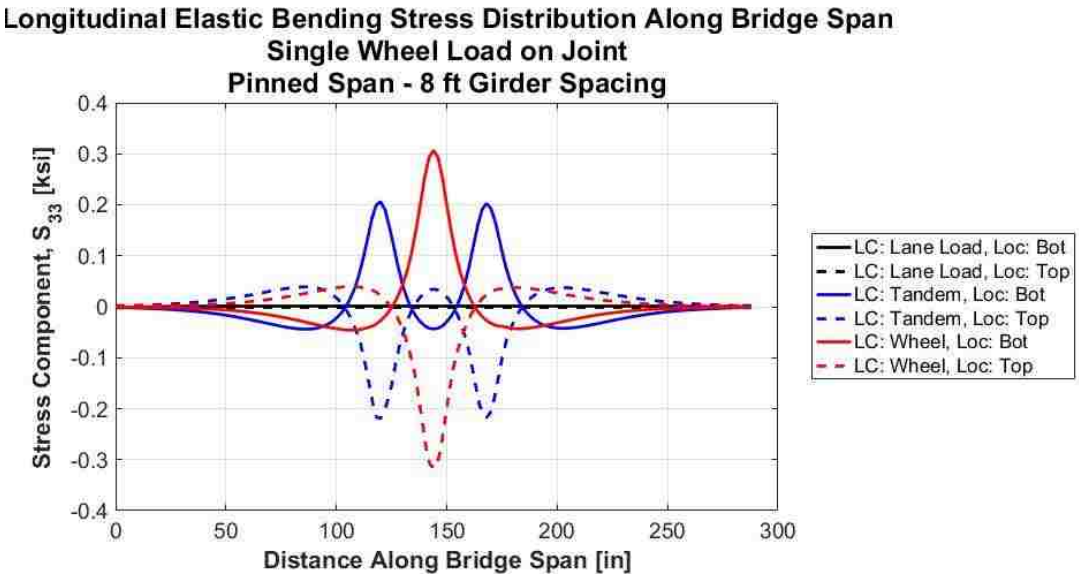

Appendix Figure F.12 Longitudinal elastic bending stress distribution along the bridge span for a single wheel load placed on the joint for the pinned-boundary configuration with 8-foot girder spacing.

F.2 Material Strength Load-Deflection Curves

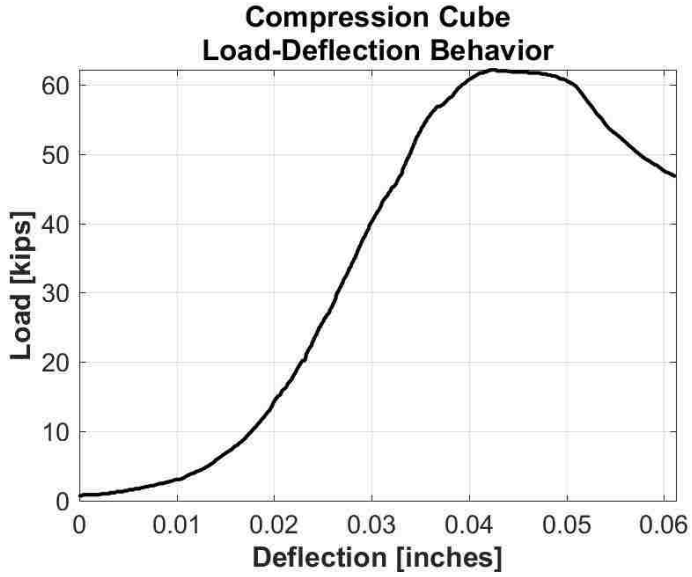

Appendix Figure F.13. Typical compression cube load-deflection behavior.

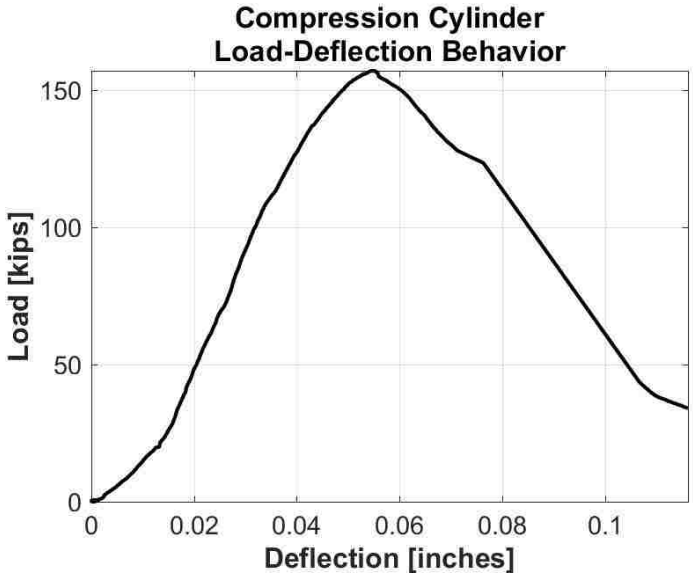

Appendix Figure F.14. Typical UHPC compression cylinder load-deflection behavior.

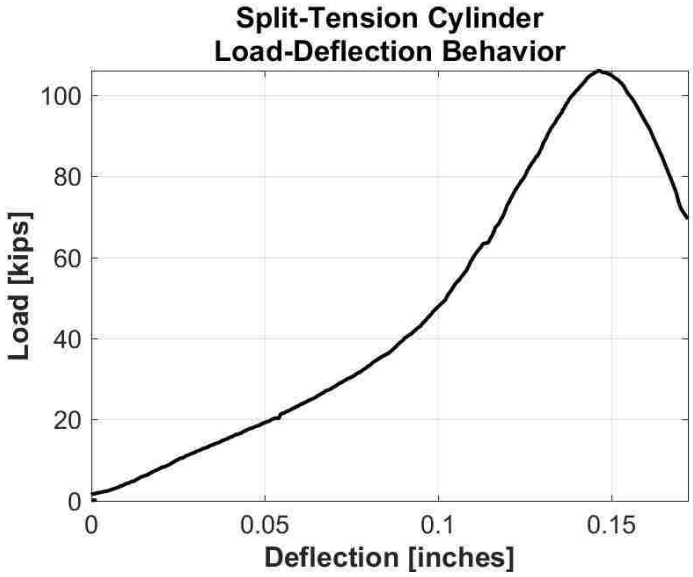

Appendix Figure F.15. Typical split-tension cylinder load-deflection behavior.

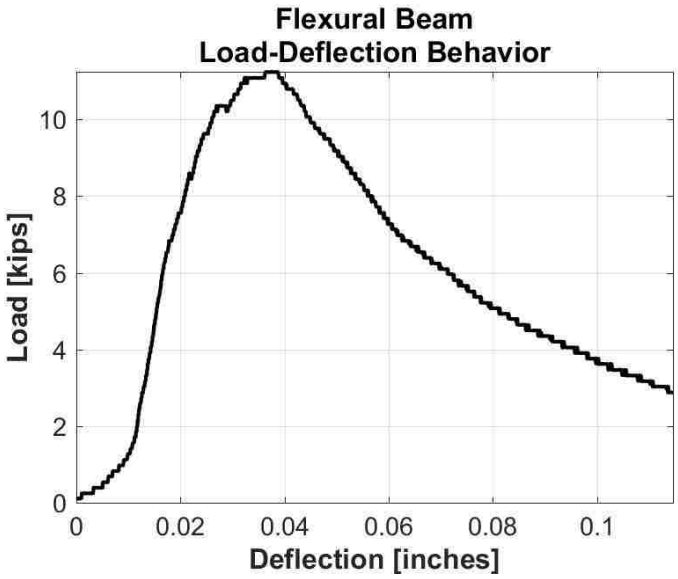

Appendix Figure F.16. Typical flexural beam load-deflection behavior.

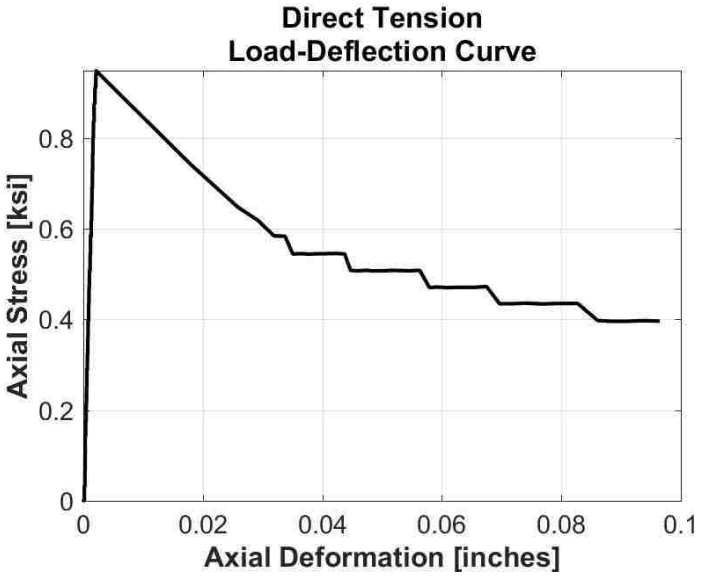

Figure 0.1. Typical direct tension test load-deflection curve.

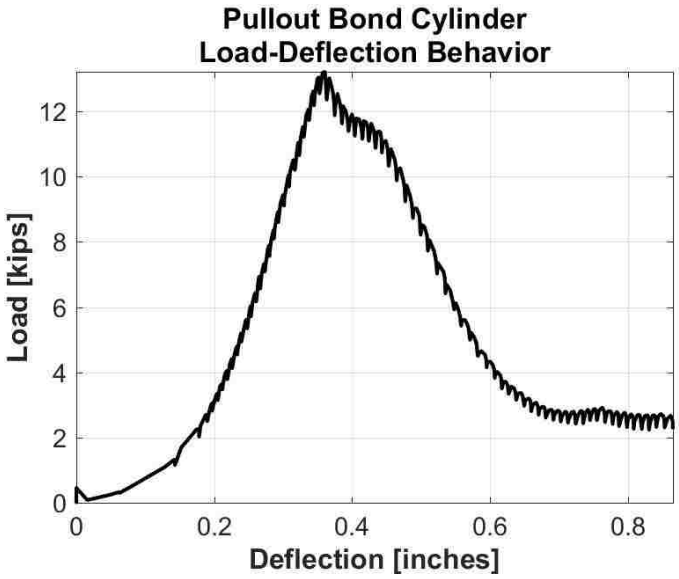

Appendix Figure F.17. Typical pullout bond cylinder load-deflection curve.

F.3 Material Strength Histograms

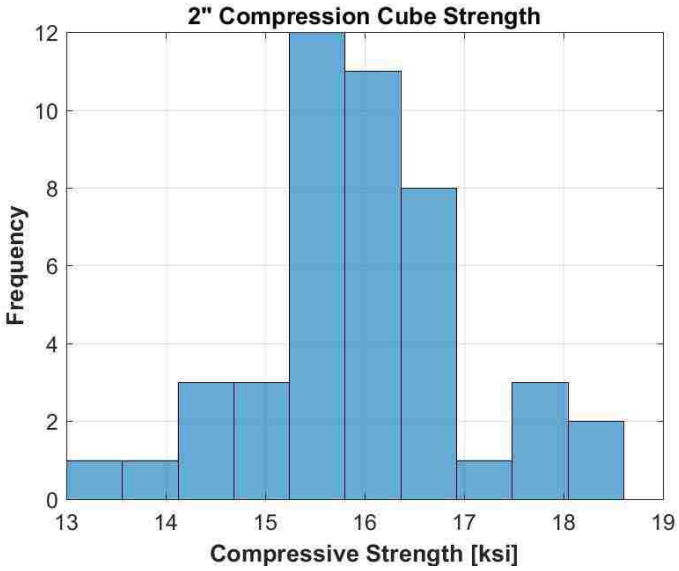

Appendix Figure F.18. 14-day strength distribution for all compression cube specimens.

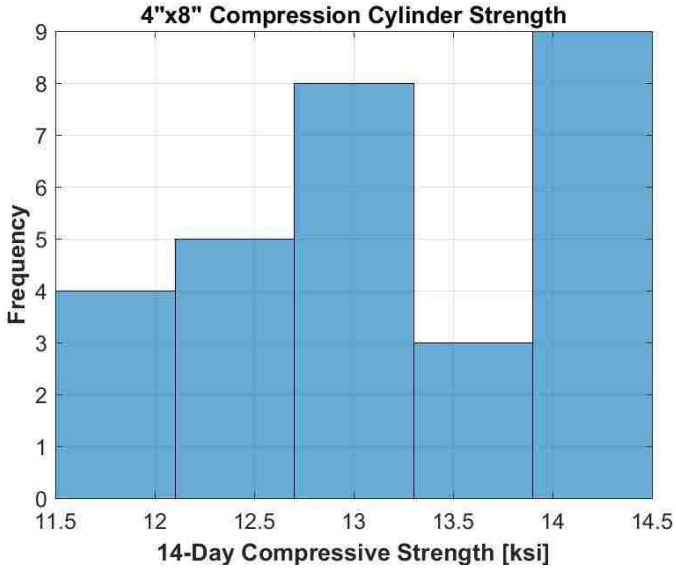

Appendix Figure F.19. 14-day strength distribution for all UHPC compression cylinder specimens.

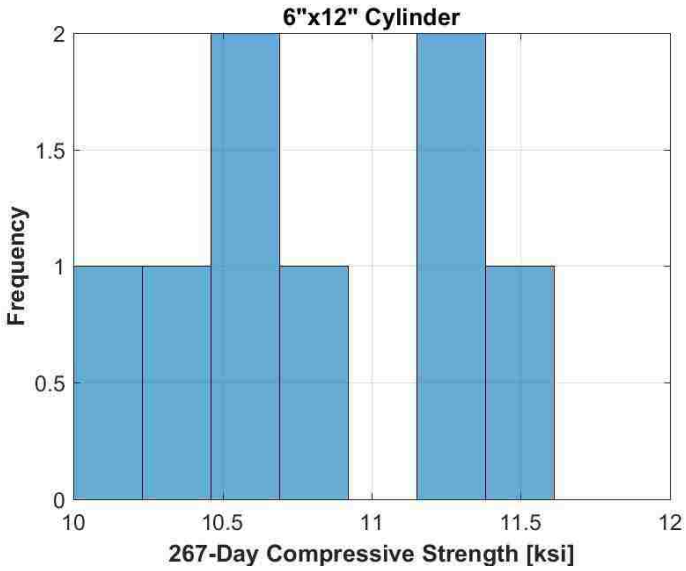

Appendix Figure F.20. 14-day strength distribution for all conventional concrete compression cylinder specimens.

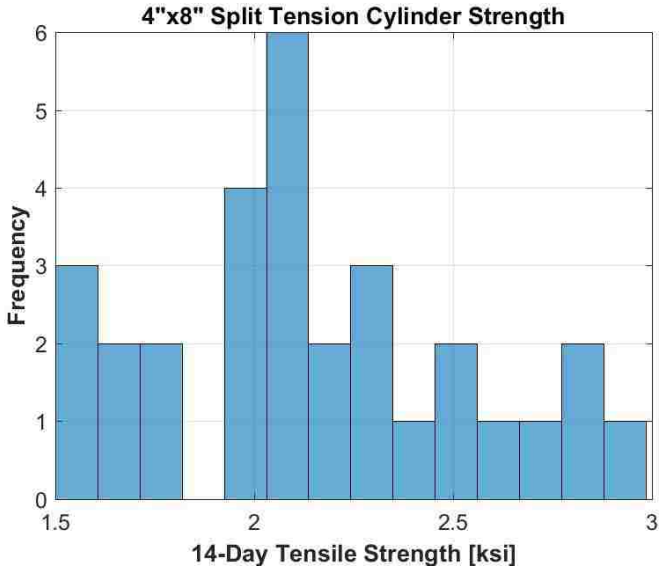

Appendix Figure F.21. 14-day strength distribution for all split-tension cylinder specimens.

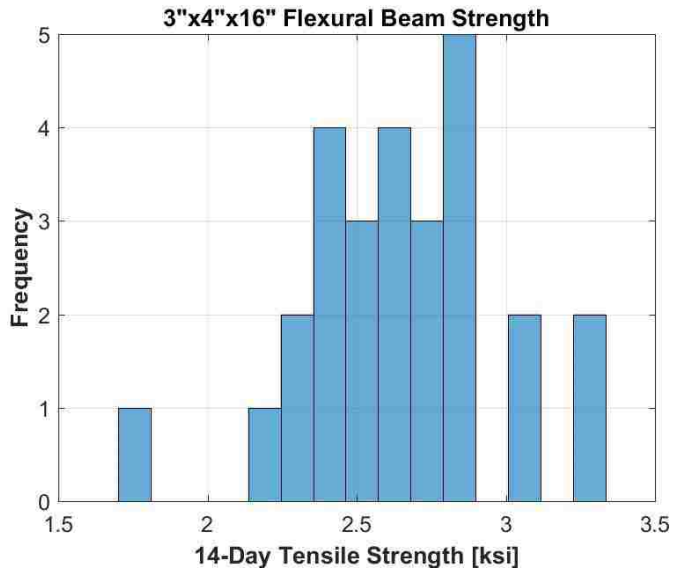

Appendix Figure F.22. 14-day strength distribution for all flexural beam specimens.

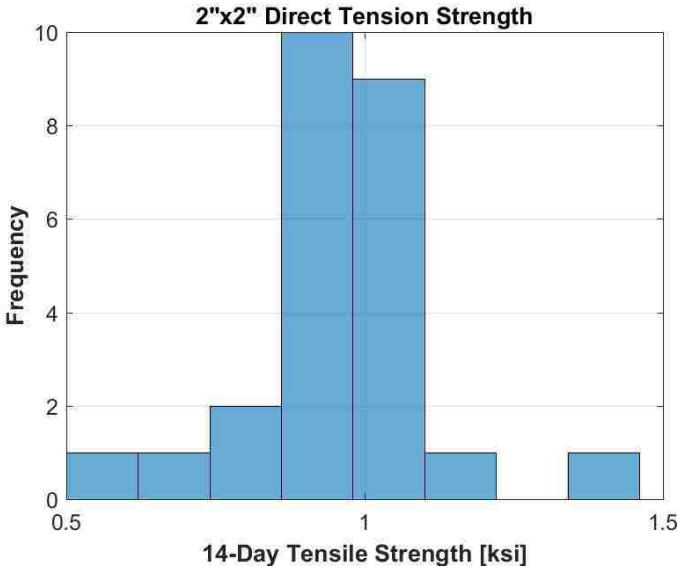

Appendix Figure F.23. 14-day strength distribution for all direct tension specimens.

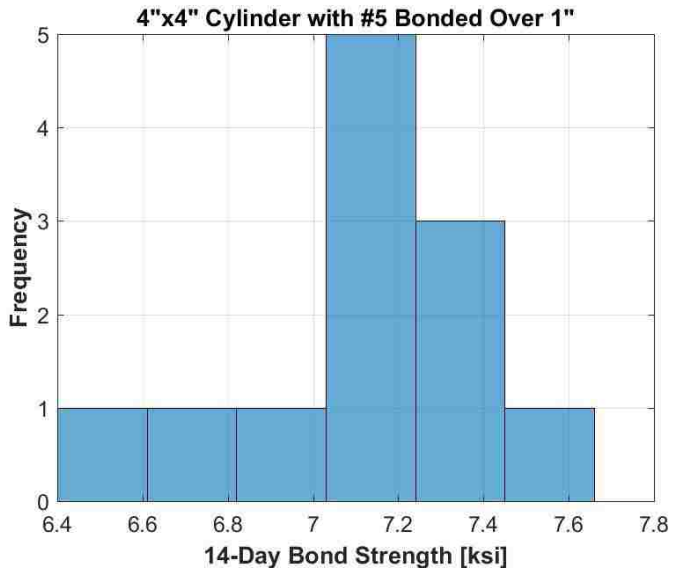

Appendix Figure F.24. 14-day strength distribution for all pullout bond cylinder specimens.

F.4 Strength Gain with Time Curves

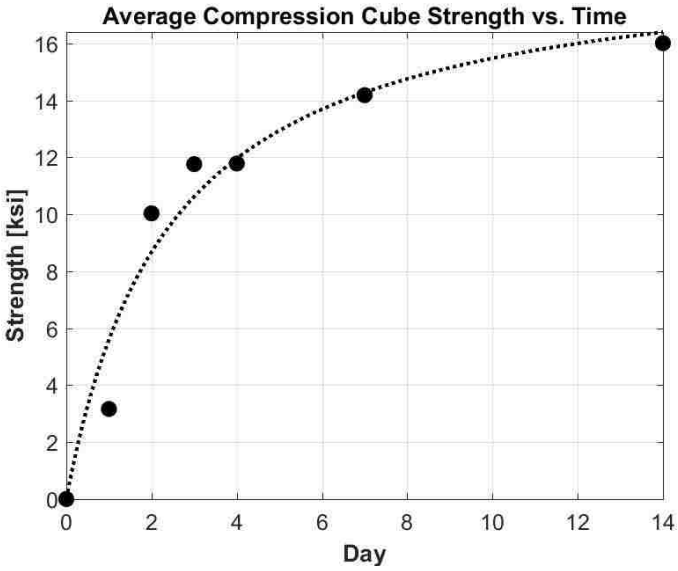

Appendix Figure F.25. S/T data with curve-fit for compression cube specimens.

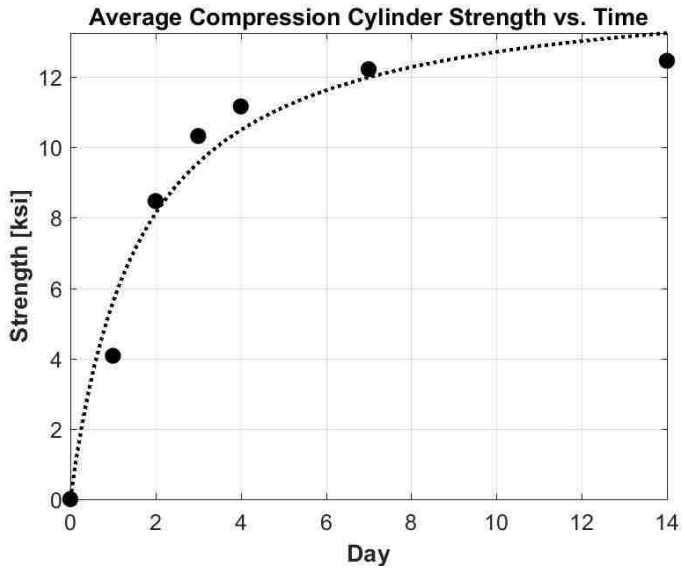

Appendix Figure F.26. S/T data with curve-fit for UHPC compression cylinder specimens.

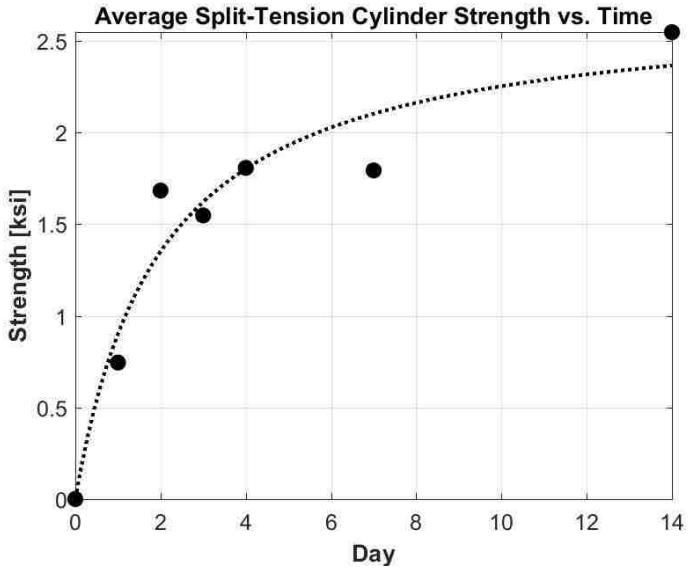

Appendix Figure F.27. S/T data with curve-fit for split-tension cylinder specimens.

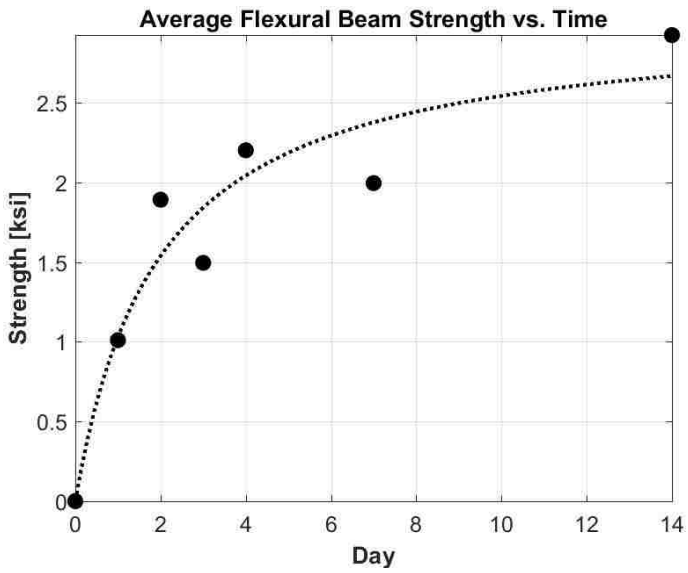

Appendix Figure F.28. S/T data with curve-fit for flexural beam specimens.

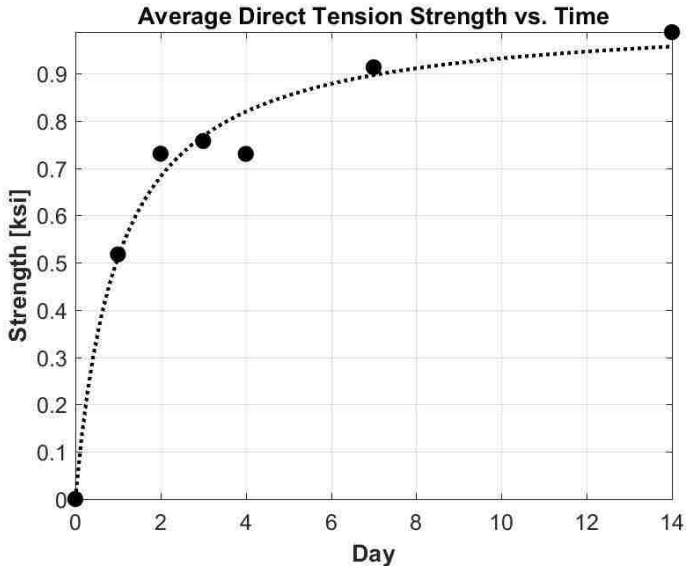

Appendix Figure F.29. S/T data with curve-fit for direct tension specimens.

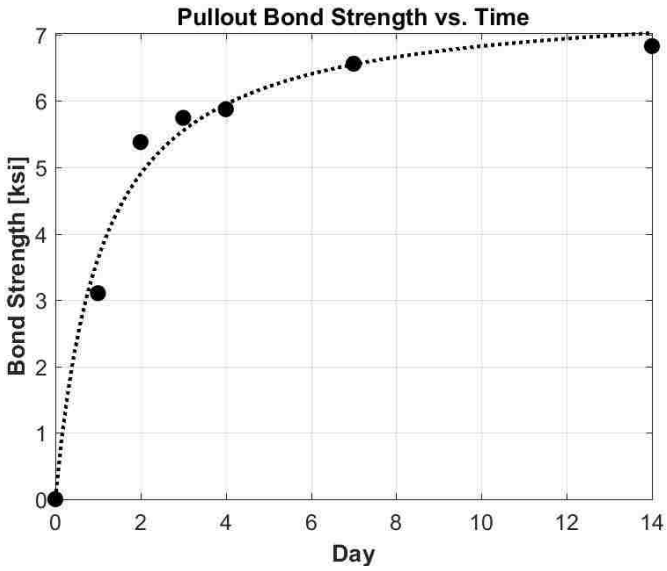

Appendix Figure F.30. S/T data with curve-fit for pullout bond cylinder specimens.

F.5 Pullout Bond Curb Bar Stress-Deflection Curves

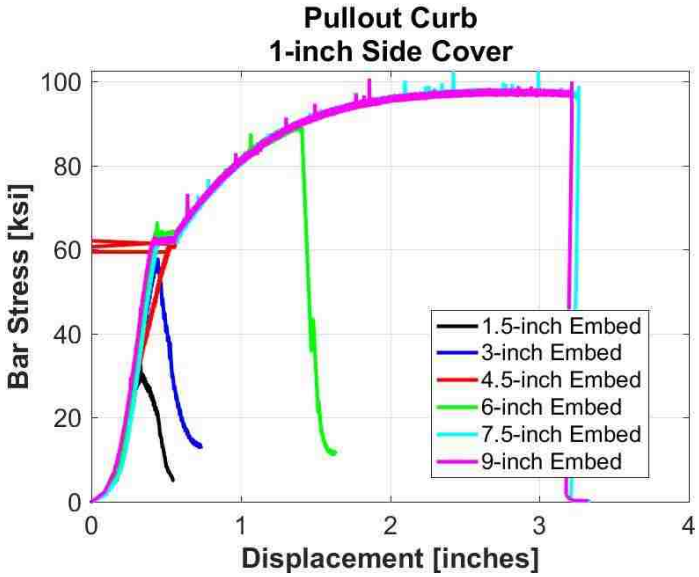

Appendix Figure F.31. Bar stress versus axial deformation curves for all Pullout Bond Curb specimens with 1-inch side cover.

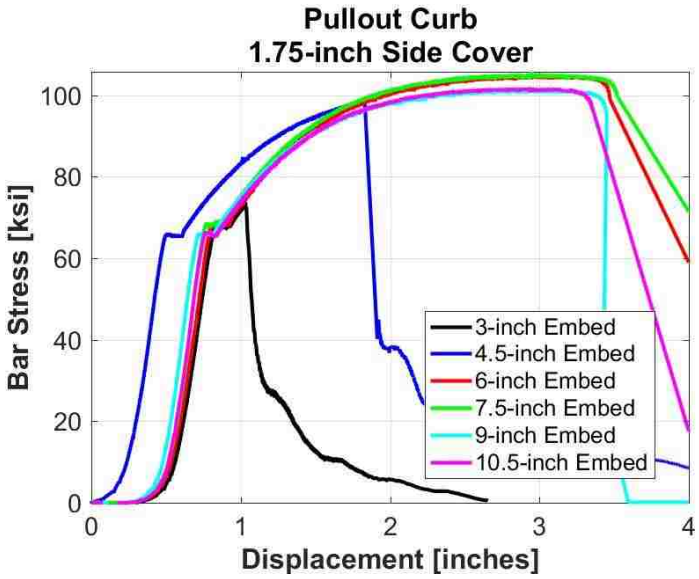

Appendix Figure F.32. Bar stress versus axial deformation curves for all Pullout Bond Curb specimens with 1.75-inch side cover.

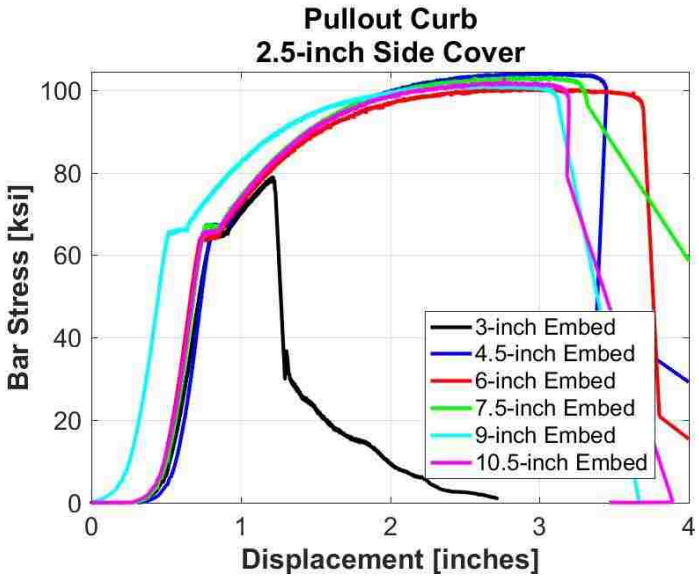

Appendix Figure F.33. Bar stress versus axial deformation curves for all Pullout Bond Curb specimens with 2.5-inch side cover.

F.6 Spliced-Connection Bond Curb Load-Deflection Curves

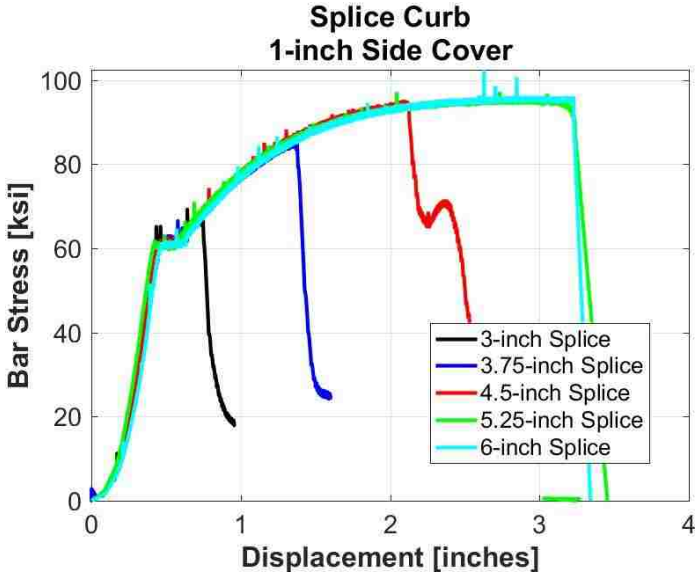

Appendix Figure F.34. Bar stress versus axial deformation curves for all Splice-Connection Bond Curb specimens with 1-inch side cover.

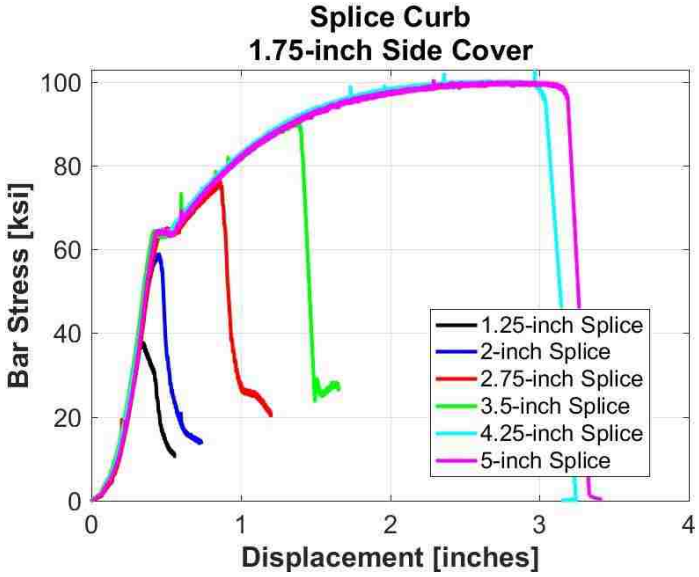

Appendix Figure F.35. Bar stress versus axial deformation curves for all Splice-Connection Bond Curb specimens with 1.75-inch side cover.

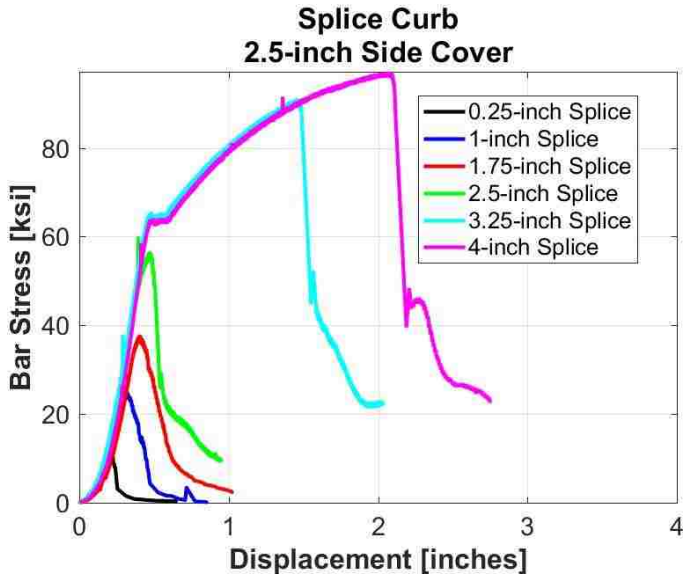

Appendix Figure F.36. Bar stress versus axial deformation curves for all Splice-Connection Bond Curb specimens with 2.5-inch side cover.

F.7 Simulated Deck Interfacial Crack Width Curves

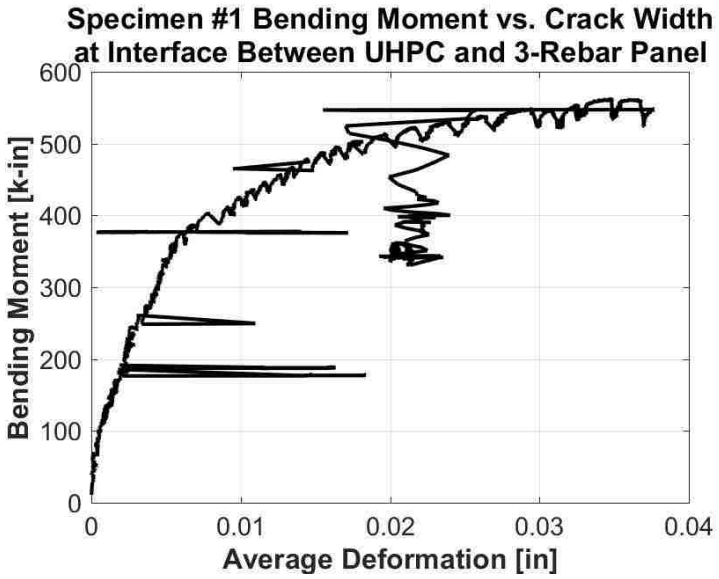

Appendix Figure F.37. Midspan bending moment versus interfacial crack width for Simulated Deck Specimen #1‡‡.

‡‡ Optotrak camera system's coordinate system was not aligned properly. Interfacial crack width magnitudes are inaccurate.

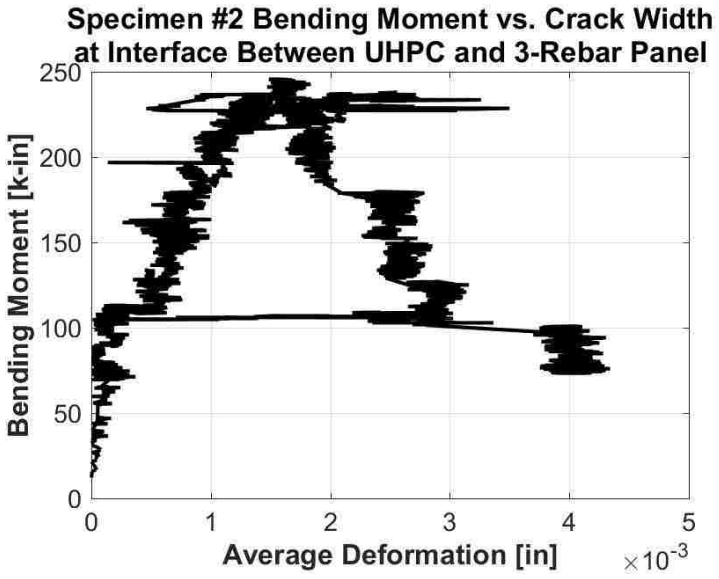

Appendix Figure F.38. Midspan bending moment versus interfacial crack width for Simulated Deck Specimen #2‡‡.

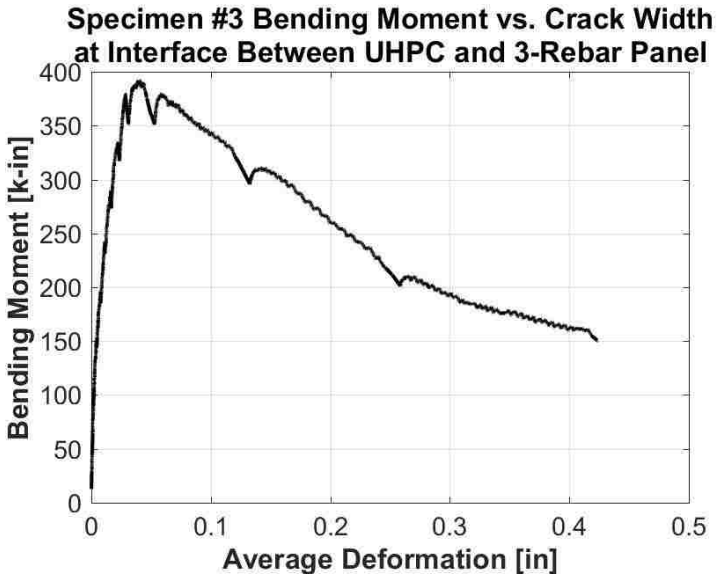

Appendix Figure F.39. Midspan bending moment versus interfacial crack width for Simulated Deck Specimen #3.

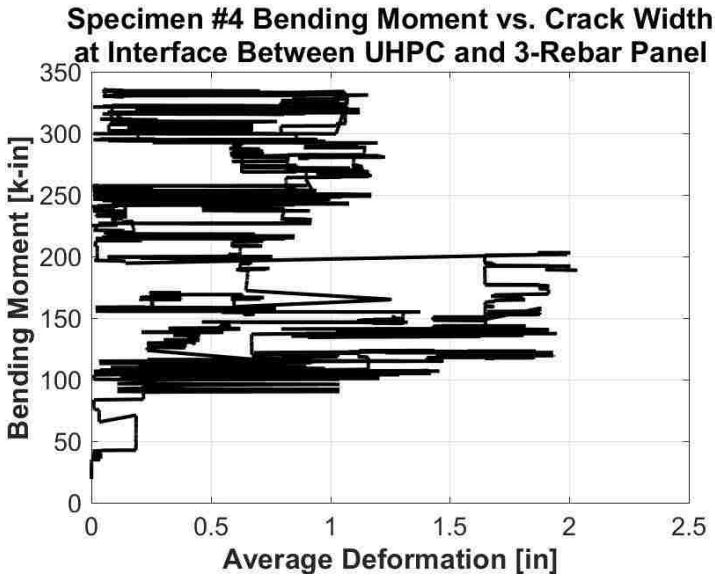

Appendix Figure F.40. Midspan bending moment versus interfacial crack width for Simulated Deck Specimen #4[§§].

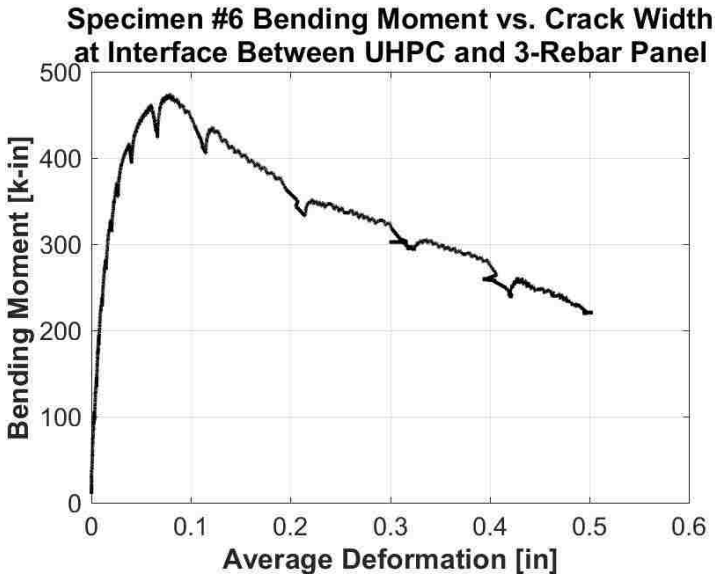

Appendix Figure F.41. Midspan bending moment versus interfacial crack width for Simulated Deck Specimen #6.

[§§] Optotrak camera system was interrupted during experiment.

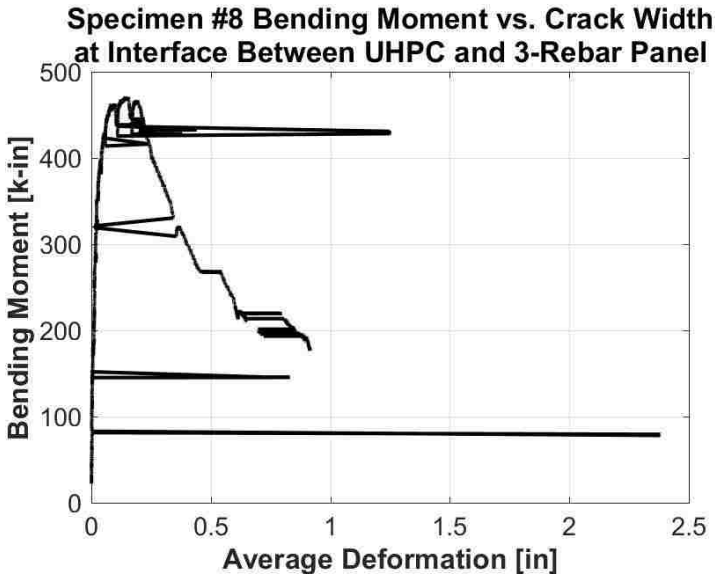

Appendix Figure F.42. Midspan bending moment versus interfacial crack width for Simulated Deck Specimen #8.

Appendix G
CALCULATIONS

G.1 Finite Element Analysis Stress Summary

Appendix Table G.1 lists both the transverse and longitudinal stress components for each analysis and load case.

Appendix Table G.1. FEA stress summary.

LIVE LOAD - TOP STRESSES @ JOINT CL [ksi]											
		Through Tandem Line				Through Wheel Line				ABS WORST CASE	
		Lane Load	Tandem Load	Wheel Load	Abs Magnitude	Lane Load	Tandem Load	Wheel Load	Abs Magnitude	Location	Abs Magnitude
S11	Fixed5	-0.006	-0.232	-0.052	**0.238**	-0.006	-0.082	-0.295	**0.301**	Wheel Line	0.301
	Fixed8	-0.018	-0.354	-0.155	**0.372**	-0.018	-0.241	-0.415	**0.433**	Wheel Line	0.433
	Pinned5	-0.008	-0.249	-0.092	**0.258**	-0.008	-0.135	-0.298	**0.307**	Wheel Line	0.307
	Pinned8	-0.024	-0.329	-0.165	**0.353**	-0.019	-0.204	-0.301	**0.320**	Tandem Line	0.353
S33	Fixed5	-0.001	0.048	-0.252	**0.253**	-0.001	0.048	-0.252	**0.253**	Wheel Line	0.253
	Fixed8	-0.003	0.030	-0.375	**0.378**	-0.003	0.030	-0.375	**0.378**	Wheel Line	0.378
	Pinned5	-0.001	0.038	-0.237	**0.237**	-0.001	0.038	-0.237	**0.237**	Wheel Line	0.237
	Pinned8	-0.001	0.034	-0.316	**0.318**	-0.001	0.034	-0.316	**0.318**	Wheel Line	0.318
										MAX	0.433

LIVE LOAD - BOTTOM STRESSES @ JOINT CL [ksi]											
		Through Tandem Line				Through Wheel Line				ABS WORST CASE	
		Lane Load	Tandem Load	Wheel Load	Abs Magnitude	Lane Load	Tandem Load	Wheel Load	Abs Magnitude	Location	Abs Magnitude
S11	Fixed5	0.004	0.173	0.038	**0.178**	0.004	0.063	0.220	**0.225**	Wheel Line	0.225
	Fixed8	0.014	0.305	0.129	**0.319**	0.014	0.203	0.364	**0.379**	Wheel Line	0.379
	Pinned5	0.009	0.215	0.093	**0.224**	0.009	0.140	0.241	**0.249**	Wheel Line	0.249
	Pinned8	0.024	0.301	0.151	**0.325**	0.024	0.236	0.326	**0.349**	Wheel Line	0.349
S33	Fixed5	0.001	-0.055	0.232	**0.233**	0.001	-0.055	0.232	**0.233**	Wheel Line	0.233
	Fixed8	0.002	-0.036	0.365	**0.367**	0.002	-0.036	0.365	**0.367**	Wheel Line	0.367
	Pinned5	0.001	-0.049	0.214	**0.215**	0.001	-0.049	0.214	**0.215**	Wheel Line	0.215
	Pinned8	0.001	-0.044	0.307	**0.308**	0.001	-0.044	0.307	**0.308**	Wheel Line	0.308
										MAX	0.379

G.2 Simulated Deck Bending Demands

The following calculations determine the maximum shear and bending moment in the UHPC joint region of each simulated deck specimen.

Load Case 1: Self-Weight

The HSS end supports were only effective at resisting upward slab deflection, so the self-weight was largely resisted by loading plate under the UHPC joint. Since some panels were longer than others (from flipping around old panels with the UHPC joint still attached, for instance), this induced rotation about the loading plate which was then resisted by one of the HSS supports.

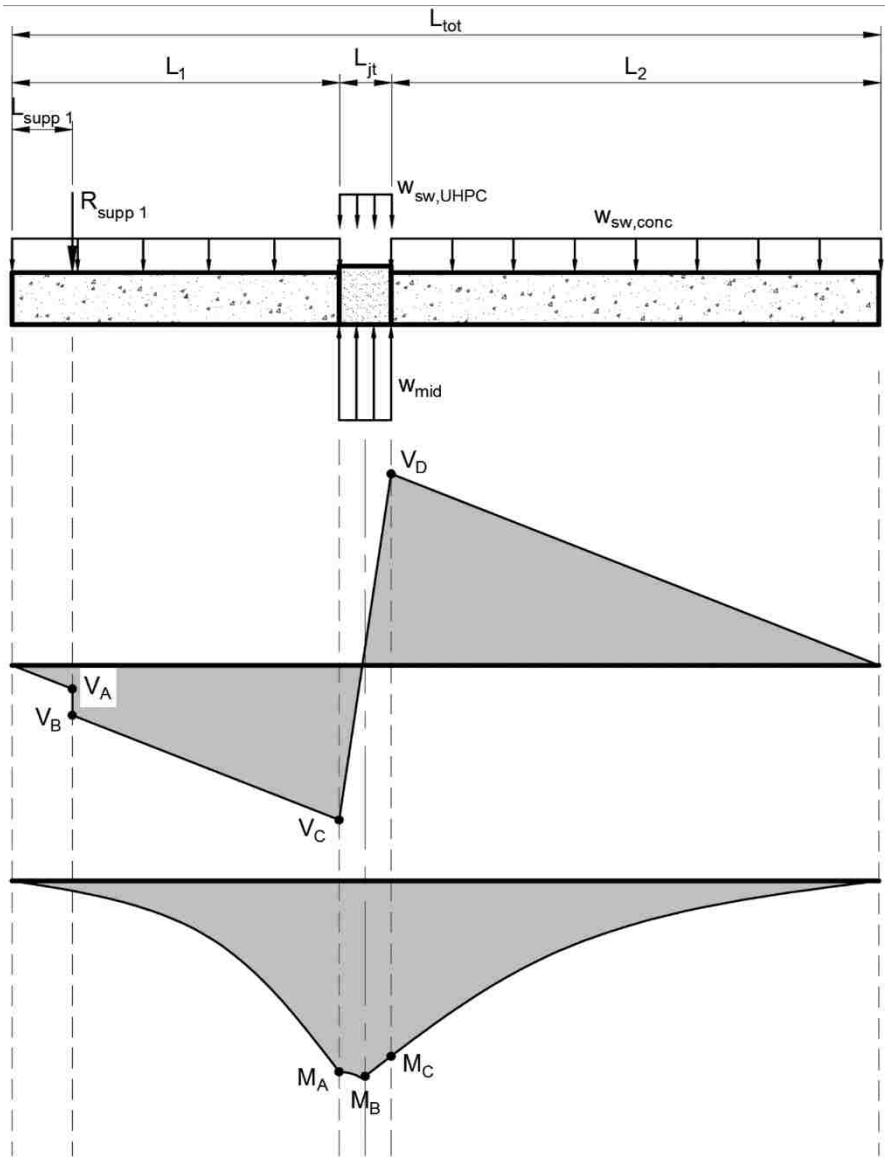

Appendix Figure G.1. Shear and bending moment diagram for Load Case 1.

Support Force

Self-weight of the simulated deck assembly acted downward and was supported by only those elements which resisted downward deflections (i.e.: the loading plate). Due to the unequal spans on both sides of the joint, the slab tended to rotate about the loading plate and was prevented from rotating by one of the HSS supports.

$$\sum M_{CL} = 0 = R_{supp}\left(L_1 + \frac{L_{jt}}{2} - L_{supp}\right) + w_{sw,conc}L_1\left(\frac{L_1 + L_{jt}}{2}\right) - w_{sw,conc}L_2\left(\frac{L_2 + L_{jt}}{2}\right)$$

$$\boxed{R_{supp} = \frac{w_{sw,conc}\left[L_2\left(L_2 + L_{jt}\right) - L_1\left(L_1 + L_{jt}\right)\right]}{2\left(L_1 + \frac{L_{jt}}{2} - L_{supp}\right)}}$$

$$\sum F_z = 0 = -R_{supp} - w_{(sw,conc)(L_{tot} - L_{jt})} - w_{sw,UHPC}L_{jt} + w_{mid}L_{jt}$$

$$\boxed{w_{mid} = \frac{1}{L_{jt}}\left[R_{supp} + w_{sw,conc}\left(L_{tot} - L_{jt}\right) + w_{sw,UHPC}L_{jt}\right]}$$

Shear Force

$$\boxed{\begin{gathered} V_A = -w_{sw,conc}L_{supp} \\ V_B = V_A - R_{supp} \\ V_{mid} = V_C + \frac{L_{jt}}{2}\left(w_{mid} - w_{sw,UHPC}\right) \\ V_C = V_B - w_{sw,conc}\left(L_1 - L_{supp}\right) \\ V_D = w_{sw,conc}L_2 \end{gathered}}$$

Location of Zero Shear

Measured from the interface of the UHPC joint nearest Panel #1.

$$\boxed{x_0 = \frac{V_C}{V_C - V_D}L_{jt}}$$

Bending Moment

$$\boxed{\begin{gathered} M_A = \frac{1}{2}\left[V_A L_{supp} + \left(L_1 - L_{supp}\right)\left(V_B + V_C\right)\right] \\ M_B = \begin{cases} M_A + \frac{L_{jt}}{4}\left(V_C + V_{mid}\right) & ; \quad x_0 \geq \frac{L_{jt}}{2} \\ M_A + \frac{1}{2}\left[V_C x_0 + V_{mid}\left(\frac{L_{jt}}{2} - x_0\right)\right] & ; \quad x_0 < L_{jt} \end{cases} \\ M_C = -\frac{V_D L_2}{2} \end{gathered}}$$

Load Case 2: Support Tightening

The HSS end supports were tightened against the top of the simulated deck to prevent excessive support slip. Before testing began, the slab rested on two jack stands near the ends of the slab which were offset from the HSS support centerline.

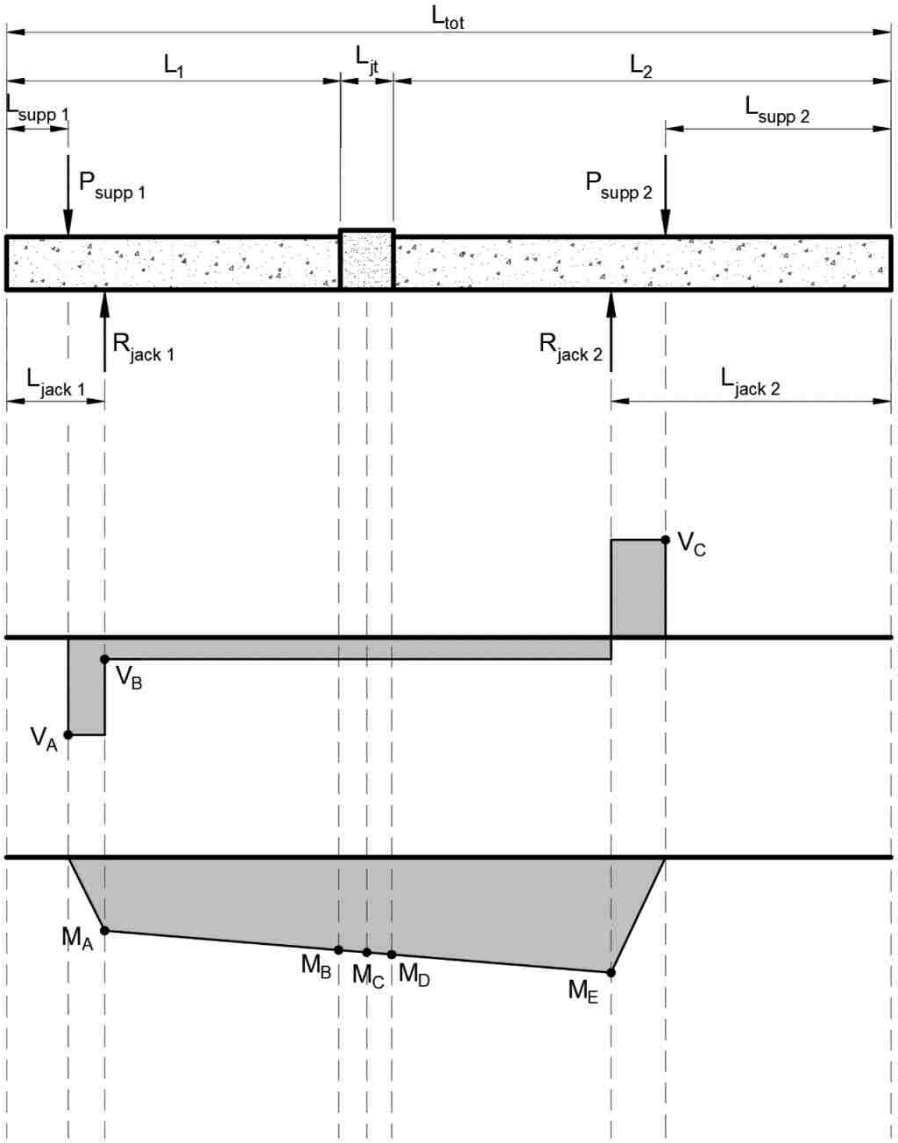

Appendix Figure G.2 Shear and bending moment diagram for Load Case 2.

Support Force

Both HSS supports were tightened against the slab by approximately 3 kips, which was derived

from tightening each end of each HSS support using approximately 30 lbs of force with an 18-inch lever arm to achieve one-half turn past the snug-tightened state. The jack stands at each end of the panel fully supported these forces.

$$\sum M_{jack\,1} = 0 = P_{supp\,1}\left(L_{jack\,1} - L_{supp\,1}\right) + R_{jack\,2}\left(L_{tot} - L_{jack\,1} - L_{jack\,2}\right) - P_{supp\,2}\left(L_{tot} - L_{jack\,1} - L_{supp\,2}\right)$$

$$\boxed{R_{jack\,2} = \frac{P_{supp\,2}\left(L_{tot} - L_{jack\,1} - L_{supp\,2}\right) - P_{supp\,1}\left(L_{jack\,1} - L_{supp\,1}\right)}{L_{tot} - L_{jack\,1} - L_{jack\,2}}}$$

$$\sum F_z = 0 = -P_{supp\,1} - P_{supp\,2} + R_{jack\,1} + R_{jack\,2}$$

$$\boxed{R_{jack\,1} = P_{supp\,1} + P_{supp\,2} - R_{jack\,2}}$$

Shear Force

$$\boxed{\begin{gathered} V_A = -P_{supp\,1} \\ V_B = V_A + R_{jack\,1} \\ V_C = P_{supp\,2} \end{gathered}}$$

Bending Moment

$$\boxed{\begin{gathered} M_A = V_A\left(L_{jack\,1} - L_{supp\,1}\right) \\ M_B = M_A + V_B\left(L_1 - L_{jack\,1}\right) \\ M_C = M_B + \frac{V_B L_{jt}}{2} \\ M_D = M_C + \frac{V_B L_{jt}}{2} \\ M_E = M_D + V_B\left(L_2 - L_{jack\,2}\right) \end{gathered}}$$

Load Case 3: Applied Load

During testing, the load was applied at midspan between the two HSS supports and was distributed over the width of the loading plate.

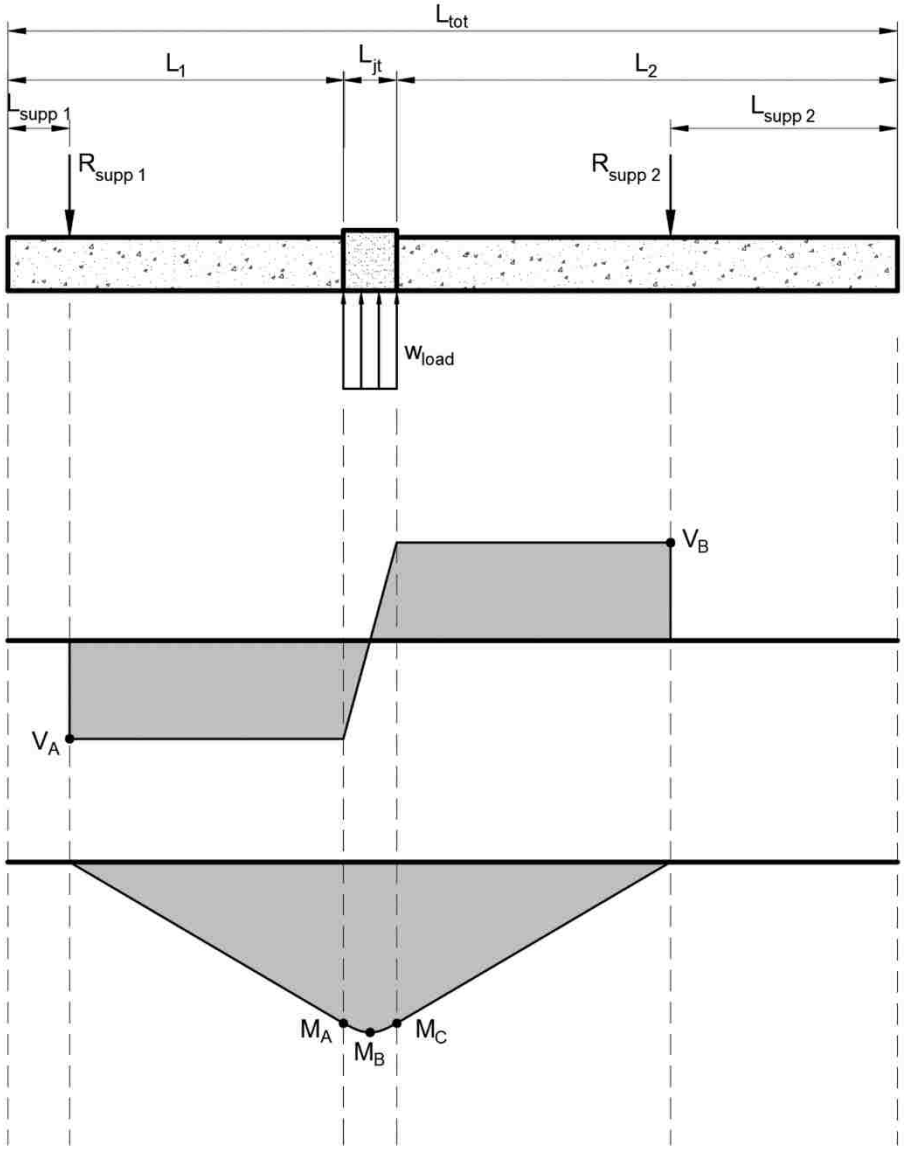

Appendix Figure G.3. Shear and bending moment diagram for Load Case 3.

Support Force

The total force recorded by the load cell, w_{tot}, consisted of lifting the total self-weight of the simulated deck, W_{sw}, in addition to the applied load, w_{load}. To separate self-weight from the applied load:

$$w_{load} = w_{tot} - w_{mid}$$

By symmetry, both HSS support forces were equal.

$$\boxed{R_{supp\,1} = R_{supp\,2} = \frac{w_{load} L_{jt}}{2}}$$

Shear Force

$$\boxed{\begin{aligned} V_A &= -R_{supp} \\ V_B &= R_{supp} \end{aligned}}$$

Bending Moment

$$\boxed{\begin{aligned} M_A &= V_A\left(L_1 - L_{supp\,1}\right) \\ M_B &= M_A + \frac{V_A L_{jt}}{4} \\ M_C &= -V_B\left(L_2 - L_{supp\,2}\right) \end{aligned}}$$

G.3 Material Strength Correction

The standard curing temperature specified by ASTM C192 was followed for curing the majority of UHPC material specimens. The material specimens which were used for the simulated deck specimens 3-8 were cured at temperatures between 45-50 °F due to mechanical issues which prevented hot water from being provided to the curing room. As a result, these material specimens were weaker and less stiff than the standard-cured specimens which were used for the remainder of test specimens.

A material strength correction derived from maturity calculations was implemented to offset the effect of curing in a colder environment. Using the S/T fit equations, the maturity of each material specimen was determined by Equation (20) at each of the standard 14 days of curing for both standard and cold-cured specimens. A base temperature, T_0, of 12.5 °F was utilized.

$$M = \int (T - T_0) dt \quad \textbf{(20)}$$

Performing these calculations resulted in a 14-day target maturity of 847.0 °F-days if the material was cured at standard temperatures and a maturity of 525.0 °F-days if cold-cured. To reach this target maturity, the materials would need to be cold-cured for 22.6 days.

This data is provided below in Appendix Table G.2.

Appendix Table G.2. S/T fit equation results (units: ksi) with calculated maturity (units: °F-days).

Day	Compression Cubes	Compression Cylinders	Split-Tension Cylinders	Flexural Beams	Direct Tension	Pullout Bond Cylinder	M_{std}	M_{cold}
0	0.000	0.000	0.000	0.000	0.000	0.000	0.0	0.0
1	5.484	5.692	0.948	0.769	0.495	3.624	60.5	37.5
2	8.496	8.261	1.416	1.153	0.661	4.902	121.0	75.0
3	10.401	9.724	1.695	1.384	0.744	5.555	181.5	112.5

4	11.714	10.668	1.880	1.538	0.794	5.951	242.0	150.0
5	12.673	11.329	2.012	1.648	0.827	6.217	302.5	187.5
6	13.406	11.816	2.110	1.730	0.851	6.408	363.0	225.0
7	13.983	12.191	2.187	1.795	0.869	6.552	423.5	262.5
8	14.449	12.488	2.248	1.846	0.883	6.664	484.0	300.0
9	14.834	12.729	2.298	1.888	0.894	6.754	544.5	337.5
10	15.157	12.929	2.340	1.923	0.903	6.828	605.0	375.0
11	15.432	13.097	2.375	1.952	0.911	6.889	665.5	412.5
12	15.669	13.240	2.405	1.978	0.917	6.941	726.0	450.0
13	15.875	13.364	2.432	2.000	0.923	6.986	786.5	487.5
14	**16.057**	**13.472**	**2.454**	**2.019**	**0.928**	**7.025**	**847.0**	**525.0**
15	16.217	13.568	2.475	2.036	0.932	7.059	907.5	562.5
16	16.360	13.652	2.493	2.051	0.936	7.089	968.0	600.0
17	16.488	13.727	2.509	2.065	0.939	7.115	1028.5	637.5
18	16.604	13.795	2.523	2.077	0.942	7.139	1089.0	675.0
19	16.709	13.856	2.536	2.088	0.944	7.161	1149.5	712.5
20	16.804	13.911	2.548	2.098	0.947	7.180	1210.0	750.0
21	16.892	13.962	2.559	2.107	0.949	7.198	1270.5	787.5
22	16.972	14.008	2.569	2.115	0.951	7.214	1331.0	825.0
22.6	**17.016**	**14.033**	**2.574**	**2.120**	**0.952**	**7.223**	**1366.5**	**847.0**

A scaling factor was applied to the 14-day strength of all cold-cured material strengths which was derived from the ratio between 22.6-day and 14-day strengths from S/T data.

$$\text{Scale Factor} = \frac{f(t = 22.6)}{f(t = 14)}$$

G.4 Yield Line Collapse Load

The Equal Strength design method requires that the non-contact spliced connection can achieve the full strength of the reinforcement before the deck collapses. This section calculates the collapse load for a bending failure mechanism.

A simple yield line analysis determines the collapse load for a bending failure mechanism in the deck. Appendix Figure G.4 depicts the yield line pattern due to a single truck wheel load.

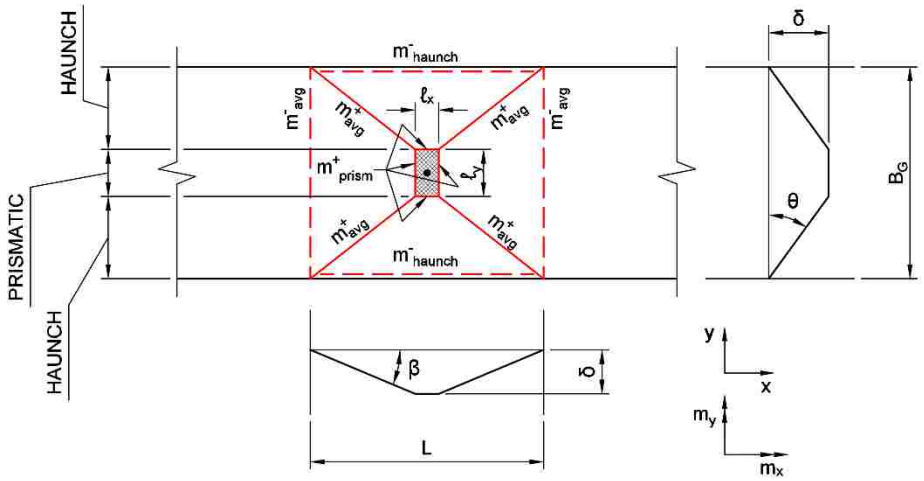

Appendix Figure G.4. Yield line pattern for a bending collapse mechanism due to a single wheel load.

Assumptions:

- Deck Reinforcement: #5 @ 6" OC
- Steel Behavior: Elastoplastic with f_y = 60 ksi
- Concrete Behavior: Rectangular stress block with f_c' = 8,000 psi and ε_{cu} = 0.003 in/in

The following calculations determine the collapse load required to yield all deck reinforcement by using the Principle of Virtual Work.

$$\beta = \frac{2\delta}{L - \ell_x}, \qquad \theta = \frac{2\delta}{B_G - \ell_y}$$

$$(VW)_{int} = 2m^{-}_{y,avg}\beta B_G + 2m^{-}_{x,haunch}\theta L + 2m^{+}_{y,prism}\beta \ell_y + 2m^{+}_{x,prism}\theta \ell_x$$

$$+ 4m^{+}_{x,avg}\theta\left(\frac{L-\ell_x}{2}\right) + 4m^{+}_{y,avg}\beta\left(\frac{B_G-\ell_y}{2}\right)$$

$$(VW)_{ext} = P\delta$$

Standard code procedures were used to calculate the bending capacity terms which are listed below in Appendix Table G.3. By equating the internal and external virtual work terms, the collapse load is approximately 545 kips for 5-foot girder spacing and 575 kips for 8-foot girder spacing.

Appendix Table G.3. Bending capacity terms used in the yield line analysis.

	x Direction	y Direction
$\boldsymbol{m^{+}_{prism}}$	18.8	18.8
$\boldsymbol{m^{-}_{prism}}$	11.8	11.8
$\boldsymbol{m^{+}_{haunch}}$	34.3	34.3
$\boldsymbol{m^{-}_{haunch}}$	27.3	27.3
$\boldsymbol{m^{+}_{avg}}$	26.6	26.6
$\boldsymbol{m^{-}_{avg}}$	19.6	19.6

G.5 Punching Shear Collapse Load

The second collapse mechanism considered is that of a punching shear failure through the deck caused by a maximum truck wheel load, as illustrated in Appendix Figure G.5. For simplicity, the deck reinforcement dowel shear strength contribution will be neglected.

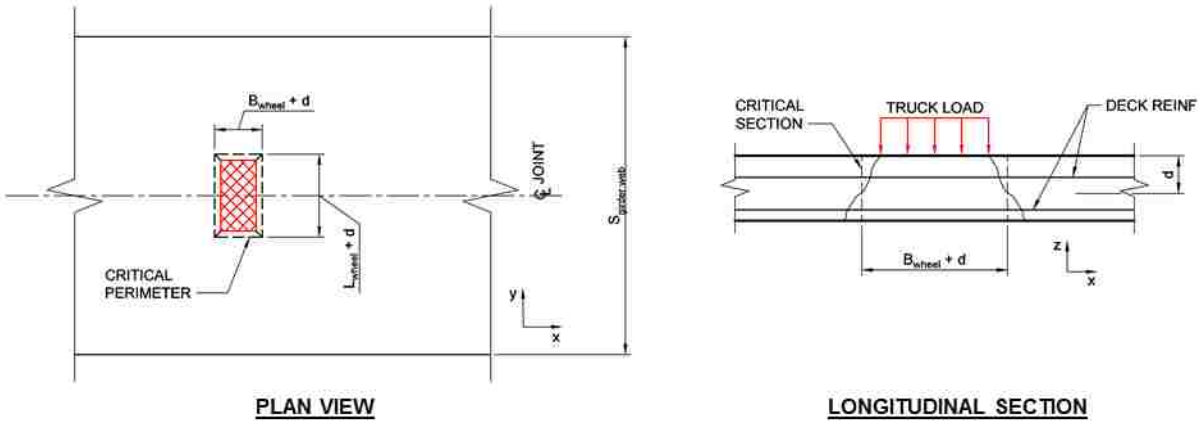

Appendix Figure G.5. Punching shear failure mechanism due to a single wheel load.

Assumptions:

- UHPC shear strength is equal to conventional concrete shear strength.
- Wheel Load Dimensions: 20" x 10"
- Concrete Strength: f_c' = 8,000 psi
- Load Type: Interior (α_s = 40)

$$b_0 = 2(B_{wheel} + d) + 2(L_{wheel} + d)$$

$$\beta = \frac{L_{wheel}}{B_{wheel}}$$

$$V_c = \min\left\{\begin{matrix} 4 \\ 2 + \frac{4}{\beta} \\ 2 + \frac{\alpha_s d}{b_0} \end{matrix}\right\} \sqrt{f_c'} b_0 d$$

Solving this equation results in approximately 90 kips of punching shear capacity which is substantially lesser than the bending failure mechanism. Thus, in the case of overloading, the bridge deck will fail through punching shear which suggests that the UHPC joint design based on expected bending capacity is irrelevant if a shear failure mechanism occurs first.

G.6 Interface Shear Demand

Although not explicitly investigated by this project, the shear demand and capacity can be approximately evaluated. The primary source of shear stress at the interface between the UHPC and conventional concrete is due to correcting the DBT girder's differential camber to align the driving surface with adjacent girders. Strongbacks are used with hydraulic rams to apply forces across the width of the DBT. The cambered shape of the girder will be simplified as a sine curve which requires a corresponding sine curve load distribution. Invoking the governing equation for bending produces the force required to correct a given difference in camber Δ_0.

$$EIv^{iv}(x) = w_0 \sin\left(\frac{\pi x}{L}\right)$$

Integrating this relationship four times and applying appropriate boundary conditions results in the following relationship:

$$v(x) = \frac{w_0 L^4}{\pi^4 EI} \sin\left(\frac{\pi x}{L}\right)$$

To correct a differential camber of Δ_0 at the girder's midspan:

$$w_{0,\Delta_0} = \frac{\Delta_0 \pi^4 EI}{L^4}$$

The section properties for a 65-inch deep DBT girder spaced at 8 feet and spanning the maximum allowable 140 feet are used here as representative values (Concrete Technology Corporation 1995). A concrete modulus of elasticity of 5,000 ksi is again assumed.

$$w_{0,\Delta_0,DBT65} = \frac{\Delta_0 \pi^4 (5{,}000)(610{,}435)}{(140\times12)^4} = 0.0373\Delta_0 \; k/in$$

For interior longitudinal joints, this force is divided equally between two joints.

$$w_{0,\Delta_0,DBT65,each} = \frac{w_{0,\Delta_0,DBT65,each}}{2} = 0.0187\Delta_0\ k/in$$

This magnitude creates interfacial shear stresses through the deck's thickness. For a six-inch thick deck:

$$v = \frac{w_{0,\Delta_0,DBT65,each}}{h} = \frac{w_{0,\Delta_0,DBT65,each}}{(6")} \rightarrow \boxed{v = 3.11\Delta_0\ psi}$$

The AASHTO LRFD Specification Section 5.8.4.3 assumes the cohesion component between concrete cast against concrete with a surface roughened to a 1/4-inch magnitude is 280 psi (American Association of State Highway and Transportation Officials 2012)

Appendix H
EXPERIMENTAL EQUIPMENT

This section defines each instrument used for material creation and data acquisition.

UHPC Pan Mixer

A pan mixer was used instead of a traditional drum mixer due to the lack of coarse aggregate to adequately mix the concrete. A low-shear type of pan mixer was utilized based on affordability and availability to contractors. The basic specifications for this mixer (displayed in Appendix Figure H.1) are detailed below in Appendix Table H.1.

Appendix Table H.1. Pan mixer specifications.

Rated Batch Output	60 L (2.1 ft^3)
Voltage	230 V
Motor Rating	2.2 HP
Motor Power	1600 W
Number of Paddles	3
Paddle Rotational Speed	32 rpm

Appendix Figure H.1. Pan mixer used to mix UHPC.

300-kip Baldwin®

A 300-kip capacity Baldwin® testing machine (see Appendix Figure H.2) provided the load for material strength tests (excepting the pullout bond cylinders) and calibrating load cells.

Appendix Figure H.2 300-kip Baldwin testing machine.

Load Cell

The maximum force expected from these tests arises from the epoxy-coated #5 rebar fracturing during the bond curb tests. Preliminary tests on this rebar resulted in a uniaxial fracture force of approximately 32 kips which will be achieved during the curb and pullout cylinder tests, and a fracture force of approximately 25-30 kips in a flexural application. The load cell used for all experiments had a sufficient 50-kip capacity.

Hydraulic Ram and Pump

Two different hydraulic rams were used depending on the type of experiment. The bond curb tests used a 100-ton capacity hydraulic ram with a 4-inch stroke that sufficiently provided the expected failure forces and accommodated the expected deformations. The simulated deck tests used an Enerpac® 10-ton capacity hydraulic ram (see Appendix Figure H.3) with a 2-inch stroke, which was preferred because it could be fitted with a hand pump to precisely control the load increment.

A hydraulic pump connected to the hydraulic ram remotely controlled the ram's stroke via a mechanical pump or a hand pump.

Appendix Figure H.3. Enerpac® hydraulic ram with handpump.

Prestressing Strand Chuck

A 0.6-inch diameter prestressing strand chuck fitted over the #5 rebar to uniaxially stress the rebar during bond curb tests and pullout bond cylinders.

Linear Potentiometer

Three different potentiometers measured deformations depending on their magnitude. BEI Sensors® linear potentiometers (see Appendix Figure H.4) with a 1.5-inch stroke measured the smallest expected deflections, whereas potentiometers with a 3.5-inch stroke measured more moderate deflections.

Appendix Figure H.4. BEI Sensors® linear potentiometers.

High-definition UniMeasure® string potentiometers (see Appendix Figure H.5) with a range of 9-12 inches measured midspan deflections for the simulated deck tests.

Appendix Figure H.5. UniMeasure® string potentiometer.

Optotrak Camera

Two Optotrak Certus® cameras (see Appendix Figure H.6) measured 3D deformations within the joint region of the simulated deck tests.

Appendix Figure H.6. Optotrak Certus® camera.

Appendix I
SAND SIEVE ANALYSIS

A particular type of sand was not specified for mixing the UHPC, but Qiao provided general sieve analysis results for their custom-sieved sand. Each batch of UHPC used bagged UNIMIN 4075 sand based largely on local availability which was not custom-sieved.

Appendix Table I.1. Sieve analysis results for UNIMIN 4075 sand.

	% Passing (Qiao)	% Passing UNIMIN 4075 (UNIMIN)	% Passing UNIMIN 4075 (UW)
#12	N/A	N/A	N/A
#16	N/A	99.8	N/A
#20	N/A	91	99.7
#30	100	60.2	N/A
#40	N/A	9.8	37.1
#50	29	1.0	N/A
#70	N/A	0.3	6.0
#100	6.3	0.1	0
#140	N/A	0	0
#200	0	0	0
Pan	0	0	0

As seen in Appendix Table I.1, Qiao's requirement was relatively vague since they did not use a large variety of sieve sizes. In general, the UNIMIN 4075 sand is coarser than that specified by Qiao.

Appendix J
SIMULATED DECK EXPERIMENT LOGS

Specimen #1

No formal log was kept for this specimen.

Specimen #2

Date	Joint Width [in]	Clear Cover [in]	Lateral Offset [in]
December 30, 2016	3	1	0

Note: Transverse deflections in parentheses are after the side ram was pumped up.

Load Stage	Load [kips]	Vertical Deflection [in]		Transverse Deflection [in]		Comments
		East	West	Top	Bottom	
1	1.15	0.005	0.005	0	N/A	N/A
2	1.9	0.012	0.012	0.00015	N/A	N/A
3	2.65	0.025	0.025	0	N/A	N/A
4	3.35	0.0018	0.041	0.0008	N/A	N/A
5	4.3	0.0082	0.07	0.001	N/A	Interface (IF) crack forms.
6	5.1	0.015	0.1	0.0015	N/A	IF cracks spreading.
7	5.6	0.028	0.124	0.0023	N/A	IF crack size 0.008".
8	6.4	0.064	0.17	0.0028	N/A	Panel crack 5" from IF.
9	7.1	0.092	0.205	0.004	N/A	
10	7.7	0.127	0.243	0.006	N/A	South panel cracks seen at 11" from southern IF.
11	8.3	0.183	0.303	0.013	0.037	IF crack size 0.018". Side ram pumped up.
12	8.8	0.231	0.345	0.002	N/A	Longitudinal cracks in UHPC form.
13	9.25	0.288	0.414	0.007	0.0006	IF crack size 0.025".
14	9.4	0.333	0.462	0.012	0.003	IF crack size 0.036". Longitudinal crack size 0.016".
15	9.5	0.415	0.56	0.005	0.0014	Side ram pumped to approx. 1,500 psi.
16	8.8	0.544	0.588	0.004	0.0078	IF crack size 0.06".
17	7.3	0.726	0.88	0.0075	0.017	
18	5.9	0.924	1.072	0.008	0.022	
19	5	1.112	1.263	0.009	0.023	
20	3.75	1.466	1.632	0.013	0.023	IF crack size 0.25".
21	2.6	2.123	2.287	0.015	0.022	

Specimen #3

Date	Joint Width [in]	Clear Cover [in]	Lateral Offset [in]
January 17, 2017	5	1	0

Load Stage	Load [kips]	Vertical Deflection [in]		Transverse Deflection [in]		Comments
		East	West	Top	Bottom	
1	2	0.0103	0.0087	0.0011	0.002	
2	4	0.028	0.025	0.0016	0.0043	
3	6.05	0.094	0.087	0.0022	0.0052	North interface (IF) crack begins.
4	7.9	0.169	0.174	0.003	0.0057	Panel crack @ 8" from joint CL forms.
5	10	0.267	0.278	0.0047	0.0064	IF crack size 0.013".
6	12	0.362	0.379	0.009	0.008	IF crack size 0.016". Panel crack size 0.013".
7	14	0.483	0.499	0.018	0.012	IF crack size 0.016". Panel crack size 0.013". Longitudinal cracks in UHPC form.
8	15.9	0.605	0.611	0.007	0.029	Panel crack @ 15" from joint CL forms.
9	16	0.741	0.76	0.019	0.034	IF crack size 0.05".
10	13.5	1.058	1.113	0.052	0.04	IF crack size 0.1".
11	9	1.425	1.484	0.053	0.038	IF crack size 0.3125".
12	6.2	1.979	2.057	0.055	0.003	IF crack size 0.5".

Specimen #4

Date	Joint Width [in]	Clear Cover [in]	Lateral Offset [in]
January 18, 2017	5	1	2

Load Stage	Load [kips]	Vertical Deflection [in]		Transverse Deflection [in]		Comments
		East	West	Top	Bottom	
1	2.3	0.009	0.017	0.0001	0.0003	
2	3.8	0.045	0.051	0.0005	0.0001	
3	6	0.125	0.13	0.0019	0.0012	Panel cracks @ 8" & 16" from joint CL form.
4	8	0.226	0.222	0.005	0.0017	UHPC interface (IF) cracks form. Panel crack size 0.002".
5	9.9	0.326	0.326	0.01	0.003	Panel cracks @ 4" from joint CL form. Panel crack size 0.01" @ 15" from joint CL.
6	11.5	0.432	0.424	0.0003	0.011	IF cracks spread across width of joint.
7	13.3	0.594	0.589	-0.013	0.0223	IF crack size 0.008".
8	11	0.855	0.834	-0.046	0.0338	
9	7	1.282	1.264	-0.049	0.034	IF crack size 0.375". (?)
10	4.6	1.617	1.639	-0.047	0.029	
11	3.6	2.005	2.05	-0.046	0.026	IF crack size 0.018". Side ram pumped up after this reading.

Specimen #5

Date	Joint Width [in]	Clear Cover [in]	Lateral Offset [in]
February 1, 2017	6	1	0

Note: Transverse deflections in parentheses are after the side ram was pumped up.

Load Stage	Load [kips]	Vertical Deflection [in]		Transverse Deflection [in]		Comments
		East	West	Top	Bottom	
1	2.05	0.015	0.004	-0.0004	0.0008	N/A
2	4.05	0.035	0.011	-0.001	0.0018	N/A
3	6	0.083	0.043	-0.0016	0.0029	Panel crack @ Grid 5.5
4	8	0.169	0.117	-0.0024	0.0032	Interface (IF) crack begins. Panel crack @ Grid 8, size 0.005".
5	9.9	0.246	0.2	-0.0041	0.0035	" "
6	12.1	0.335	0.295	-0.0125 (0.0001)	0.0046 (0.0264)	New panel crack @ Grid 4.7 & 9. IF crack size 0.01". Side ram was accidentally released and the side plates dropped. They were blocked back up with the original wood pieces to attempt to bring the deflections back to where they were before the ram dropped.
7	13.9	0.425	0.375	-0.0032	0.027	New panel crack just beyond Grid 9. Longitudinal crack in UHPC between Grid B & C. IF crack size 0.016". Panel crack size 0.013".
8	15.8	0.57	0.51	-0.023 (-0.0006)	0.027 (0.0488)	New panel crack @ Grid 6.7 and beyond Grid 9. Longitudinal crack in UHPC between Grid B & C beginning to form cone-shaped cracks. New longitudinal crack in UHPC between Grid D & E. IF crack size 0.04". Panel crack size 0.016". Side ram pumped up.
9	15	0.775	0.707	-0.0143 (-0.0011)	0.049 (0.060)	Longitudinal crack in UHPC @ Grid F. IF crack size 0.125". Panel crack size 0.016". Side ram pumped up.
10	13.2	0.987	0.929	-0.0023	0.059	IF crack size 0.1875". Longitudinal crack size 0.01". Panel crack size 0.013".
11	11.1	1.262	1.216	-0.013 (-0.0004)	0.051 (0.06)	IF crack size 0.25". Longitudinal crack size 0.01". Panel crack size 0.01". Side ram pumped up.
12	8.9	1.51	1.51	-0.00007	0.0593	IF crack size 0.3125". Longitudinal crack size 0.016". Panel crack size 0.01".
13	8.1	1.756	1.78	-0.0039 (-0.0006)	0.052 (0.056)	IF crack size 0.375". Longitudinal crack size 0.02". Panel crack size 0.01". Side ram pumped up.
14	7.7	1.996	2.01	-0.001	0.055	IF crack size 0.4375". Longitudinal crack size 0.016". Panel crack size 0.01".
15	7.2	2.245	2.259	-0.0047	0.051	IF crack size 0.5625". Longitudinal crack size 0.02". Panel crack size 0.01".

Specimen #6

Date	Joint Width [in]	Clear Cover [in]	Lateral Offset [in]
February 2, 2017	5	1	1

Note: Transverse deflections in parentheses are after the side ram was pumped up.

Load Stage	Load [kips]	Vertical Deflection [in]		Transverse Deflection [in]		Comments
		East	West	Top	Bottom	
1	2	0.0073	0.0065	-0.00004	-0.00004	N/A
2	4.2	0.0368	0.0255	0.0008	-0.0003	N/A
3	6	0.0763	0.0472	0.0013	-0.0013	Interface (IF) crack forms. Panel crack forms @ Grid 5.25.
4	8.1	0.1467	0.1136	0.0011	-0.0017	Panel crack forms @ Grid 6.5-7.
5	10	0.2186	0.1823	-0.0003	-0.0018	IF crack size 0.01". Panel crack size 0.005". Panel crack forms @ Grid 8.5.
6	12	0.288	0.255	-0.0025	-0.0015	IF crack size 0.016".
7	14.1	0.377	0.346	-0.0054	-0.0002	IF crack size 0.02".
8	16	0.467	0.437	-0.0104 (0.0013)	0.0016 (0.016)	IF crack size 0.03". Longitudinal crack in UHPC forms. Side ram pumped up.
9	18	0.602	0.577	-0.0053 -0.0103 (0.0013)	0.021 0.0188 (0.032)	IF crack size 0.03". Longitudinal crack in UHPC between Grids B & C and at Grid D forms. Panel crack size 0.013". Side ram pumped up.
10	19.8	0.805	0.767	-0.0134 -0.023 (-0.0011)	0.039 0.035 (0.0708)	Extensive UHPC cracking. IF crack size 0.07". Longitudinal crack size 0.025". Panel crack size 0.013". Side ram pumped up.
11	19.2	1.022	0.973	-0.010 -0.021 (0.0011)	0.077 0.0696 (0.096)	Cone-shaped panel crack forms between Grid E & F. IF crack size 0.125". Longitudinal crack size 0.025". Panel crack size 0.02". Side ram pumped up.
12	15.7	1.272	1.234	0.00025 -0.0099 (0.0026)	0.0966 0.087 (0.0998)	Further propagation of UHPC cracks. IF crack size 0.25". Longitudinal crack size 0.02". Panel crack size 0.013". Side ram pumped up.
13	13.6	1.534	1.495	0.0025	0.0995	IF crack size 0.3275". Longitudinal crack size 0.02". Panel crack size 0.013".
14	11.6	1.8	1.744	-0.010 -0.024 (-0.00001)	0.088 0.069 (0.097)	IF crack size 0.375". Longitudinal crack size 0.02". Panel crack size 0.013". Side ram pumped up.
15	9.6	2.1	2.024	-0.0007	0.097	IF crack size 0.5". Longitudinal crack size 0.025". Panel crack size 0.013".

Specimen #7

No formal log was kept for this specimen.

Specimen #8

Date	Joint Width [in]	Clear Cover [in]	Lateral Offset [in]
January 28, 2017	6	1.75	0

Note: Transverse deflections in parentheses are after the side ram was pumped up.

Load Stage	Load [kips]	Vertical Deflection [in]		Transverse Deflection [in]		Comments
		East	West	Top	Bottom	
1	2	0.005	0.0034	-0.0003	-0.0001	N/A
2	4.2	0.0139	0.0158	-0.0005	-0.0005	N/A
3	6.2	0.033	0.022	0.0093	0.0011	N/A
4	8.2	0.064	0.056	0.009	0.001	Interface (IF) crack begins to form.
5	9.5	0.111	0.104	0.0089	0.0009	Panel crack forms 14" from center of joint. Pumped up side ram but should not have. Read incorrect sign.
6	12.1	0.159	0.163	0.024	0.01	Panel crack forms 8" from center of joint. IF crack size 0.012".
7	14	0.206	0.21	0.022	0.009	Panel crack size 0.013".
8	15.8	0.249	0.253	0.019	0.008	Panel crack forms 18" from center of joint.
9	18.1	0.308	0.311	0.017	0.0075	IF crack size 0.02".
10	20	0.364	0.371	0.012	0.007	IF crack size 0.022". Panel crack size 0.02".
11	22	0.449	0.451	0.006	0.0075	Longitudinal crack forms in UHPC, size 0.01". IF crack size 0.025".
12	23.8	0.543	0.543	0.0049	0.011	Second longitudinal crack forms in UHPC. IF crack size 0.025". Panel crack size 0.022".
13	25.1	0.76	0.758	-0.038	0.021	Third longitudinal crack forms. IF crack size 0.032". Longitudinal crack size 0.023".
14	25.6	1.016	0.994	-0.0043 (-0.0001)	0.053 (0.055)	IF crack size 0.065". Longitudinal crack size 0.04". Side ram pumped up.
15	18.7	1.428	1.408	-0.0004	0.06	IF crack size 0.125". Longitudinal crack size 0.042".
16	12.6	1.806	1.791	-0.0018	0.052	IF crack size 0.5". Longitudinal crack size 0.03". Panel crack size 0.04".
17	10	2.195	2.164	-0.004	0.046	IF crack size 0.675". Longitudinal crack size 0.03". Panel crack size 0.04".

Appendix K
EXPERIMENTAL PHOTOGRAPHS

K.1 Material Strength Tests

Compression Cube

Compression Cylinder

Split-Tension Cylinder

Flexural Beam

Direct Tension

Pullout Bond Cylinder

Elastic Modulus Cylinder

K.2 Pullout Bond Curb Tests

1" Cover

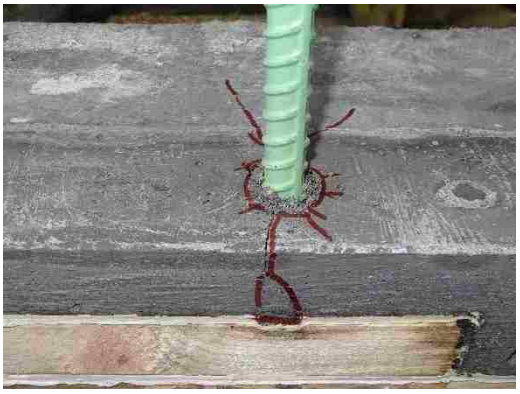

1.5” Embedment

3” Embedment

4.5” Embedment

6” Embedment

7.5” Embedment

9” Embedment

1.75” Cover

3” Embedment

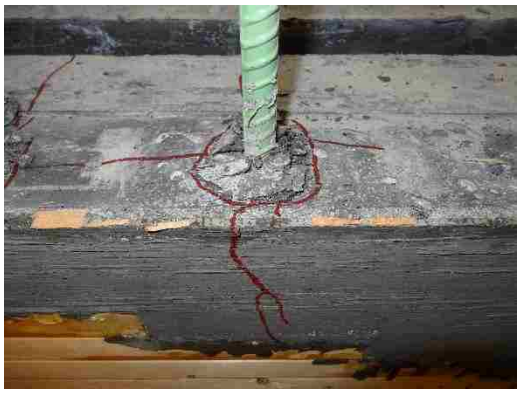

4.5” Embedment

6” Embedment

7.5” Embedment

9” Embedment

10.5” Embedment

2.5” Cover

3” Embedment

4.5” Embedment

6” Embedment

7.5” Embedment

9” Embedment

10.5” Embedment

K.3 Splice-Connection Curb Tests

1” Cover

3” Splice

3.75” Splice

4.5” Splice

5.25” Splice

6” Splice

1.75” Cover

1.25” Splice

2” Splice

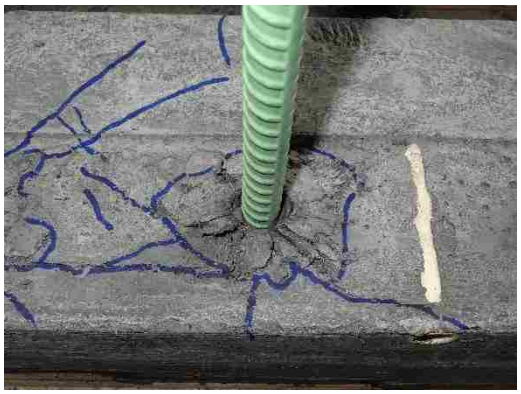

2.75” Splice

3.5” Splice

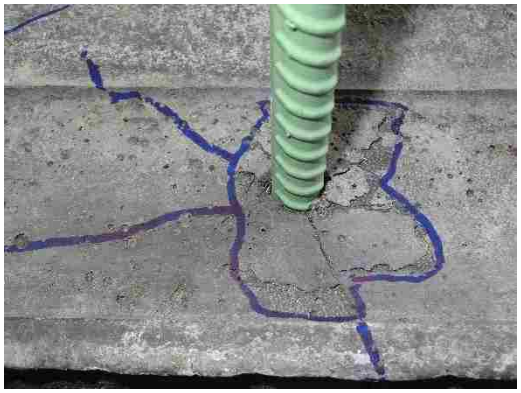

4.25” Splice

5” Splice

2.5” Cover

0.25” Splice

1” Splice

1.75” Splice

2.5” Splice

3.25” Splice

4” Splice

K.4 Flexural Simulated Deck Tests

See Appendix J for load stage parameters.

Specimen #3

Load Stage 1

Load Stage 2

Load Stage 3

Load Stage 4

Load Stage 5

Load Stage 6

Load Stage 7

Load Stage 8

Load Stage 9

Load Stage 10

Load Stage 11

Load Stage 12

Specimen #4

Load Stage 1

Load Stage 2

Load Stage 3

Load Stage 4

Load Stage 5

Load Stage 6

Load Stage 7

Load Stage 8

Load Stage 9

Load Stage 10

Load Stage 11

Specimen #5

Load Stage 1

Load Stage 2

Load Stage 3

Load Stage 4

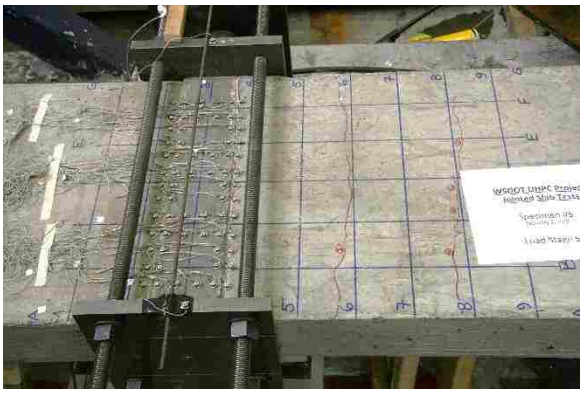

Load Stage 5

Load Stage 6

Load Stage 7

Load Stage 9

Load Stage 10

Load Stage 11

Load Stage 12

Load Stage 14

Load Stage 15

Specimen #6

Load Stage 1

Load Stage 2

Load Stage 3

Load Stage 4

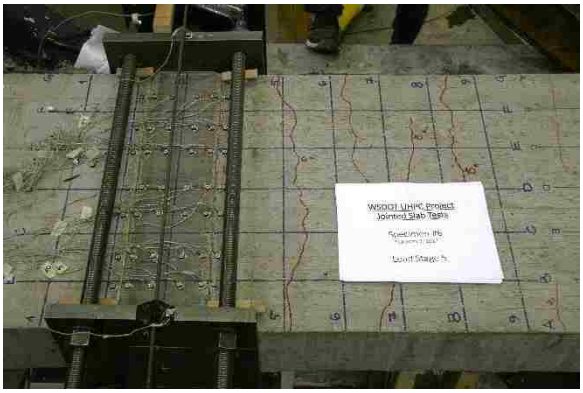

Load Stage 5

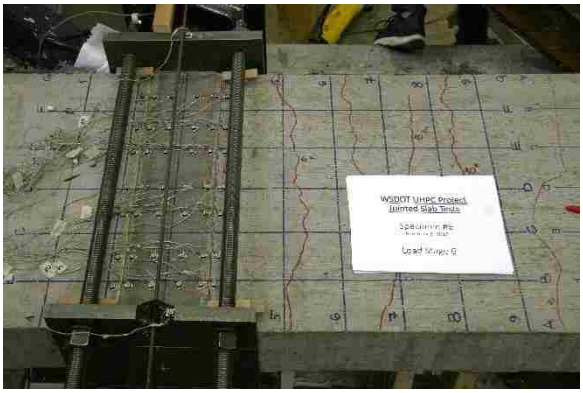

Load Stage 6

Load Stage 7

Load Stage 8

Load Stage 10

Load Stage 11

Load Stage 13

Load Stage 14

Load Stage 15

<u>Specimen #7</u>

Load Stage 1

Load Stage 2

Load Stage 3

Load Stage 4

Load Stage 5

Load Stage 6

Load Stage 7

Load Stage 8

Load Stage 9

Load Stage 10

Load Stage 11

Load Stage 12

Load Stage 13

Load Stage 14

Specimen #8

Load Stage 1

Load Stage 2

Load Stage 3

Load Stage 4

Load Stage 5

Load Stage 6

Load Stage 7

Load Stage 8

Load Stage 9

Load Stage 10

Load Stage 12

Load Stage 13

Load Stage 14

Load Stage 15

Load Stage 16

Load Stage 17